

**Lukas Schöller**

**MULTISCALE MODELING OF CURING  
AND CRACK PROPAGATION IN  
FIBER-REINFORCED THERMOSETS**

SCHRIFTENREIHE DES INSTITUTS  
FÜR ANGEWANDTE MATERIALIEN

BAND 117



Scientific  
Publishing



Lukas Schöller

**Multiscale Modeling of Curing and Crack Propagation  
in Fiber-Reinforced Thermosets**

**Schriftenreihe  
des Instituts für Angewandte Materialien  
*Band 117***

Karlsruher Institut für Technologie (KIT)  
Institut für Angewandte Materialien (IAM)

Eine Übersicht aller bisher in dieser Schriftenreihe erschienenen Bände  
finden Sie am Ende des Buches.

# Multiscale Modeling of Curing and Crack Propagation in Fiber-Reinforced Thermosets

by  
Lukas Schöller

Karlsruher Institut für Technologie  
Institut für Angewandte Materialien

Multiscale Modeling of Curing and Crack Propagation  
in Fiber-Reinforced Thermosets

Zur Erlangung des akademischen Grades eines Doktor-Ingenieurs  
von der KIT-Fakultät für Maschinenbau des Karlsruher Instituts für  
Technologie (KIT) genehmigte Dissertation

von Lukas Schöller, M.Sc.

Tag der mündlichen Prüfung: 30. November 2023

Referent: Prof. Dr. rer. nat. Britta Nestler

Korreferent: Prof. Dr. Colin Denniston

#### Impressum



Karlsruher Institut für Technologie (KIT)  
KIT Scientific Publishing  
Straße am Forum 2  
D-76131 Karlsruhe

KIT Scientific Publishing is a registered trademark  
of Karlsruhe Institute of Technology.

Reprint using the book cover is not allowed.

[www.ksp.kit.edu](http://www.ksp.kit.edu)



*This document – excluding parts marked otherwise, the cover, pictures and graphs –  
is licensed under a Creative Commons Attribution-Share Alike 4.0 International License  
(CC BY-SA 4.0): <https://creativecommons.org/licenses/by-sa/4.0/deed.en>*



*The cover page is licensed under a Creative Commons  
Attribution-No Derivatives 4.0 International License (CC BY-ND 4.0):  
<https://creativecommons.org/licenses/by-nd/4.0/deed.en>*

Print on Demand 2024 – Gedruckt auf FSC-zertifiziertem Papier

ISSN 2192-9963

ISBN 978-3-7315-1340-7

DOI 10.5445/KSP/1000167720





# Kurzfassung

Aufgrund ihres Leichtbaupotenzials bei relativ geringen Kosten gewinnen glasfaserverstärkte Polymere in industriellen Anwendungen zunehmend an Bedeutung. Sie verbinden die hohe Festigkeit von Glasfasern mit der Beständigkeit von z.B. duroplastischen Harzen. Bei der Verarbeitung von faserverstärkten Duroplasten kommt es zu einer chemischen Reaktion des Harzes. Die chemische Reaktion geht mit einer chemischen Schrumpfung einher. In Verbindung mit der thermischen Ausdehnung kann das Material bereits beim Herstellungsprozess beschädigt werden. Auch wenn das Komposit nicht vollständig versagt, kann es zu Mikrorissbildung kommen. Diese Schäden können die Blastbarkeit des Bauteils und damit seine Lebensdauer beeinträchtigen. Faserverstärkte Duroplaste enthalten Strukturen auf verschiedenen Längenskalen, die das Verhalten des Gesamtbauteils beeinflussen und daher für eine genaue Vorhersage der Rissbildung berücksichtigt werden müssen. Das Verständnis der Mechanismen der Rissbildung auf den verschiedenen Längenskalen ist daher von großem Interesse. Auf der Grundlage von Molekulardynamiksimulationen wird ein Harzsystem zusammen mit einer Faseroberfläche und einer Schlichte auf der Nanoskala betrachtet und ein systematisches Verfahren für die Entwicklung eines ausgehärteten Systems vorgestellt. Eine zweistufige Reaktion, eine Polyurethanreaktion und eine radikale Polymerisation, wird auf der Grundlage eines etablierten Ansatzes modelliert. Anhand des fertig ausgehärteten Systems werden Auswertungen über gemittelte Größen und entlang der Normalenrichtung der Faseroberfläche durchgeführt, was eine räumliche Analyse der Faser-Schlichtharz-Grenzfläche erlaubt. Auf der Mikrolängenskala werden die einzelnen Fasern räumlich aufgelöst. Mit Hilfe der Kontinuumsmechanik und der Phasenfeldmethode wird das Versagen während des Aushärtungsprozesses

auf dieser Längenskala untersucht. In der Materialwissenschaft wird die Phasenfeldmethode häufig zur Modellierung der Rissausbreitung verwendet. Sie ist in der Lage, das komplexe Bruchverhalten zu beschreiben und zeigt eine gute Übereinstimmung mit analytischen Lösungen. Dennoch sind die meisten Modelle auf homogene Systeme beschränkt, und nur wenige Ansätze für heterogene Systeme existieren. Es werden bestehende Modelle diskutiert und ein neues Modell für heterogene Systeme abgeleitet, das auf einem etablierten Phasenfeldansatz zur Rissausbreitung basiert. Das neue Modell mit mehreren Rissordnungsparametern ist in der Lage, quantitatives Risswachstum vorherzusagen, wo die etablierten Modelle eine analytische Lösung nicht reproduzieren können. Darüber hinaus wird ein verbessertes Homogenisierungsschema, das auf der mechanischen Sprungbedingung basiert, auf das neuartige Modell angewandt, was zu einer Verbesserung der Rissvorhersage selbst bei unterschiedlichen Steifigkeiten und Risswiderständen der betrachteten Materialien führt. Zudem wird zur Erzeugung digitaler Mikrostrukturen, die für Aushärtungssimulationen im Mikrobereich verwendet werden, ein Generator für gekrümmte Faserstrukturen eingeführt. Anschließend wird die Verteilung mechanischer und thermischer Größen für verschiedene Abstraktionsebenen der realen Mikrostruktur sowie für verschiedene Faservolumenanteile verglichen. Schließlich wird das neue Rissausbreitungsmodell mit dem Aushärtungsmodell kombiniert, was die Vorhersage der Mikrorissbildung während des Aushärtungsprozesses von glasfaserverstärktem UPPH-Harz ermöglicht.

# Abstract

Because of their lightweight potential at relatively low cost, glass-fiber reinforced polymers are becoming increasingly important in industrial applications. They combine the high strength of glass fibers with the durability of, for example, thermoset resins. During processing of fiber-reinforced thermosets, the resin material undergoes a chemical reaction. The chemical reaction is accompanied by chemical shrinkage. Combined with thermal expansion, the microstructure can be damaged during this manufacturing process. Even if the component does not fail completely, micro-cracking can occur. This damage can affect the overall performance of the component and therefore its lifetime. Fiber-reinforced thermosets contain microstructures on different length scales, which influence the behavior of the overall composite and must therefore be taken into account for accurate prediction of crack formation. Understanding the mechanisms of crack initiation at different length scales is therefore of great importance. To this end, using molecular dynamics simulations, a resin system is considered together with a fiber surface and a sizing layer at the nanoscale. A systematic procedure for the development of a final cured system is presented. A two-stage reaction, a polyurethane reaction and a radical polymerization, is modeled based on an established molecular dynamics approach. For the fully cured system, evaluations are carried out in terms of averaged quantities as well as quantities along the normal direction of the fiber surface, resulting in spatially varying properties along the fiber-sizing-resin interface. At the micro scale, the individual fibers are resolved. Based on continuum mechanics and the phase-field method, the fracture during the curing process is studied in this work. In materials science, the phase-field method is widely used to model crack propagation. It is capable of describing complex fracture behavior and

shows good agreement with analytical solutions. Nevertheless, most models are introduced for homogeneous systems, and few approaches are available for heterogeneous systems. Existing models are discussed and a new model for heterogeneous systems is derived based on an established phase-field approach to crack propagation. The new multi-crack order parameter model is able to predict crack growth quantitatively, whereas the established models fail to reproduce an analytical solution. Furthermore, a more advanced homogenization scheme based on the mechanical jump condition is applied to the novel model, leading to an improvement in crack prediction even for a high contrast in stiffness and crack resistance of the considered materials. A curved fiber structure generator is introduced to generate digital microstructures that are used for curing simulations at the micro scale. Subsequently, the distributions of mechanical and thermal quantities are compared for different levels of abstraction of the real microstructure, as well as for different fiber volume fractions. Finally the novel crack propagation model is combined with the curing model, which allows the prediction of micro-crack formation during the curing process of glass fiber reinforced UPPH resin.

# Acknowledgements

First of all I would like to thank my supervisor Prof. Dr. rer. nat. Britta Nestler for her trust in my abilities and for the freedom and opportunity she gave me during my time as a doctoral researcher. For the introduction, all the discussions and helpful guidance in molecular dynamics, I would also like to thank my co-supervisor Prof. Dr. Colin Denniston. Moreover, I am also grateful to both of them for providing me with the opportunity to spend a research stay at the University of Western Ontario in Canada.

Furthermore, this dissertation was made possible and carried out during my time as a research assistant at the Institute for Applied Materials – Microstructure Modeling and Simulation (IAM-MMS) at the Karlsruhe Institute of Technology (KIT) and at the Institute for Digital Materials Science (IDM) at the Karlsruhe University of Applied Sciences.

I would like to thank the German Research Foundation (DFG) for funding the investigations within the International Research Training Group 2078. The Federal Ministry of Education and Research (Bundesministerium für Bildung und Forschung) I also thank for its financial support within the framework of the “EiChFest” (project number 03SF0641A).

Special thanks fo to my team leaders Dr.-Ing. Daniel Schneider and Dr.-Ing. Andreas Prahs for their guidance and valuable discussions, without which my research would not have been possible.

I would also like to thank my colleagues for the numerous collegial discussions and impulses. I particularly want to highlight Dr. Ing. Felix Schwab, Martin Reder, Dr. Ing. Michael Späth, and Dr. Ing. Christoph Herrmann. Furthermore, I would like to thank our administrative staff and the secretariat, especially Inken Heise and Christof Ratz, for their technical and administrative support. And last but not least, I would like to thank my family and all my friends who have encouraged and supported me at all stages of my journey over the last few years.

Karlsruhe, September 2023

*Lukas Schöller*

# Contents

<b>Kurzfassung</b> . . . . .	<b>i</b>
<b>Abstract</b> . . . . .	<b>iii</b>
<b>Acknowledgements</b> . . . . .	<b>v</b>
<b>List of abbreviations and symbols</b> . . . . .	<b>xi</b>
<b>1 Introduction</b> . . . . .	<b>1</b>
1.1 Motivation and objectives . . . . .	1
1.2 Notation and conventions . . . . .	7
1.3 Outline of the thesis . . . . .	9
<b>2 Selected fundamentals</b> . . . . .	<b>11</b>
2.1 Composite materials and compression molding process . . . . .	11
2.2 Continuum mechanics . . . . .	14
2.2.1 Kinematics . . . . .	14
2.2.2 Balance laws . . . . .	16
2.2.3 Infinitesimal deformation . . . . .	18
2.2.4 Material theory . . . . .	19
2.3 Phase-field modeling . . . . .	21
2.3.1 Free energy . . . . .	21
2.3.2 Evolution equation . . . . .	23
2.3.3 Considering mechanical jump conditions . . . . .	24
2.4 Linear elastic fracture mechanics . . . . .	26
2.5 Molecular dynamics . . . . .	28
2.5.1 Lagrange equations . . . . .	29
2.5.2 Microcanonical ensemble . . . . .	30

2.5.3	Isobaric-isothermal ensemble . . . . .	31
2.5.4	Potential energy function . . . . .	32
<b>3</b>	<b>Two-stage polymerization using molecular dynamics . . .</b>	<b>35</b>
3.1	Constituents . . . . .	36
3.1.1	Glass fiber surface . . . . .	36
3.1.2	Resin system . . . . .	37
3.1.3	Fiber sizing . . . . .	39
3.2	Molecular modelling description . . . . .	42
3.2.1	Fiber surface . . . . .	42
3.2.2	Reaction algorithms . . . . .	44
3.3	Results . . . . .	45
3.3.1	Fiber surface . . . . .	48
3.3.2	Sizing layer . . . . .	49
3.3.3	Condensation reaction . . . . .	51
3.3.4	Pure resin layer . . . . .	52
3.3.5	Complete system . . . . .	53
3.3.6	Polyurethane reaction . . . . .	55
3.3.7	Radical polymerization . . . . .	57
3.4	Interim conclusion . . . . .	61
<b>4</b>	<b>Structure generator for FRPs . . . . .</b>	<b>63</b>
4.1	Fiber description . . . . .	64
4.2	Results . . . . .	67
<b>5</b>	<b>Curing simulations of FRTS on a micro scale . . . . .</b>	<b>73</b>
5.1	Model . . . . .	73
5.2	Results . . . . .	78
5.2.1	Pure resin . . . . .	81
5.2.2	Unidirectional fiber-reinforced . . . . .	82
5.2.3	Two-dimensional curved fibers . . . . .	84
5.2.4	Three-dimensional curved fibers . . . . .	85
5.2.5	Comparison . . . . .	86

---

<b>6 Phase-field modeling of crack propagation in heterogeneous materials</b>	<b>89</b>
6.1 Phase-field crack propagation models	90
6.1.1 Classical homogeneous model	90
6.1.2 Heterogeneous single-crack order parameter model	94
6.1.3 Heterogeneous multi-crack order parameter model	98
6.1.4 Comparison	101
6.2 Numerical treatment	104
6.3 Extension to a single-obstacle potential	107
6.4 Results	109
6.4.1 Steady-state profiles in 1D	109
6.4.2 Sloped binary interface	112
6.4.3 Single inclusion problem	121
6.4.4 Application to FRPs	128
6.5 Interim conclusion	135
<b>7 Crack formation during curing of FRTS</b>	<b>137</b>
7.1 Optimal choice of mobility	137
7.2 Results	139
<b>8 Conclusion and outlook</b>	<b>149</b>
<b>A Appendix</b>	<b>155</b>
A.1 Intermolecular interaction potentials	155
A.2 Two-stage polymerization	158
A.3 Phase-field modeling of crack propagation	160
<b>Bibliography</b>	<b>163</b>
<b>List of the author's publications</b>	<b>187</b>
<b>List of Figures</b>	<b>189</b>
<b>List of Tables</b>	<b>195</b>



# List of abbreviations and symbols

## Abbreviations

1D / 2D / 3D	One / two / three dimensional
AMR	Adaptive mesh refinement
CZM	Cohesive zone modeling
DEM	Discrete element method
FEM	Finite element method
GFEM	Generalized finite element method
LEFM	Linear elastic fracture mechanic
MD	Molecular dynamics
PFM	Phase-field method
XFEM	Extended finite element method
MCOP	Multi-crack order parameter
SCOP	Single-crack order parameter
FRP	Fiber-reinforced polymer
FRTS	Fiber-reinforced thermoset
GF	Glass fiber
PU	Polyurethane
SMC	Sheet molding compound
TS	Thermoset
UP	Unsaturated polyester

UPPH	Unsaturated polyester polyurethane hybrid
NPT	Isobaric-isothermal ensemble
NVE	Microcanonical ensemble
SIP	Single inclusion problem
(P-)MDI	(Poly)methylene diphenyl thiocyanate
$\gamma$ -MPS	$\gamma$ -methacryloxypropyltrimethoxysilane
IPN	Interpenetrating polymer network
KDE	Kernel density estimator

## Scalars

$\eta$	Specific entropy
$\psi$	Helmholtz free energy
$\rho$	Mass density
$\theta$	Absolute temperature
$e$	Specific internal energy
$r$	Specific heat source
$f_{el}$	Strain energy density
$f$	Free energy density
$\lambda, \mu$	Lamé parameters
$\nu$	Poisson's ratio
$E$	Young's modulus
$G$	Shear modulus
$K$	Bulk modulus
$\sigma^1, \sigma^2, \sigma^3$	Principal stresses
$\sigma^*$	Maximum absolute principal stress
$\sigma_{vM}$	von Mises equivalent stress

$\phi_c$	$N$ -tuple of crack order parameters
$\phi$	$N$ -tuple of order parameters
$\phi$	Order parameter
$\phi_c$	Crack order parameter
$\tilde{\phi}_c$	Effective Crack order parameter
$\varepsilon_{\phi_c}$	Interface parameter of the crack phasefield
$\varepsilon_{\phi_s}$	Interface parameter of the phasefield
$\gamma$	Surface energy density
$h^\alpha$	Interpolation function
$M$	Mobility
$K_I, K_{II}, K_{III}$	Stress intensity factors
$K_{Ic}, K_{IIc}, K_{IIIc}$	Fracture toughness
$G$	Energy release rate
$G_c$	Critical energy release rate
$\zeta$	Curing degree
$\alpha$	Thermal expansion coefficient
$\chi_r$	Total curing shrinkage
$\kappa$	Isotropic thermal conductivity
$\theta^g$	Glass transition temperature
$\theta_{\text{ref}}$	Reference temperature
$c_V$	Specific heat capacity at constant volume
$E^1, E^2$	Activation energies
$h^{\text{tot}}$	Total reaction enthalpy
$t, \Delta t$	Time, time step width
$v_f$	Fiber volume fraction
$k_B$	Boltzmann constant
$R$	Universal gas constant

## Vectors

$X$	Reference position vector
$x$	Current position vector
$v$	Velocity vector
$a$	Acceleration vector
$u$	Displacement vector
$b$	Body force vector
$t$	Traction vector
$g$	Temperature gradient
$q$	Heat flux vector
$f$	Force vector
$n$	Normal vector

## 2<sup>nd</sup> order tensors

$\mathbf{1}$	Identity tensor
$F$	Deformation gradient
$H$	Displacement gradient
$E^G$	Green's strain tensor
$\varepsilon$	Infinitesimal strain tensor
$\varepsilon_{el}$	Infinitesimal elastic strain tensor
$\varepsilon_{\theta}$	Infinitesimal thermal strain tensor
$\varepsilon_{\chi}$	Infinitesimal curing shrinkage strain tensor
$\sigma$	Cauchy stress tensor
$\sigma'$	Deviatoric stress tensor
$\sigma^{\circ}$	Spherical stress tensor
$A$	2 <sup>nd</sup> order fiber orientation tensor

**4<sup>th</sup> order tensors**

$\mathbb{C}$  Stiffness tensor

**Others**

$\Omega$  Material body

$\partial\Omega$  Boundary of the material body

$S$  Singular surface

$S_c$  Sharp crack surface

$\mathcal{F}$  Free energy functional

$\mathcal{G}_\phi$  Gibbs simplex

$\mathcal{L}$  Lagrangian

$K$  Kinetic energy

$U$  Potential energy



# 1 Introduction

## 1.1 Motivation and objectives

Glass fiber-reinforced polymers are increasingly important in industrial applications due to their lightweight potential at relatively low cost. They combine the high strength of glass fibers with the durability of, for example, thermosets. A novel unsaturated polyester polyurethane hybrid (UPPH) resin system allows co-molding of continuous fiber-reinforced polymers in e.g. compression molding. The relatively low cycle times allow a wide range of uses, such as in automotive applications [6, 7]. Understanding the behavior of such a composite, including manufacturing and possible damage during this process, is essential for designing safe and reliable products.

Fiber-reinforced thermosets (FRTS) contain structures on of different length scales, cf. Figure 1.1. Starting with the nano length scale where individual atoms are resolved and the interfaces between fiber, resin and fiber sizing take place. A well-established method for this scale is molecular dynamics, for which a approach for investigating the fiber-sizing-resin interface during polymerization will be presented in this work. At the micro length scale, the individual fibers are resolved. Based on continuum mechanics and the phase-field method, the fracture during the curing process will be studied. The meso length scale deals with whole fiber bundles, while the marco length scale represents the entire FRTS component.

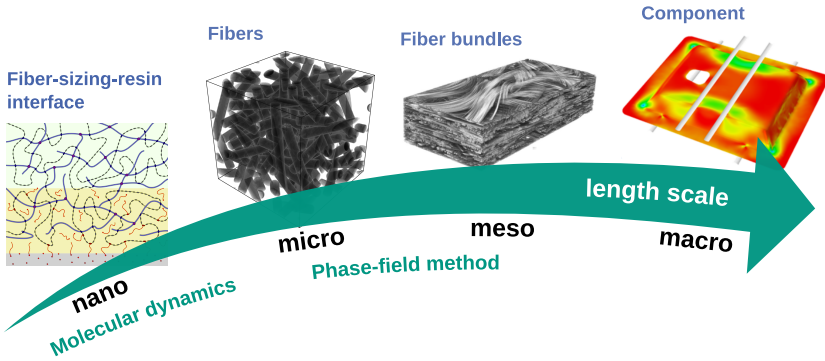


**Figure 1.1:** The different length scales of fiber-reinforced thermosets and their corresponding different computational methods used in this work. With images reprinted with permission from [8, 9].

**Crack propagation modeling<sup>1</sup>** Understanding failure and fracture behavior is a challenge in modern engineering and materials science, especially when considering the growing number of materials with a complex morphology and heterogeneous material properties, such as fiber-reinforced polymers (FRP). Predicting the resistance to failure and the complex crack propagation paths of such materials will improve the ability to determine effective load capacities and to develop efficient, safe, and predictable products. Linear Elastic Fracture Mechanics (LEFM) has proven to be capable of describing crack propagation in homogeneous materials in 2D [10, 11]. An extension to heterogeneous materials is possible [12, 13], but a general approach which describes complex heterogeneous materials in 3D seems difficult and not feasible. An alternative approach is cohesive zone modeling (CZM), introduced by Barenblatt [14] and Dugdale [15], which can be embedded in the finite element method (FEM), using cohesive finite elements. An overview of CZM can be found in Elices et al. [16]. Since these models demand conforming meshes,

<sup>1</sup>The content of this section has been taken directly from Schöller et al. [1, 3] with minor linguistic changes.

more advanced crack paths requires cumbersome remeshing methods. In comparison, the generalized/extended finite element method (GFEM/XFEM) enriches the solution space of the FEM to handle discontinuous functions [17]. This eliminates the need for conforming meshes and remeshing. However, both CZM and GFEM/XFEM are limited to describe complex crack propagation behavior, including nucleation, branching, or the interaction between cracks. In a domain with sharp interfaces, different regions, e.g., phases or destroyed and unbroken material, occurring in the case of fracture, are distinctly separated, cf. e.g., Prahs and Böhlke [18], in the context of interface conditions on a sharp interface. This requires explicit tracking of the interface, which has proven impractical.

**Phase-field crack propagation models<sup>1</sup>** An alternative approach to fracture utilizes the phase-field method (PFM), introducing order parameters to allow a smooth transition between various regions. This results in continuous order parameter fields, often referred as phasefields, and allows an implicit tracking of the interface on nonconforming meshes, and thus an efficient numerical treatment of singularities, such as grain boundaries or cracks. Thus, the PFM is widely established to describe the evolution of microstructures, such as solidification or solid-solid phase transitions, including consideration of different types of physical aspects, e.g., thermodynamics, chemistry, or mechanics [19–23]. Phase-field approaches to brittle fracture have been developed in both the physical [24–26] and the mechanical community [27–29]. The latter is based on Griffith’s theory [30] and the variational formulation of Francfort and Marigo [31] and Francfort and Bourdin et al. [32]. Other more advanced applications, for example, deal with plasticity [33–36] or multiphysics [37–40]. For most of these models, the material is considered homogeneous. This is a reasonable assumption on macroscopic length scales. Often, however, failure mechanisms occur at smaller length scales, where many materials are heterogeneous. Therefore, models that are able to describe fracture of heterogeneous systems are highly desirable.

**Crack propagation in heterogeneous materials**<sup>1</sup> Most phase-field models describing crack propagation in such systems introduce a varying crack surface energy. This is achieved either by anisotropy [41, 42] or interpolation of the surface energy [43, 44]. Schneider et al. [45] proposed a model that extends the multiphase-field model of Nestler et al. [46], so as to describe crack propagation in polycrystalline systems. The model takes into account damage due to a phase transition to a common crack phase. This concept has also been extended to anisotropy [47] and plasticity [48]. A common approach to consider an interfacial fracture toughness is to lower the crack resistance in the interfacial region. Hansen-Dörr et al. [49, 50], for instance, model a locally varying value based on a virtual phase transition. To account for interfacial effects, CZM have also been introduced into phase-field crack propagation models [51–54]. Although these models can describe complex crack propagation in heterogeneous materials, including interfacial effects, and agree with the LEFM and experiments, they can lead to non-physical behavior as discussed by Henry [55].

An objective of this work is to introduce a novel multi-crack order parameter (MCOP) phase-field model for fracture which is able to overcome issues of the established single-crack order parameter (SCOP) approaches for modeling crack propagation in heterogeneous systems based on the phase-field method. Therefore, some issues of the SCOP model are illustrated in simple 1D and 2D simulation setups and several advantages of the novel model are demonstrated. Moreover, the work at hand is to extend this model by incorporating a more sophisticated scheme for the underlying homogenization problem [56–61]. Therefore, the work of Schneider et al. [60] is applied to the MCOP model. Finally, an exemplary FRP system is used to demonstrate the limitations of the basic scheme and the advantages of the proposed model, where the homogenization scheme is based on mechanical jump conditions.

**The role of fiber sizing<sup>2</sup>** Besides the matrix material and the fiber, the sizing (fiber coating) plays a crucial role in the manufacturing and performance of FRPs. The fiber size consist of multiple components and fulfills a variety of tasks, such as protection of the fiber, improvement of the fiber handling, or enhancement of the adhesive bonding of fiber and matrix [62]. Early investigations considering the sizing were conducted by Plueddemann [63, 64] and Loewenstein [65]. They mainly focus on the coupling agent, which provides the functionality of bonding to both the glass fiber and the resin. In the literature, Thomason [66–68], Gao and Mäder [69] and Liu et al. [70], among others, examined the sizing of glass fibers with different sizing formulations and using various approaches. Furthermore, Karger-Kocsi et al. [71] summarize recent advances in interphase technology for several fibers, and matrix materials, as well as sizes. Also, Thomason [62] recently gave a detailed overview of glass fiber sizing. He pointed out that the actual sizing is always a proprietary secret that leads to a lack of understanding of the fiber sizing, especially since the knowledge is very fragmented. As the fiber interphase is a common point of failure in FRPs, through mechanisms such as fiber pull-out and fiber debonding, this lack of knowledge is a severe impediment to improving these materials. Moreover, fiber interphase has been mostly studied in the literature based on an experimental approach. In contrast, few investigations have been conducted based on simulative approaches. Therefore, modeling of the fiber-resin interphase, including the sizing, e.g. based on molecular dynamics, is highly desirable as it provides insights into the interphase and could improve the understanding of FRP. In particular, regarding their manufacturing, performance, or failure mechanism, this could lead to an improvement of this whole class of materials.

---

<sup>2</sup>The content of this section has been taken directly from Schöller et al. [2] with minor linguistic changes.

Only a few attempts to investigate the interface between fiber and matrix, based on molecular dynamics (MD), can be found in the literature. While the interphase between carbon fibers was examined [72–74], including the fiber sizing [75], no investigation of the interphase for glass fibers and their sizing have been conducted so far. Insight into the formation of the network during the polymerization, in combination with the fiber size, could improve the understanding of sizing extensively.

**Curing of FRTSs** During the processing of FRTS, e.g. compression molding, the resin material undergoes a chemical reaction. The formation of the final polymer structure gives the component its final strength and properties, such as mechanical stiffness. Accompanying the chemical reaction, the curing process, is a chemical shrinkage. Together with a thermal expansion due to the higher temperature, the microstructure can already exhibit stresses during this manufacturing process. In particular, the high contrast between the thermal, chemical and mechanical material behavior of fiber and matrix can cause damage at this stage. Even if a complete failure of the component does not occur, microcracks may occur, e.g. at the fiber-resin interface. This damage can affect the overall performance of the component and therefore its service life. Understanding the mechanism of crack formation at the length scale of individual fibers is therefore of great interest.

In this work, a structure generator for curved fibers is introduced. Using such volume elements and material properties derived from the study of the resin system with molecular dynamics simulations [76], curing simulations are performed. Subsequently, the distribution of mechanical and thermal quantities will be compared for different levels of abstraction of the real microstructure as well as for different fiber volume fractions. Finally, the combination of the novel MCOP model with the mechanical jump condition framework, cf. eg. [60], allows the prediction of microcrack formation during the curing process of glass fiber-reinforced UPPH resin.

**Objectives** The main objectives and novelties of this work are listed in the following:

- The two-stage polymerization process of the UPPH resin is studied by molecular dynamics simulations. In contrast to Schwab and Denniston [76], the glass fiber and sizing are also considered, and the evolution of various quantities during polymerization along the fiber-sizing-resin interface is examined.
- A volume element generator for long curved fibers is developed based on molecular dynamics and the discrete element method.
- The curing process of UPPH in such glass fiber-reinforced volume elements is studied and stresses due to thermal and chemical strains are discussed.
- A novel phase-field crack propagation model based on multiple crack order parameters is developed. It is demonstrated that it provides qualitatively and quantitatively better predictions of crack formation in heterogeneous materials than established models.
- In the novel MCOP, the mechanical jump condition framework [22] is incorporated. The advantages of such an extension are shown, e.g., by crack formation around a single inclusion problem.
- Crack propagation in FRTS is studied. External displacement boundary conditions are used to demonstrate the advantages of the MCOP as well as the jump condition framework. Finally, crack initiation during curing of glass fiber-reinforced UPPH resin is predicted using the novel model.

## 1.2 Notation and conventions

In this work, a symbolic notation for tensors is used: Scalar-valued quantities are denoted by a normal font, e.g.  $a, b$ . Furthermore are 1<sup>th</sup> and 2<sup>nd</sup> order

tensors, or vectors, denoted by bold symbols, e.g.  $\mathbf{a}$ ,  $\mathbf{B}$ . In addition, 4<sup>th</sup> order tensors are denoted by double-strike symbols, e.g.  $\mathbb{C}$ . The tensors are restricted to an orthonormal basis (ONB)  $\{\mathbf{e}_x, \mathbf{e}_y, \mathbf{e}_z\}$  with the unit vectors  $\mathbf{e}_i \forall i = x, y, z$ . Greek letters, e.g.  $\alpha, \beta$ , are used to denote phase indices in the context of the phase-field model.

**Operations** The scalar product is denoted by  $\mathbf{a} \cdot \mathbf{b}$  and  $\mathbf{A} \cdot \mathbf{B}$  for vectors  $\mathbf{a}, \mathbf{b}$  or 2<sup>nd</sup> order tensors  $\mathbf{A}, \mathbf{B}$ , respectively. A linear mapping of a 2<sup>nd</sup> order tensor  $\mathbf{A}$  and a vector  $\mathbf{b}$  is defined by  $\mathbf{A}\mathbf{b}$ , and for a 2<sup>nd</sup> order tensor  $\mathbf{A}$  and a 4<sup>th</sup> order tensor  $\mathbb{C}$  by  $\mathbb{C}[\mathbf{A}]$ . The dyadic product of two vectors follows by  $\mathbf{a} \otimes \mathbf{b}$ . The vector norm can be written with  $|\mathbf{a}| = \sqrt{\mathbf{a} \cdot \mathbf{a}}$ , and the tensorial Frobenius norm analogously with  $|\mathbf{A}| = \sqrt{\mathbf{A} \cdot \mathbf{A}}$ . The inverse of a tensor  $\mathbf{A}$  is denoted by  $\mathbf{A}^{-1}$  and the transposed tensor by  $\mathbf{A}^T$ . The trace of a 2<sup>nd</sup> order tensor  $\mathbf{A}$  is defined by  $\text{tr}(\mathbf{A}) = \mathbf{A} \cdot \mathbf{1}$ , where the 2<sup>nd</sup> order identity tensor is  $\mathbf{1}$ .

**Derivatives** Total derivatives are denoted by  $\frac{d\mathbf{a}}{dx}$  for a vector  $\mathbf{a}$  with respect to  $x$ , while partial derivatives are denoted by  $\frac{\partial \mathbf{a}}{\partial x}$ . The derivatives respectively apply to any tensorial order of the numerator or denominator. For the temporal derivative the abbreviation  $\dot{\phi} = \frac{d\phi}{dt}$  for an arbitrary field  $\phi$  and time  $t$  is introduced. The spatial gradient  $\frac{\partial \phi}{\partial \mathbf{x}}$  with respect to a position vector  $\mathbf{x}$  can be written by  $\text{grad}(\phi)$  or using the nabla operator with  $\nabla \phi$ . The divergence of a vector field  $\mathbf{a}$  is denoted by  $\text{div}(\mathbf{a}) = \text{grad}(\mathbf{a}) \cdot \mathbf{1}$  or  $\nabla \cdot \mathbf{a}$  and can also be extended to higher tensorial orders. The Laplacian operator is defined by  $\Delta \phi = \text{div}(\text{grad}(\phi))$ .

## 1.3 Outline of the thesis

This dissertation is organized as follows: Selected fundamentals of composite materials, continuum mechanics, phase-field modeling, fracture mechanics and molecular dynamics are introduced in Chapter 2. Subsequently, in Chapter 3, the two-stage polymerization of the fiber resin system considered is investigated using molecular dynamics. In order to study this curing process at the micro scale, a structure generator for curved fibers in FRPs is established in Chapter 4. Based on the generated structures, micro-scale curing simulations are performed and the corresponding curing model is formulated in Chapter 5. In order to be able to describe crack propagation in such a heterogeneous system, different crack propagation models based on phase-field modeling are presented in Chapter 6. These are qualitatively and quantitatively compared, resulting in a novel crack propagation model for heterogeneous systems, including advanced homogenization schemes. The ability of the model to predict crack propagation in FRPs is demonstrated and finally applied to the compression molding process of glass fiber-reinforced UPPH resin in Chapter 7. Thereby, the loading due to thermal expansion and chemical shrinkage on the micro-length scale is considered. Finally, conclusions and a outlook are given in Chapter 8.



## **2 Selected fundamentals**

### **2.1 Composite materials and compression molding process**

A composite material consists of two or more components. Typically, the components have significantly different material properties, such as chemical or mechanical properties and are often composed of materials of different classes, such as steel-reinforced concrete, fiber-reinforced ceramics, or fiber-reinforced polymers. The general idea of a composite material is to combine the constituents to get a composite material with better effective properties. For example, for fiber-reinforced polymers (FRP), the matrix materials primarily embed the fibers, transfer loads and protect the fibers. In contrast, the fibers mainly provide the strength and stiffness of the composite. The effective strength is significantly increased compared to the pure matrix materials, while other properties, e.g. chemical resistance, may be reduced compared to a pure glass.

In this work, FRPs, in particular fiber-reinforced thermosets (FRTS), are considered in the context of the compression molding process, which is briefly introduced in the following. The reader is referred to [7, 77] for a more comprehensive introduction to FRTS and the compression molding process.

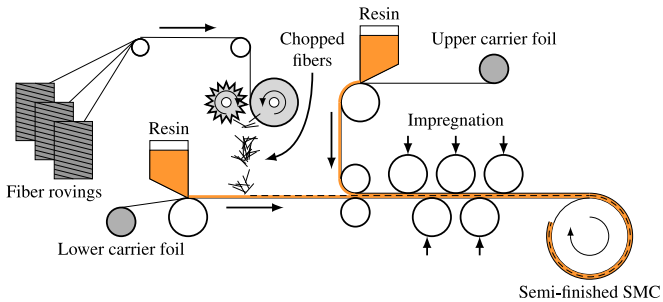


**Figure 2.1:** Manufacturing process of semi-finished sheet molding compound (SMC). Reprinted from [78].

**Glass fiber-reinforced UPPH<sup>1</sup>** Fiber-reinforced polymers are increasingly important in industrial applications, including aerospace, automotive, marine, and construction industries. The majority of these are glass fiber-reinforced polymers, probably due to the relatively low cost while still offering good performance. A relatively new thermoset matrix material in this context is the unsaturated polyester polyurethane hybrid (UPPH) resin system. It combines a polyurethane (PU) polyaddition with a radical polymerization of unsaturated polyester (UP), resulting in a two-step reaction of the thermoset. The hybrid networks formed by this copolymerization increase overall properties such as crack resistance, tensile strength and toughness [6]. There is therefore increasing interest in using this material in industrial applications such as the automotive industry [7].

**Compression molding process** For FRPs, the choice of manufacturing process is often based on the fiber aspect ratio, i.e., the ratio of fiber length to diameter. Depending on the ratio, different high shear stresses can occur

<sup>1</sup>The content of this section has been taken directly from Schöller et al. [2] with minor linguistic changes.

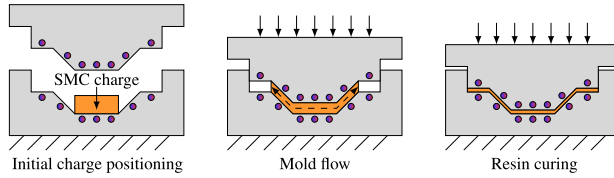


**Figure 2.2:** The compression molding process: Placing the SMC initial charge, compression molding and finally, curing of the resin. Reprinted from [78].

during the processes, which prevents a free choice of the manufacturing process. In this work, the compression molding process is chosen because it also allows the co-molding of continuous fiber-reinforced polymers as local reinforcements, leading to continuous-discontinuous FRPs. This class of composites combines the possibility of complex structures of discontinuous fiber-reinforced polymers with the high strength and stiffness of continuous fiber-reinforced polymers and offers an immense weight saving potential. In this context, compression molding allows low cycle time and therefore low cost.

The compression molding process of FRTS uses a prepreg, a sheet molding compound (SMC). To produce the SMC, the resin is mixed and applied evenly to two films through doctor boxes. Chopped glass fibers are then dropped randomly onto the films. The films are then joined and the resin cures during a polyurethane reaction to a so-called B-stage, cf. Figure 2.1. The finished SMC can be easily transported and cut to size. After the films are removed, the charge is placed in the press onto the hot molds. By closing the molds, pressure and heat are applied and the SMC charge flows into its final shape and radical polymerization takes place, curing the part to its final strength, cf. Figure 2.2. After the molds are opened, the part is removed and cooled to room temperature for further processing. An example of the final microstructure is shown in Figure 2.3. The chopped fiber roving, consisting of hundreds of individual fibers, can be identified in the CT scan. Based on the flow direction, the bundles may have a preferred direction. Thus, a planar distribution is observed in the CT scan due to the planar geometry of the final component.

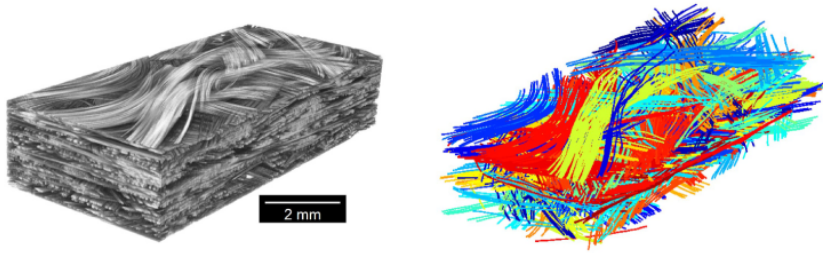


**Figure 2.3:** 3D visualization of the tracked and clustered SMC fiber bundles. Only clustered fiber bundles with a minimum of 100 sub-bundles are visualized. Reprinted with permission from [9]. Copyright 2021 Elsevier.

## 2.2 Continuum mechanics

This section gives a brief introduction to continuum mechanics, mainly following Altenbach [79] and Bertram and Glüge [80]. For more detailed fundamentals of continuum mechanics, the reader is referred to e.g. [79–84]. In continuum mechanics, material bodies are considered which continuously occupy a region in three-dimensional Euclidean space  $\mathbb{R}^3$  by an infinite number of material points. This work is restricted to Cauchy-Boltzmann continua, for which each material point has three translational degrees of freedom and, for example, no rotational degrees of freedom.

### 2.2.1 Kinematics

A material body  $\Omega$  with a boundary  $\partial\Omega$  and a unit normal vector  $\boldsymbol{n}$  directed outwards is considered. Any material point within  $\Omega$  can be described by a position vector  $\boldsymbol{X}$  at a reference time  $t_0$  in a reference configuration. The position vector at a time  $t > t_0$  can be described by

$$\boldsymbol{x} = \boldsymbol{\chi}(\boldsymbol{X}, t) \quad (2.1)$$

in the current configuration by the motion function

**Deformation** The gradient of the motion  $\chi$  with respect to the reference configuration

$$\mathbf{F} = \frac{\partial \chi(\mathbf{X}, t)}{\partial \mathbf{X}} \quad (2.2)$$

is called the deformation gradient and describes the transformation of a line element  $d\mathbf{X}$  of the reference configuration into a line element  $d\mathbf{x}$  in the current configuration by

$$d\mathbf{x} = \mathbf{F} d\mathbf{X}. \quad (2.3)$$

In addition, the transformation of an area element  $d\mathbf{A}$  and a volume element  $dV$  of the reference configuration into elements of the current configuration ( $d\mathbf{a}, dv$ ) follows by

$$d\mathbf{a} = \det(\mathbf{F}) (\mathbf{F}^T)^{-1} d\mathbf{A}, \quad (2.4)$$

$$dv = |\det(\mathbf{F})| dV. \quad (2.5)$$

The difference between the reference and current position vector yields the displacement vector

$$\mathbf{u} = \chi(\mathbf{X}, t) - \mathbf{X}, \quad (2.6)$$

and time derivative of the motion  $\chi$  the velocity vector

$$\mathbf{v} = \frac{\partial \chi(\mathbf{X}, t)}{\partial t}. \quad (2.7)$$

The gradient of the displacement vector with respect to the reference configuration

$$\mathbf{H} = \frac{\partial \mathbf{u}}{\partial \mathbf{X}} = \mathbf{F} - \mathbf{1} \quad (2.8)$$

is called the displacement gradient and can also be directly related to the deformation gradient with the identity tensor  $\mathbf{1}$ .

**Strain measures** Based on a polar decomposition of the deformation gradient the symmetric Green's strain tensor

$$\mathbf{E}^G = \frac{1}{2} (\mathbf{F}^T \mathbf{F} - \mathbf{1}) \quad (2.9)$$

can be defined, which is independent of rigid body motion, and therefore is a common strain measure for finite deformation. The symmetric infinitesimal strain tensor

$$\boldsymbol{\varepsilon} = \frac{1}{2} (\mathbf{H} + \mathbf{H}^T), \quad (2.10)$$

is the linearized variant of  $\mathbf{E}^G$ , which is only independent of translational rigid body motion, not to rotational rigid body motion and is therefore often used in the context of small deformations.

## 2.2.2 Balance laws

This section considers sufficiently smooth physical fields without singular surfaces. For a discussion of continua with material singular surfaces, the reader is referred to e.g. Prahs and Böhlke [18].

**Balance of linear momentum** The balance of linear momentum can be written by

$$\frac{d}{dt} \int_{\Omega} \rho \mathbf{v} \, dv = \int_{\Omega} \rho \mathbf{b} \, dv + \int_{\partial\Omega} \mathbf{t} \, da, \quad (2.11)$$

with the mass density  $\rho$ , and implies that the change of linear momentum  $\int_{\Omega} \rho \mathbf{v} \, dv$  is equal to the forces of a body force vector  $\mathbf{b}$  and the traction vector  $\mathbf{t}$ .

The *Theorem of Cauchy* states that the traction vector is given by

$$\mathbf{t} = \boldsymbol{\sigma} \mathbf{n}, \quad (2.12)$$

with the normal vector  $\mathbf{n}$  and the Cauchy stress tensor  $\boldsymbol{\sigma}$  [80]. For the static case and when no body force is present, the local balance of linear momentum can be written by

$$\operatorname{div}(\boldsymbol{\sigma}) = \mathbf{0}. \quad (2.13)$$

Furthermore, the balance of angular momentum is satisfied with the symmetry of the stress tensor

$$\boldsymbol{\sigma} = \boldsymbol{\sigma}^T, \quad (2.14)$$

as stated by *Boltzmann's axiom* [80].

**First law of thermodynamics** The first law of thermodynamics, or the balance of total energy, can be defined by

$$\frac{d}{dt} \int_{\Omega} \rho \left( e + \frac{1}{2} \mathbf{v} \cdot \mathbf{v} \right) dv = \int_{\Omega} \rho (\mathbf{b} \cdot \mathbf{v} + r) dv + \int_{\partial\Omega} (\mathbf{t} \cdot \mathbf{v} - \mathbf{q} \cdot \mathbf{n}) da, \quad (2.15)$$

with the specific internal energy  $e$ , a specific heat source  $r$  and the heat flux vector  $\mathbf{q}$ . Therefore, the change in total energy, the sum of internal and kinetic energy, is equal to the power of a volumetric and surface forces and the heat supplied by a heat source and flux.

**Second law of thermodynamics** The first law of thermodynamics provides a balance of total energy, but it does not state how energy can be converted, nor in what direction. Therefore, the second law of thermodynamics is given by

$$\frac{d}{dt} \int_{\Omega} \rho \eta dv - \int_{\Omega} \rho \frac{r}{\theta} dv + \int_{\partial\Omega} \frac{\mathbf{q}}{\theta} \cdot \mathbf{n} da \geq 0, \quad (2.16)$$

with the absolute temperature  $\theta$ , the specific entropy  $\eta$ , and states that the entropy production of a body is never greater than its entropy change due to the

heat flux and the heat source. In combination with the first law of thermodynamics, the localized Clausius-Duhem inequality (CDI)

$$\boldsymbol{\sigma} \cdot \boldsymbol{\varepsilon} - \rho \dot{\psi} - \rho \eta \dot{\theta} - \frac{\mathbf{q} \cdot \mathbf{g}}{\theta} \geq 0 \quad (2.17)$$

with the Helmholtz free energy  $\psi = e - \theta \eta$  and the temperature gradient  $\mathbf{g} = \partial \theta / \partial \mathbf{X}$  can be formulated. This inequality equation imposes restrictions on the constitutive equations describing the material response, e.g. by following the work of Coleman and Noll [85].

### 2.2.3 Infinitesimal deformation

The deformation of a body is infinitesimal, or small, if

$$|\mathbf{H}| \ll |\mathbf{1}| \quad (2.18)$$

is fulfilled. And therefore, e.g. the strain tensor can be approximated by the geometrically linearized variant

$$\mathbf{E}^G \approx \boldsymbol{\varepsilon}. \quad (2.19)$$

Furthermore, for the gradient of an arbitrary field  $\psi$  with respect to the reference and current configuration,

$$\frac{\partial \psi}{\partial \mathbf{X}} \approx \frac{\partial \psi}{\partial \mathbf{x}}, \quad \rho \approx \rho_0 \quad (2.20)$$

applies.

## 2.2.4 Material theory

The balance of linear momentum (2.13) contains nine unknown physical fields, three displacement and six stress components, but only provides three equations. Therefore, six additional constitutive equations have to be formulated to relate the material response, hence the stresses, to the kinematic measures. In addition, some basic principles about the material behavior are postulated in the following [80].

- **Principle of Determinism:** The stresses at a material point are defined only by the displacement field of the body in the past and in the present.
- **Principle of Invariance under Superimposed Rigid Body Motions:** The stresses are not directly caused by translations or rotations of the body.
- **Principle of Local Action:** The stresses in a material point are determined by the motion of only a finite neighborhood of that point.

**Hooke's law** The materials in this work are assumed to be elastic, which describe materials for which the current stresses depend only on the current deformations [80]. In the context of small deformations, the linear mapping of strain to stress tensor

$$\boldsymbol{\sigma} = \mathbb{C}[\boldsymbol{\varepsilon}], \quad (2.21)$$

with the 4<sup>th</sup> order stiffness tensor  $\mathbb{C}$ , is the *Hooke's law* in a general anisotropic form. The strain energy density follows by the quadratic form

$$f_{\text{el}} = \frac{1}{2} \mathbb{C}[\boldsymbol{\varepsilon}] \cdot \boldsymbol{\varepsilon}, \quad (2.22)$$

and the stress and stiffness can also be described by the potential relations

$$\boldsymbol{\sigma} = \frac{\partial f_{\text{el}}}{\partial \boldsymbol{\varepsilon}}, \quad \mathbb{C} = \frac{\partial^2 f_{\text{el}}}{\partial \boldsymbol{\varepsilon} \partial \boldsymbol{\varepsilon}} = \frac{\partial \boldsymbol{\sigma}}{\partial \boldsymbol{\varepsilon}}. \quad (2.23)$$

In the isotropic case, Hooke's law can be simplified to

$$\boldsymbol{\sigma} = \lambda \operatorname{tr}(\boldsymbol{\varepsilon}) \mathbf{1} + 2\mu \boldsymbol{\varepsilon}, \quad (2.24)$$

with the *Lamé* parameters  $\lambda$  and  $\mu$ , but can also be related to other elastic moduli, e.g. the *Young's* modulus  $E$  and the *Poisson's* ratio  $\nu$ , cf. e.g. [80].

**Spectral form and principal stresses** The symmetric stress tensor can be rewritten in the spectral form

$$\boldsymbol{\sigma} = \sum_i^3 \sigma^i \mathbf{p}^i \otimes \mathbf{p}^i, \quad (2.25)$$

with the principal stresses  $\sigma^i \forall i = 1, 2, 3$  and the corresponding principal stress axes  $\mathbf{p}^i$ . The numbering of the principal stresses usually follows the convention

$$\sigma^1 \geq \sigma^2 \geq \sigma^3. \quad (2.26)$$

**Stress deviator and von Mises stress** In addition to the spectral form, the stress tensor can also be decomposed into a spherical part  $\boldsymbol{\sigma}^\circ$  and the stress deviator  $\boldsymbol{\sigma}'$  through

$$\boldsymbol{\sigma}^\circ = \frac{1}{3} \operatorname{tr}(\boldsymbol{\sigma}) \mathbf{1}, \quad \boldsymbol{\sigma}' = \boldsymbol{\sigma} - \boldsymbol{\sigma}^\circ. \quad (2.27)$$

Note that for a hydrostatic stress state  $\boldsymbol{\sigma} = -p\mathbf{1}$  at a pressure  $p$ , the deviator part vanishes, i.e.,  $\boldsymbol{\sigma}' = \mathbf{0}$ . Based on the stress deviator, the *von Mises* equivalent stress

$$\sigma_{\text{vM}} = \sqrt{\frac{3}{2}} |\boldsymbol{\sigma}'| \quad (2.28)$$

can be defined, which relates the three-dimensional stress state to a fictive uniaxial stress state.

## 2.3 Phase-field modeling

The phase-field model (PFM) is a well-established approach for describing microstructure evolution on the micro and meso length scales. In a PFM a singular interface is described by a diffuse smooth transition instead of a sharp interface. This avoids a cumbersome explicit tracking of interfaces, which has proven to be unfeasible. In recent years, PFM has been widely used to describe the evolution of microstructures, such as solidification or solid-solid phase transitions, taking into account different types of physical aspects, e.g. thermodynamics, chemistry or mechanics [20–23]. For a comprehensive overview, the reader is referred to e.g. [19].

In this section, a basic multiphase-field model is presented based on the work of Steinbach et al. [86] and Nestler et al. [46]. Many of the extensions to the models that are state of the art nowadays are omitted, since the focus of this work is primarily on the phase-field model in the context of crack propagation. Instead, the model is solely used to parameterize the underlying morphology in a diffuse context. For an introduction to the PFM for crack propagation, the reader is referred to Chapter 6.

### 2.3.1 Free energy

For a material body  $\Omega$  with a singular interface  $S$ , e.g. between two subregions with different material properties, a free energy functional

$$\mathcal{F}[\mathbf{u}] = \int_{\Omega} f_{\text{bulk}}(\mathbf{u}) \, dv + \int_S f_{\text{intf}} \, da \quad (2.29)$$

is introduced. Thus,  $f_{\text{bulk}}$  describes the energy densities of the bulk regions which depends e.g. on the displacement vector  $\mathbf{u}$ . The interfacial energy density  $f_{\text{intf}}$ , e.g., consists of the surface energy density of the surface. With the  $N$ -tuple  $\phi$  of order parameters and their corresponding gradients

$$\phi = \{\phi^1, \phi^2, \dots, \phi^N\}, \quad \nabla\phi = \{\nabla\phi^1, \nabla\phi^2, \dots, \nabla\phi^N\}, \quad (2.30)$$

the free energy can be parameterized by these order parameters, yielding

$$\mathcal{F}[\phi, \nabla\phi, \mathbf{u}] = \int_{\Omega} (f_{\text{bulk}}(\phi, \nabla\phi, \mathbf{u}) + f_{\text{intf}}(\phi, \nabla\phi)) \, \text{d}\mathbf{v} = \int_{\Omega} f \, \text{d}\mathbf{v}. \quad (2.31)$$

When the order parameters  $\phi$  are associated with an indicator functions, both functionals can be considered equivalent. In contrast, for a diffuse and smooth interface, where the order parameter can be considered as the local volume fraction of each subregion, the free energy (2.31) is an approximation of (2.29). The interfacial energy density can be further decomposed by

$$f_{\text{intf}} = f_{\text{pot}} + f_{\text{grad}}, \quad (2.32)$$

into a potential contribution  $f_{\text{pot}}$  and a gradient contribution  $f_{\text{grad}}$ . For the latter various formulation can be found in literature. In the work at hand

$$f_{\text{grad}}(\nabla\phi) = -\varepsilon_{\phi_s} \sum_{\alpha}^N \sum_{\beta>\alpha}^N \gamma_{\alpha\beta} \nabla\phi^{\alpha} \cdot \nabla\phi^{\beta}, \quad (2.33)$$

from Steinbach and Pezzolla [87] is used. Here,  $\varepsilon_{\phi_s}$  is a measure of the width of the diffuse interface and  $\gamma_{\alpha\beta}$  is the surface energy density between a subregion of  $\alpha$  and  $\beta$ . For  $f_{\text{pot}}$ , common choices in the literature are multi-well or multi-obstacle potentials. In this work, the latter is used in the form of

$$f_{\text{pot}}(\phi) = \frac{16}{\varepsilon_{\phi_s} \pi^2} \sum_{\alpha}^N \sum_{\beta>\alpha}^N \gamma_{\alpha\beta} \phi^{\alpha} \phi^{\beta}, \quad (2.34)$$

from Nestler et al. [46]. In addition, the Gibbs simplex

$$\mathcal{G}_\phi = \left\{ \phi \left| \sum_{\alpha}^N \phi^\alpha = 1, \phi^\alpha \geq 0 \forall \alpha = 1, \dots, N \right. \right\} \quad (2.35)$$

must be satisfied. The bulk energy density  $f_{\text{bulk}}$  in this work is limited to the effective strain energy density, which can be decomposed into phase-specific strain densities  $f_{\text{el}}^\alpha$  by

$$f_{\text{bulk}}(\phi, \nabla \phi, \mathbf{u}) = f_{\text{el}}^\alpha = \sum_{\alpha}^N h^\alpha(\phi) f_{\text{el}}^\alpha, \quad (2.36)$$

with an interpolation function  $h^\alpha(\phi)$ , which can be chosen arbitrarily with respect to some restrictions. The most straightforward choice is the order parameter itself,  $h^\alpha(\phi) = \phi^\alpha$ , which will be used in the following work.

### 2.3.2 Evolution equation

To obtain an evolution equation for the order parameters  $\phi$ , a Ginzburg-Landau type evolution equation [88] is introduced. In the context of PFM it is often referred to as the Allen-Cahn evolution equation, cf. Allen and Cahn [89]. Nestler et al. [46] introduced in addition a Lagrange parameter to account for the sum constraint of (2.35), which yields

$$\dot{\phi}^\alpha = \frac{M}{\varepsilon_{\phi_s}} \left( -\frac{\delta \mathcal{F}}{\delta \phi^\alpha} + \frac{1}{N} \sum_{\beta}^N \frac{\delta \mathcal{F}}{\delta \phi^\beta} \right), \quad (2.37)$$

for the temporal evolution of the order parameter of the subregion  $\alpha$ , with a mobility  $M$ . Steinbach and Pezzolla [87] introduced an alternative formulation

$$\dot{\phi}^\alpha = \frac{1}{N \varepsilon_{\phi_s}} \sum_{\beta \neq \alpha}^N M^{\alpha\beta} \left( \frac{\delta \mathcal{F}}{\delta \phi^\alpha} - \frac{\delta \mathcal{F}}{\delta \phi^\beta} \right), \quad (2.38)$$

where dual interactions are considered, allowing for individual mobility  $M^{\alpha\beta}$  for each interaction.

### 2.3.3 Considering mechanical jump conditions<sup>2</sup>

The phase-specific strain energy densities  $f_{\text{el}}^{\alpha}$  are modeled by hyperelastic potentials. Assuming small deformations

$$f_{\text{el}}^{\alpha} = \frac{1}{2} \boldsymbol{\sigma}^{\alpha} \cdot \boldsymbol{\varepsilon}^{\alpha}, \quad \boldsymbol{\sigma}^{\alpha} = \mathbb{C}^{\alpha} [\boldsymbol{\varepsilon}^{\alpha}], \quad (2.39)$$

follows, with the phase-specific infinitesimal strain tensor  $\boldsymbol{\varepsilon}^{\alpha}$  and the stiffness tensor  $\mathbb{C}^{\alpha}$ . In general, the relation between phase-specific strains and the total strain tensor

$$\boldsymbol{\varepsilon} = \sum_{\alpha} \phi^{\alpha} \boldsymbol{\varepsilon}^{\alpha} = \text{sym}(\text{grad}(\mathbf{u})), \quad (2.40)$$

with the displacement vector  $\mathbf{u}$ , is unknown. Using a Voigt-Taylor homogenization scheme,  $\boldsymbol{\varepsilon}^{\alpha} = \boldsymbol{\varepsilon} \forall \alpha = 1, \dots, N$  is assumed. This results in a linear interpolation of the phase-specific parameters, e.g. stiffness. In contrast, Schneider et al. [60] presented a scheme which accounts for the mechanical jump conditions

$$\begin{aligned} \llbracket \mathbf{H} \rrbracket^{\alpha\beta} &= \mathbf{a}^{\alpha\beta} \otimes \mathbf{n}^{\alpha\beta}, & \llbracket \boldsymbol{\sigma} \rrbracket^{\alpha\beta} \mathbf{n}^{\alpha\beta} &= \mathbf{0}, \\ \text{with } \llbracket \boldsymbol{\psi} \rrbracket^{\alpha\beta} &= \boldsymbol{\psi}^{\alpha} - \boldsymbol{\psi}^{\beta}, \end{aligned} \quad (2.41)$$

which was recently also applied to single-crack order parameter phase-field models by Prajapati et al. [47] and Hansen-Dörr et al. [90]. Thereby, the first equation resembles a kinematic compatibility, since the deformation gradient  $\mathbf{H}$  can only exhibit a jump  $\mathbf{a}^{\alpha\beta}$  in normal direction of the singular surface. In contrast, the balance of linear momentum on a material singular surface, c.f.,

---

<sup>2</sup>This section is based on the work of Schöller et al. [3]. Minor linguistic changes and additions have been made.

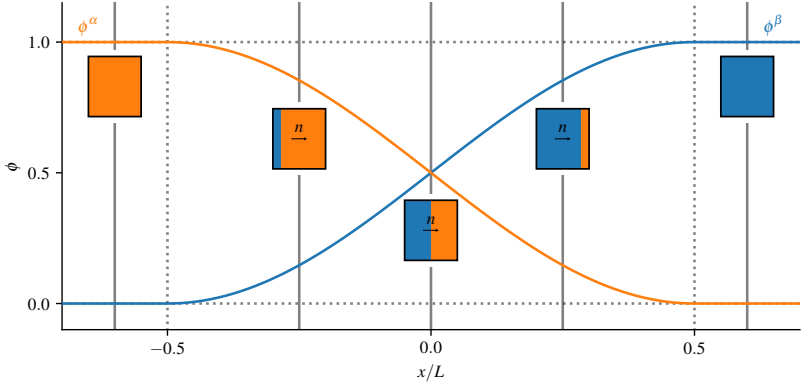


**Figure 2.4:** Schematic representation of a diffuse interface when mechanical jump conditions are considered. Each point of the interface can be associated with a laminate-like structure of different volume fractions of both phases and a normal direction  $\mathbf{n}$ .

e.g., Prahs and Böhlke [18], given by Equation (2.41)b, prohibits a jump of the stress vector normal to the singular surface. Regarding a multiphase-field approach, the normal vector  $\mathbf{n}^{\alpha\beta}$  of the singular surface between phase  $\alpha$  and  $\beta$  and the jump of the infinitesimal strain tensor, regarding the diffuse interface context is given by

$$\llbracket \varepsilon \rrbracket^{\alpha\beta} = \text{sym} \left( \mathbf{a}^{\alpha\beta} \otimes \mathbf{n}^{\alpha\beta} \right), \quad \mathbf{n}^{\alpha\beta} = \frac{\nabla \phi^\alpha - \nabla \phi^\beta}{|\nabla \phi^\alpha - \nabla \phi^\beta|}. \quad (2.42)$$

In order to solve the governing equations, the unknown jump vectors  $\mathbf{a}^{\alpha\beta}$  have to be determined. Reformulating the problem as a system of linear equations allows us to determine an effective stiffness for fixed order parameters [60, 90]. Based on a staggered approach, the governing equations are solved iteratively with an additional static criterion for crack propagation [1]. A more detailed introduction to mechanical jump conditions, in the context of a multiphase-field approach, is given by Schneider et al. [60].

The introduction of order parameters and the interpolation of phase-specific parameters requires additional assumptions. This is extensively discussed in the literature, e.g. by Ammar et al. [58], Durga et al. [56], or Mosler et al. [57], among others. Basic schemes such as a linear or harmonic interpolation of the phase-specific stiffnesses represent the upper and lower bounds of the strain energy in the context of a homogenization theory. Schneider et al. [22] discussed the ability to reproduce sharp interface properties by a multiphase-field model when considering mechanical jumps. Figure 2.4 depicts a schematic representation of such diffuse interface when mechanical jumps are considered. Therefore, each point of the interface can be thought of as a laminar structure. Instead of only the local volume fractions, also the normal vector  $n$  of the interface determines the effective elastic material behavior. In addition, a crack propagation model with multiple crack order parameters is introduced in this work, cf. Chapter 6. For such a model, the ability to obtain an accurate approximation of the phase-specific energy densities for sharp interfaces is of even higher interest.

## 2.4 Linear elastic fracture mechanics

This work is limited to crack propagation in the context of linear elastic fracture mechanics (LEFM), i.e., the material exhibits only elastic behavior. Instead, the inelastic processes that may be associated with crack growth, such as microstructural defects, plasticity, or void formation, are considered within the process zone. This zone, around the crack tip, is assumed to be small compared to the length scale of the body. Note that this zone is not resolved in the context of LEFM and this work. This section contains only the most necessary basics of LEFM, for a more comprehensive discussion the reader is referred to e.g. [91].

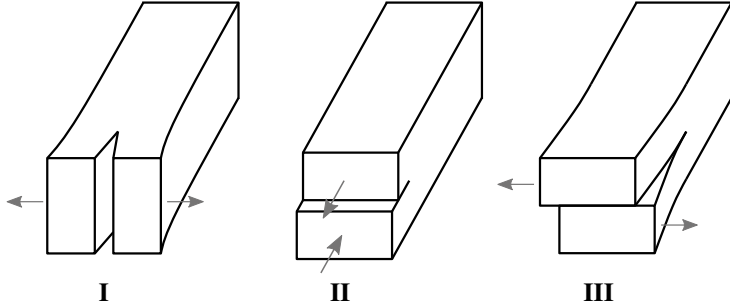


**Figure 2.5:** Different crack modes: Mode I has the crack opening normal to the crack plane. And Mode II and Mode III with the crack opening tangential to the crack plane in different directions.

**Crack opening modes** When considering a crack with a crack tip and a crack surface, three basic crack opening modes can be identified. For mode I, the crack opening is normal to the crack surface and can be associated with a tensile stress normal to the crack plane. For both Mode II and Mode III, the crack opening is tangential to the crack plane. Mode II can be associated with a sliding mode and with shear stress parallel to the crack plane and perpendicular to the crack front. Mode III can be considered as a tearing mode, with shear stress parallel to the crack plane and front. These three modes are also displayed in Figure 2.5. Note that for most real microstructures and loads a mixed mode, a superposition of the three modes, can be expected.

**Stress intensity factors** For pure crack opening modes, the fields near the crack tip, e.g. stresses and strains, can be fully characterized by stress intensity factors  $K_I$ ,  $K_{II}$  or  $K_{III}$  for each corresponding crack mode. These factors depend on the geometry of the body, the crack geometry and the loading and can be determined analytically for some cases, cf. eg. [91]. Based on the  $K$ -concept, which assumes that the crack tip and the process zone can be described by the stress intensity factors, the criterion

$$K_I = K_{Ic}, \quad K_{II} = K_{IIc}, \quad K_{III} = K_{IIIc}, \quad (2.43)$$

for crack growth of the corresponding pure crack mode can be formulated. The fracture toughness values  $K_{Ic} \forall i = I, II, III$  are material-specific properties. In the case of a mixed mode, an equivalent criterion  $f(K_I, K_{II}, K_{III}) = 0$  can be formulated with a generalized function  $f$  [91].

**Energy release rate** Based on the energy potential of a material body  $\Pi$ , including the potential of external forces, the energy release rate  $G$  follows from

$$G = -\frac{d\Pi}{dA}, \quad (2.44)$$

where  $dA$  is an infinitesimal crack surface. With the energy release rate, the criterion

$$G = G_c \quad (2.45)$$

can be formulated for crack growth with crack resistance or critical energy release rate  $G_c$ . A more general approach to this criterion is Griffith's fracture criterion [30]

$$\frac{d\Pi}{dA} + \frac{d\Gamma}{dA} = 0, \quad (2.46)$$

with the fracture energy  $\Gamma$ . From Equation (2.44) it follows that the energy released by crack growth must be equal to the energy required to create the corresponding new crack surface, so that the crack resistance can also be related to the surface energy density  $\gamma$  of a crack flank by  $G_c = 2\gamma$ .

## 2.5 Molecular dynamics

**General idea**<sup>3</sup> Molecular dynamics (MD) is a simulation method that allows prediction of the temporal evolution and interaction of atoms and molecules, mostly using numerical integration of Newton's equations. The MD

---

<sup>3</sup>The content of this section has been taken directly from Schöller et al. [2] with minor linguistic changes.

method has its origins in the work of Alder and Wainwright [92, 93] and Stillinger and Rahman [94]. An overview of the history of MD and its application is given by van Gunsteren and Berendsen [95].

### 2.5.1 Lagrange equations

The structure of the derivation of the equations for MD is based on the Lagrangian formalism, cf. Goldstein [96]. Based on the action functional

$$S = \int \mathcal{L}(\mathbf{x}_1, \dots, \mathbf{x}_N, \mathbf{v}_1, \dots, \mathbf{v}_N) dt \quad (2.47)$$

with the position vector  $\mathbf{x}_i$  for a particle  $i$  and the velocity vector  $\mathbf{v}_i = \dot{\mathbf{x}}_i$  for  $N$  particles in the system considered. The Lagrangian follows by

$$\mathcal{L}(\mathbf{x}_1, \dots, \mathbf{x}_N, \mathbf{v}_1, \dots, \mathbf{v}_N) = K(\mathbf{v}_1, \dots, \mathbf{v}_N) - U(\mathbf{x}_1, \dots, \mathbf{x}_N), \quad (2.48)$$

with the kinetic energy  $K$  and the potential energy function  $U$ . For a stationary point of  $S$ ,

$$\frac{d}{dt} \left( \frac{\partial \mathcal{L}}{\partial \mathbf{v}_i} \right) - \frac{\partial \mathcal{L}}{\partial \mathbf{x}_i} = 0 \quad (2.49)$$

must hold, which are the Euler-Lagrange equations in the context of molecular dynamics. The kinetic energy  $K$  is given by

$$K(\mathbf{v}_1, \dots, \mathbf{v}_N) = \frac{1}{2} \sum_i^N m_i \mathbf{v}_i \cdot \mathbf{v}_i, \quad (2.50)$$

with the mass  $m_i$  of particle  $i$ . The potential energy function  $U$  can be associated with the conservative force vector  $\mathbf{f}_i$  for an particle  $i$  with

$$\mathbf{f}_i(\mathbf{x}_1, \dots, \mathbf{x}_N) = -\frac{\partial}{\partial \mathbf{x}_i} U(\mathbf{x}_1, \dots, \mathbf{x}_N). \quad (2.51)$$

**Algorithm 1:** Velocity Verlet algorithm

---

```
 $t \leftarrow t_0$   
while  $t < t_{\text{end}}$  do  
   $\mathbf{x}_i(t + \Delta t) \leftarrow \mathbf{x}_i(t) + \Delta t \mathbf{v}_i(t) + \frac{1}{2} \Delta t^2 \mathbf{a}_i(t)$   
   $\mathbf{v}_i\left(t + \frac{1}{2} \Delta t\right) \leftarrow \mathbf{v}_i(t) + \frac{1}{2} \Delta t \mathbf{a}_i(t)$   
   $\mathbf{a}_i(t + \Delta t) \leftarrow \frac{\mathbf{f}_i(t + \Delta t)}{m_i}$   
   $\mathbf{v}_i(t + \Delta t) \leftarrow \mathbf{v}_i\left(t + \frac{1}{2} \Delta t\right) + \frac{1}{2} \Delta t \mathbf{a}_i(t + \Delta t)$   
   $t \leftarrow t + \Delta t$   
end
```

---

With (2.50) and (2.51) the Equations (2.49) can be rewritten by

$$m_i \mathbf{a}_i - \mathbf{f}_i = 0, \quad (2.52)$$

with the acceleration vector  $\mathbf{a}_i = \dot{\mathbf{v}}_i = \ddot{\mathbf{x}}_i$ , which resembles Newton's second law of motion and is the basis of the molecular dynamic simulations performed in this work.

## 2.5.2 Microcanonical ensemble

A system with  $N$  particles, e.g. atoms and additionally a fixed volume of the system ( $V$ ) and a fixed internal energy ( $E$ ) is considered as a microcanonical ensemble. This is often referred to as a (constant) NVE ensemble. Applying a time integration method to the equations of motion (2.52) yields a molecular dynamics algorithm.

**Verlet integration** Based on Newton's equations of motion, a Taylor expansion of the position coordinates  $x_i$  can be performed at two different time steps,  $t + \Delta t$  and  $t - \Delta t$ . Combining these expansions yields

$$\mathbf{x}_i(t + \Delta t) = 2\mathbf{x}_i(t) - \mathbf{x}_i(t - \Delta t) + \frac{1}{2}\Delta t^2 \mathbf{a}_i(t) + \mathcal{O}(\Delta t^4), \quad (2.53)$$

with the time step width  $\Delta t$  and an error term of order  $\Delta t^4$ . This integration scheme is also referred to as Verlet integration [97].

**Velocity Verlet integration** The Verlet integration evolves solely the position vector. Although the velocity could be constructed at any time, an alternative integration scheme is given by

$$\mathbf{x}_i(t + \Delta t) = \mathbf{x}_i(t) + \Delta t \mathbf{v}_i(t + \Delta t) + \frac{1}{2}\Delta t^2 \mathbf{a}_i(t + \Delta t) \quad (2.54)$$

$$\mathbf{v}_i(t + \Delta t) = \mathbf{v}_i(t) + \frac{1}{2}\Delta t (\mathbf{a}_i(t) + \mathbf{a}_i(t + \Delta t)), \quad (2.55)$$

which is known as the Velocity Verlet integration [98] and evolves the position as well as the velocity vector. Despite the rather simple scheme, this integrator exhibits some important properties, such as time reversibility, and is therefore used as the time integration scheme for the molecular dynamics simulations of this work. A possible implementation of this scheme is shown in Algorithm 1.

### 2.5.3 Isobaric-isothermal ensemble

As an alternative to the microcanonical ensemble, also the number of particles ( $N$ ), the pressure ( $P$ ) and temperature ( $T$ ) can be fixed, resulting in the isobaric-isothermal or NPT ensemble. One way to archive this ensemble is to use a Nosé-Hoover thermostat. Instead, in this work a NVE ensemble is used with a velocity Verlet integration, along with a thermostat and a barostat. For the latter, a Langevin thermostat [99] and a Berendsen barostat [100] are chosen, which are briefly introduced below.

**Langevin thermostat** The basic idea of the Langevin thermostat [99] is to add a random force  $\mathbf{f}_i^r$  to the particles with

$$\mathbf{f}_i^r \propto \sqrt{\frac{k_B m_i \theta}{\Delta t \gamma}}, \quad (2.56)$$

the Boltzmann constant  $k_B$ , and a damping factor  $\gamma$ . This force mimics the force caused by random collisions of solvent atoms with the particles at a given temperature  $\theta$ . In addition, a friction force

$$\mathbf{f}_i^f = -\frac{m_i}{\gamma} \mathbf{v}_i \quad (2.57)$$

is added to damp the velocity of the particles. With forces of this nature it can be shown that the local temperature evolves towards  $\theta$ .

**Berendsen barostat** The Berendsen barostat [100] couples the system weakly to a heat bath of some pressure  $p_0$ . This adds an additional term

$$\left. \frac{dp}{dt} \right|_{\text{bath}} = \frac{p_0 - p}{\tau_p} \quad (2.58)$$

describing the coupling to the heat bath, with the pressure of the system  $p$  and a time constant  $\tau_p$ . This can be archived by rescaling the simulation domain by the factor

$$\mu = 1 - \frac{\kappa_T \Delta t}{\tau_p} (p_0 - p), \quad (2.59)$$

at each time step with an isothermal compressibility  $\kappa_T$ .

## 2.5.4 Potential energy function

The potential energy function  $U$  of a system with  $N$  particles can be decomposed into

$$U = U^{\text{intra}} + U^{\text{inter}}, \quad (2.60)$$

where  $U^{\text{intra}}$  represents intramolecular interactions and  $U^{\text{inter}}$  represents intermolecular interactions.

**Intramolecular interactions** The intramolecular part of potential energy function  $U^{\text{intra}}$  can be further decomposed with

$$U^{\text{intra}} = \sum_{i>j} U_{ij}^{\text{lj}} + U_{ij}^{\text{C}} \quad (2.61)$$

in a pairwise interaction contribution  $U_{ij}^{\text{lj}}$  and an additional Coulomb potential  $U_{ij}^{\text{C}}$ . Note that the subscripts denotes the particle index, not a tensorial index. The pairwise interaction is modeled by a standard 9/3 Lennard-Jones potential

$$U_{ij}^{\text{lj}} = \epsilon^{\text{lj}} \left( 2 \left( \frac{\sigma}{r_{ij}} \right)^9 - 3 \left( \frac{\sigma}{r_{ij}} \right)^6 \right) \quad r_{ij} < r_c, \quad (2.62)$$

with  $r_{ij}$  as the distance between particle  $i$  and  $j$ . The parameters  $\sigma$ , and  $\epsilon^{\text{lj}}$  describes the position and value of the minimum of the potential. Both can be dependent of the type of particle  $i$  and  $j$ , but for the sake of clarity indices are omitted. The Coulomb potential follows by

$$U_{ij}^{\text{C}} = \frac{Cq_iq_j}{\epsilon^{\text{C}}r_{ij}} \quad r_{ij} < r_c, \quad (2.63)$$

with the charge  $q_i$  of a particle  $i$ , and the dielectric constant  $\epsilon^{\text{C}}$ . The energy-conversion constant  $C$  is dependent of the particle types.  $U_{ij}^{\text{lj}}$  as well as  $U_{ij}^{\text{C}}$  are truncated after a cutoff distance  $r_c$  to reduce the computational cost, with a negligible error.

**Intermolecular interactions** The intermolecular interaction contribution  $U^{\text{inter}}$  of the potential energy function can be further decomposed by

$$U^{\text{inter}} = \sum_{i,j} U_{ij}^{\text{B}} + \sum_{i,j,k} U_{ijk}^{\text{A}} + \sum_{i,j,k,l} U_{ijkl}^{\text{D}} + \sum_{i,j,k,l} U_{ijkl}^{\text{I}}. \quad (2.64)$$

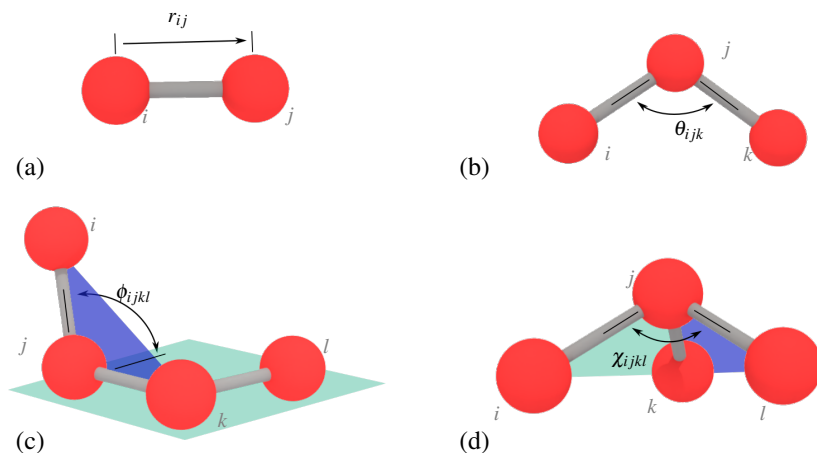


**Figure 2.6:** Different contributions to the intramolecular potential energy: (a) Energy due to bonds stretching between atoms  $i$  and  $j$  at distance  $r_{ij}$ , (b) due to an angle  $\theta_{ijk}$  between three atoms  $i$ ,  $j$  and  $k$ , (c) due to a dihedral angle  $\phi_{ijkl}$  of four atoms  $i$ ,  $j$ ,  $k$  and  $l$ , and (d) due to an improper angle  $\chi_{ijkl}$  of four atoms  $i$ ,  $j$ ,  $k$  and  $l$ .

This involves the energy contribution due to bonds stretching between atoms  $U_{ij}^B$ , due to an angle  $\theta_{ijk}$  between three atoms ( $U_{ijk}^A$ ), due to a dihedral angle  $\phi_{ijkl}$  of four atoms ( $U_{ijkl}^D$ ), and due to an improper angle  $\chi_{ijkl}$  of four atoms ( $U_{ijkl}^I$ ). An illustration of the bond length and the different angles is given in Figure 2.6. Note that the indices  $i, j, k, l$  are chosen from the set of atoms that are actually bonded with the corresponding topology (see Figure 2.6). The individual terms are based on the COMPASS force field [101–103] and are completely listed in Appendix A.1.

### 3 Two-stage polymerization using molecular dynamics<sup>1</sup>

In the context of thermoset polymers, early studies on epoxy systems were conducted by Barton et al. [104, 105], and also material property prediction of thermoset polymers, based on MD simulations, were performed [106–109]. To be able to model the reaction of thermosets, force-fields like REAXFF [110] or RMDff [111] were invented. Despite the ability to model reactive processes, the increase of the computational cost hinders the investigation of bigger systems with more realistic number of molecules. In contrast to this, custom scripts were often developed in order to generate systems in a preprocessing step [112, 113]. Furthermore, empirical modeling of reactive processes in classical molecular dynamics were introduced [76, 114–118]. These approaches compare the pre-reaction topology, and if the reaction occurs, the topology is updated according to a post-reaction template. Recently the REACTER framework [116–118] enabled multiple reactions during a continuously running simulation, based on, e.g. a distance, orientation, user-specified, or a more advanced Arrhenius type criterion. This allows massive, parallel simulation of thermoset polymerization. Schwab and Denniston [76] develop a similar approach to model the polymerization of a UPPH resin system, using an Arrhenius type criterion. They were able to investigate the resin system during the copolymerization process with reasonable computational effort, and determine effective properties.

---

<sup>1</sup>This section is based on the work of Schöller et al. [2]. Minor linguistic changes and additions have been made.

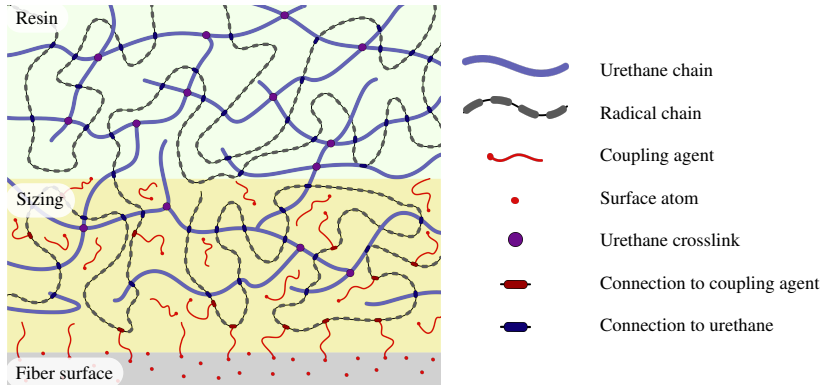


**Figure 3.1:** Schematic interface between glass fiber surface, fiber size and the resin. The legend on the right indicates the individual components.

## 3.1 Constituents

A schematic showing how the constituents are arranged in the system is given in Fig. 3.1. The surface of the glass fiber forms a passive substrate at the bottom for the sizing layer which is then followed by the bulk UPPH resin at the top. These constituents are described in more detail below. The goal is to construct a slightly simplified, but reasonably realistic, chemically bonded structural model of the full system.

### 3.1.1 Glass fiber surface

The material class for fibers used in FRPs can vary widely. One of the most commonly used is silica based glass, which consist in general of a complex chemical structure [119]. In addition, the composition of a glass surface can differ greatly from the bulk of the glass fiber [64, 70]. An E-glass is assumed for this work as it is commonly used in FRPs and is chemically simpler than other choices [120]. The total composition of all components on such a surface

Element	Atomic composition (%)	Atomic weight
Si	22.5	28.086
O	59.5	15.999
Ca	5.5	40.078
Al	6.9	26.982
Mg	1.0	24.304
Na	0.6	22.990
B	4.0	10.806

**Table 3.1:** Components of the glass fiber surface [70, 121].

has been measured by XPS scans performed by Liu et al. [70], and listed in Table 3.1.

The connection between the fiber surface and the sizing agents is primarily established through bonding with silicon atoms. The other surface atoms play an otherwise passive role in this system. Hence, as a further simplification, the fiber surface is represented solely by its silicon atoms. Forming essentially a static substrate for the system, a layer of silicon atoms needs to be generated that provides a reasonable spacing and configuration to account for the whole composition of the fiber surface.

### 3.1.2 Resin system

This section introduces the resin system used in this work. The reader is referred to the work of Schwab and Denniston [76] and Verleg [122] for a more extensive discussion of the UPPH resin. In order to provide the resin with the functionality to perform the copolymerization, it consists of three main components: Isocyanates, unsaturated polyester, and peroxide molecules. For the latter TRIGONOX<sup>®</sup> C is assumed, where only relatively few molecules are present, since it serves only as an initiator for the radical reaction. The isocyanate LUPRANATE<sup>®</sup> M 20 R consists of methylene diphenyl thiocyanate

(MDI) and their polymeric variants (P-MDI), with different functionality. Finally, the unsaturated polyester DARON<sup>®</sup> AQR 1009 consists of molecules of different functionality diluted by styrene. For a complete composition with functionalities and molecular weights the reader is referred to Table 3.2 and Schwab and Denniston [76]. In the following, the two-stage reaction is described as used in a typical sheet molding compound (SMC) process, in which glass fiber-reinforced UPPH is employed [7].

**Polyurethane reaction** On a carrier film, the mixed resin is applied. In addition, chopped glass fibers are added. At room temperature, the hydroxyl groups of the UP begin to react with the isocyanates groups of (P)-MDI, creating crosslinks between these components (cf. Figure 3.1). This polyaddition leads to long polyurethane chains for which the material changes from a fluid to a highly viscous, more rigid state. This B-staged material can be more easily transported, stored and cut for the final curing.

**Radical polymerization** The B-stage material is placed in a press with pre-heated molds. Due to the increase in temperature and pressure during compression, the peroxide group begins to cleave, producing radical oxygen atoms. The free radicals attack the double-bonded carbon of the styrene and polyurethane molecules. By creating a more stable bond with the carbon, the other carbon of the double bond itself becomes a radical. Thus, a polymer chain begins to form and propagates through the material, forming a network of polystyrene that crosslinks the polyurethane chains formed by the first reaction. This results in an interpenetrating polymer network (IPN) of polyurethane and polyester chains, as shown in Figure 3.1, which gives the material its final strength and properties. In the system investigated in this work, the selected coupling agent (cf. Section 3.1.3) of the size also takes part in this reaction. This leads to increased adhesive bonding, as strong covalent bonds ultimately connect all components, including the fiber surface. The chains are terminated by the combination of radicals at the end of two chains. At the macroscopic level, the

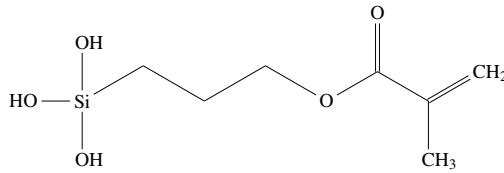


**Figure 3.2:** Skeletal formula of the hydrolyzed  $\gamma$ -MPS.

material begins to cure due to heat and pressure as it flows to form the final component.

### 3.1.3 Fiber sizing

For the selection of glass fiber sizing there exists a large number of possible components and compositions. Thomason [62] describes sizing as a black-box technology, since size formulations are kept secret by suppliers and the understanding of glass fiber sizing in the literature is quite limited, fragmented, and usually only discussed generically. Because the size must perform a variety of tasks, a size used in the industry may consist of ten or more components. Thus, components such as a coupling agent, film former, lubricant, emulsifier, and other processing aids, among others could be used [123]. However, most of them are present only in relatively low concentrations [65].

The main components are therefore the film former and the coupling agent. The coupling agent improves the adhesion of fiber and polymer matrix. Therefore, it must react with the fiber surface as well as providing a functional group that reacts with the resin. The film former is usually a polymer that is mainly intended to protect the fibers during processing in the FRP production process [124]. The film former is usually chosen to be compatible with, if not identical to, the matrix material used.

In this work, the complex sizing system is simplified using the following assumptions:

- The sizing components are reduced to film former and coupling agent.
- Partly due to lack of information to the contrary, and the variety of other formulations possible, it is assumed that the film former is the same polymer as the matrix resin, hence UPPH, cf. Section 3.1.2.
- Only a common coupling agent compatible with the resin is chosen, making our sizing somewhat generic. Most actual sizing would consist of a blend of different coupling agents, but these vary amongst different manufacturers and their identity and concentration are typically proprietary. Thus, it would be difficult to include these components in a model which would fit any particular system more realistically.

### 3.1.3.1 Coupling agent

Most coupling agent for glass fibers are organofunctional silanes, and their general structure consists of  $R^1-Si(OR^2)_3$ , where  $R^1$  provides the ability to react with the matrix material, creating mainly strong bonded links between matrix and the coupling agent, cf. Figure 3.1.  $R^2$  is usually a methyl or ethyl group [62], and their hydrolyzed version is able to bind to the fiber surface. Together with the bond to the matrix, this improves the overall adhesion of the polymer matrix and glass fiber.

Thomason [62] extensively studied coupling agents being used based on literature and patents. From the manifold number of different available silane molecules, he concludes that the industry appears to have focused mainly on a few silanes where  $R^1$  contains either an amino, epoxy, methacryloxy or vinyl functional group. The most common silane is  $\gamma$ -aminopropyltriethoxysilane, which is normally used for thermoplastics and sometimes also for polyester and epoxy polymers. In contrast, the primary coupling agent for polyester appears to be  $\gamma$ -methacryloxypropyltrimethoxysilane ( $\gamma$ -MPS). Furthermore,  $\gamma$ -glycidoxypropyltrimethoxysilane is used for epoxy and multicompatible

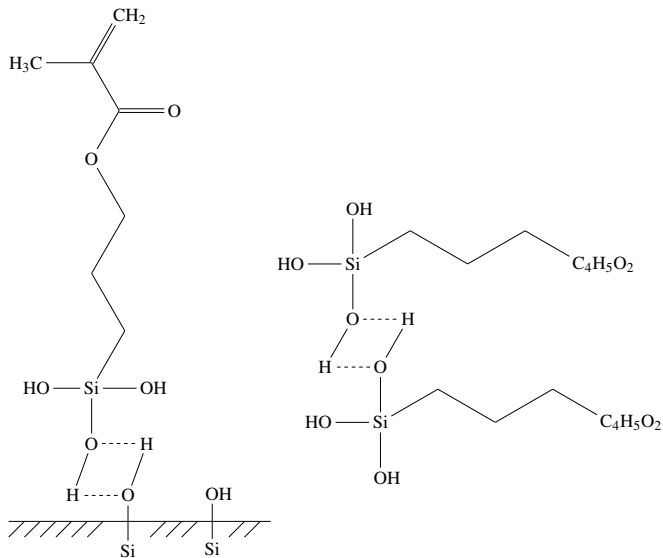


**Figure 3.3:** Hydrogen bonds of the coupling agent  $\gamma$ -MPS at the glass fiber surface (left) and with other coupling agent molecules (right).

polymers [62]. As in this work a UPPH resin is considered (cf. Section 3.1.2), the unsaturated polyester compatible coupling agent  $\gamma$ -MPS is chosen.

### 3.1.3.2 Application of the size

In order to apply the size to the glass fibers, it needs to be dissolved, usually using water as the solvent. In this process,  $\gamma$ -MPS of the size is hydrolyzed to dissolve the methyl groups and yield methanol and  $R^1-Si(OH)_3$ , with the complete formula shown in Figure 3.2. The aqueous size is then applied to the hot glass fiber by rollers, shortly after the liquid glass has been extruded through bushings to form the glass fiber [123]. The applied size then dries on the glass fibers, and the hydrolyzed  $\gamma$ -MPS undergoes a condensation process. In this process, the hydroxyl groups form hydrogen bonds with other hydroxyl

groups. Potential reaction partners are Si–OH groups on the silicate surface of the fibers, but also other coupling molecules. In a subsequent step, a covalent bond forms while they lose a water molecule. Figure 3.3 shows the bonding of the  $\gamma$ -MPS to the fiber surface and other coupling agents. Ultimately, a small amount of the coupling agent becomes strongly bonded to the surface, while others form oligomers.

## 3.2 Molecular modelling description

The models and subsequent simulations described in this section are all implemented in the open-source molecular dynamics software LAMMPS [125, 126]. The COMPASS force field [101–103] is used to model the molecules and their interaction. In general, the potential of the force field consists of various contributions that can be grouped into two categories: The inter-molecular interaction is taken into account via individual potentials for bonds, angles, dihedrals, and impropers. On the other hand, a 9-6 Lennard-Jones potential models the van der Waals forces, and together with a Coulombic potential represent the intra-molecular interactions. For a more detailed discussion of the potentials, the reader is referred to Sun [103].

### 3.2.1 Fiber surface

During the main simulations, the atoms on the fiber surface will be rigid. However, to generate the surface and provide the system with the basic layer of silicon atoms, the use of complex potentials, including force fields, is omitted. Instead, a standard 12/6 Lennard-Jones potential

$$E = 4\epsilon \left[ \left( \frac{\sigma}{r} \right)^{12} - \left( \frac{\sigma}{r} \right)^6 \right], \quad r < r_c, \quad (3.1)$$

for the Si atoms is introduced, with  $\epsilon = 1 \text{ kcal mol}^{-1}$ , and  $\sigma = \sqrt[6]{2.0}r_0$ . Based on Si–O–Si bond lengths, the equilibrium spacing for the potential is set to  $r_0 = 3.28 \text{ \AA}$ , and a cutoff length  $r_c = 10 \text{ \AA}$ . Since the main objective of this work is to show the interaction between sizing and resin, the influence of the simplification of the E-glass fiber surface is assumed to be negligible.

Domain	Component	No of mol.	
Resin	(P-)MDI	functionality = 2	630
		functionality = 3	72
		functionality = 4	324
	UP	1 × basic structure	486
		5 × basic structure	36
		10 × basic structure	198
	Styrene		4716
Peroxide		72	
Size	$\gamma$ -MPS	hydrolyzed	2211
	(P-)MDI	functionality = 2	444
		functionality = 3	51
		functionality = 4	228
	UP	1 × basic structure	343
		5 × basic structure	25
		10 × basic structure	140
Styrene		3324	
Peroxide		51	
Surface	$\gamma$ -MPS	attached & hydrolyzed	384
	Si		4890

**Table 3.2:** Composition of the different layer of the domain. Note that the number of size molecules are not the final ones, as the size layer is processing during the generation.

### 3.2.2 Reaction algorithms

Three different reaction processes are examined in this work: First, a condensation reaction in which the hydrolyzed coupling agent forms oligomers. Second, the polyurethane addition of the resin results in the B-stage material. Further, the final curing occurs by a radical polymerization, which crosslinks the components, including the coupling agent, and thus the fiber surface. Because different reaction algorithms are used for the condensation and polymerization reactions, they are introduced separately in the following.

**Condensation** To generate the condensation reaction, the REACTOR framework [116, 117] is used. Based on pre- and post-reaction templates, this framework offers great flexibility in modeling reactions. Although it is possible to incorporate various conditions, such as an Arrhenius type condition, only a simple distance criterion is used for the condensation: If the initiator atoms are within a certain distance, a drawn random number is compared with a given probability. If the reaction takes place, the topology is updated according to the specified reaction templates. Since the main goal of this reaction is to model the formation of coupling agent oligomers from monomers, this approach is considered sufficient. In addition, REACTOR allows the removal of atoms from the system during the reaction. This allows easy treatment of the water, which is a product of condensation that would otherwise have to be removed by other cumbersome techniques (such as via a diffusion-driven drying process).

**Polymerization** Following Schwab and Denniston [76] a more involved approach is used for both polymerization reactions. Similar to the REACTOR framework, potential reaction sites and post-reaction topology are defined based upon templates. Instead of only a simple distance criterion, an Arrhenius type equation

$$F = \exp\left(-\frac{\Delta E}{k_B \Theta}\right), \quad (3.2)$$

with an activation energy  $\Delta E$ , the Boltzmann constant  $k_B$  and the temperature  $\Theta$ , is considered. The activation energy  $\Delta E$  describes the difference between the energy of the bond and the energy at which a bond dissociates, or alternatively a bond is formed. For bond dissociation, the  $F$  must be less than a number drawn at random between 0 and 1. Conversely,  $F$  must be greater than the random number to form a bond. In addition to this basic algorithm, Schwab and Denniston adapted the approach to model the polymerization of UPPH in a more appropriate way: In the polyurethane reaction, a hydrogen atom is transferred from a hydroxyl group to a nitrogen atom. To avoid instabilities, they added a transient bond that excluded these atoms from all potentials except the Coulomb potential, when the main bond between carbon and oxygen atoms is formed. This leads to a smooth transition of the hydrogen atom towards the nitrogen atom until the bond changes into a standard one with the full potential. Furthermore, Schwab and Denniston introduced additional Coulomb forces to the initiator atoms. The existence of an interaction between these atoms is physically motivated by these sites being electrophile or nucleophile centers. However, the form of the interaction (Coulomb) is artificial. These artificial charges accelerate the polymerization and allow it to be simulated on the timescales that a classical MD simulation can handle, and is therefore also used in this work. The charges are chosen small enough so that properties of the resulting bonded network does not appear to be altered by the accelerated dynamics [76].

### 3.3 Results

As in the actual system, the manufacturing of the fiber, application of sizing, and embedding in the resin are all done in separate processes. In the following sections, the generation of the fiber–resin system is described in successive steps. The setup and conditions of each step are separately introduced, and their results are discussed:

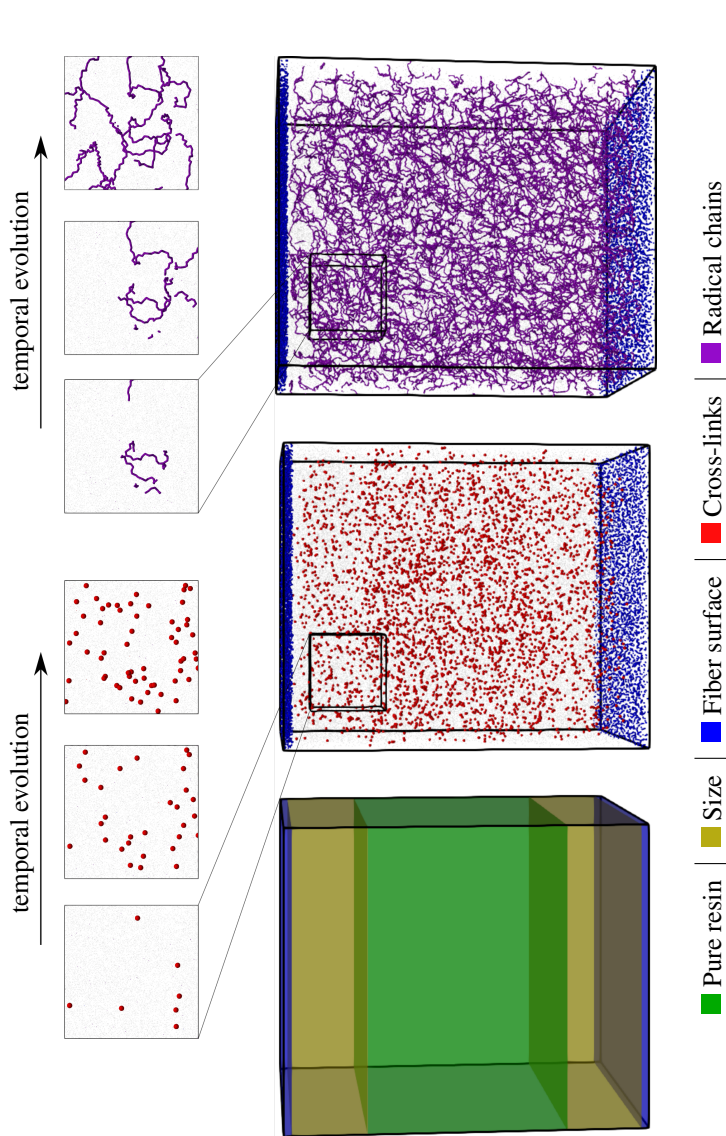


**Figure 3.4:** The partition of the domain in the individual layers in the left, the system after the polyurethane reaction (50% conversion rate) in the center, and after the radical reaction in the right. The individual components are highlighted in the corresponding color. In the top, sections of the domains are shown at successive time points in the reactions.

System	Step	Time step (fs)	No. of steps
Resin	Compression	1.0	200000
	Equilibrating		200000
Sizing	Compression	1.0	100000
	Equilibrating		200000
	Condensation		1000000
Combining	Compression	1.0	100000
	Equilibrating		200000
Polyurethane reaction		$2-5 \times 10^{-2}$	$\approx 5700000$
Radical polymerization		$5 \times 10^{-2}$	$\approx 5140000$

**Table 3.3:** Number of steps and time steps for each simulation step and the different systems. For the polyurethane reaction, the time step is increased linearly up to a conversion level of 50%.

- Two rigid glass fiber surfaces, consisting of silicon atoms, representing the complex structure of a real E-glass fiber, are generated.
- The sizing layer, consisting of UPPH resin and coupling agent, is placed between these surfaces with some pre-attached  $\gamma$ -MPS and the condensation reaction is conducted.
- Separately, a pure UPPH resin layer is generated and compressed to an initial configuration.
- The surface-sizing layer and the resin layer are combined: The two surfaces bound the domain normal to these surfaces, followed by two sizing layers and a pure resin layer in the middle of the domain. Such a system is also schematically shown in the left of Figure 3.4.
- The two-stage curing process, the polyurethane and radical polymerization, takes place subsequently.

The PACKMOL [127] software is used for packing of the initial molecules. In combination with MOLTEMPLATE [128], this allows a flexible setup of complex MD simulations in LAMMPS [125, 126] using force fields. A velocity-Verlet integration scheme is used to solve the Newtonian equations of motion [97]. Temperature is adjusted by a Langevin thermostat [99] and the pressure is also set, as described in the next subsection. The result is that the simulations are performed in a NPT ensemble: Constant number of atoms, constant pressure, and constant temperature, although the set pressure and temperature may be different during the different steps described below, just as they would be in the actual manufacturing of a real composite system. Furthermore, simulation parameters, such as the time step and the number of time steps, for each simulation step are summarized in Table 3.3. In the equilibration steps, the pressure, temperature, and domain length normal to the fiber surface of the corresponding systems were observed to determine a sufficient equilibration time.

### 3.3.1 Fiber surface

To create the fiber surface, a random initial distribution of Si atoms is placed in a large periodic domain, and then compressed to E-glass density. This is performed at 293.15 K with interactions based on the Lennard-Jones potential (3.1). For this purpose, the final density is assumed to be  $2.58 \text{ g cm}^{-3}$ , cf. Wallenberger and Bingham [120]. In addition, the silicon represents not only the mass but the entire composition of the E-glass fibers surface, see Table 3.1. From the final equilibrated system, two layers are extracted with a thickness of  $6.56 \text{ \AA}$ , which is about twice the equilibrium bond length of a Si–O–Si bond. Thus, each layer consists of at least two Si atoms in the normal direction. The final edge length of the (square) fiber surface is  $200 \text{ \AA}$  and also determines the domain sizing of the subsequent steps. In these, the silicon atoms are assumed to form a rigid layer based on the configuration created in this step. Therefore, the force on these atoms is averaged for the entire layer and an additional force representing the ambient pressure is applied. As a consequence, the pressure

can be controlled while enabling the layer to move while maintaining the initial configuration of the surface atoms.

### 3.3.2 Sizing layer

The implementation of the reaction algorithms (cf. Section 3.2) would allow depicting the complete condensation reaction of the coupling agent, including bonding to the fiber surface as well as to other coupling agent molecules, cf. Figure 3.3. However, in combination with the fully atomistic approach, realistic surface coverage is not possible due to the lack of a feasible timescale. Instead, some silicon atoms of the inner surface layers have pre-attached coupling molecules before the actual condensation reaction takes place. This simplified approach seems legitimate, especially since the first chemically absorbed layer of the sizing appears to be fairly well understood [70, 129–131] and reasonable assumptions can be made about the spatial distribution of  $\gamma$ -MPS. Based on the area occupied by a coupling agent molecule on the fiber surface, reported by Miller and Ishida [129] to be  $0.59 \text{ nm}^2$ , a method for placing these pre-attached molecules was developed: The occupied area is converted into a mean separation distance of the  $\gamma$ -MPS molecules. Assuming a uniform distribution and a circular area  $\pi r^2$ , this results in a minimum distance given by the radius  $r$ . For the first pre-attached molecule, a random atom is selected from the generated surface layer. Thereby, only the silicon atoms in the inner half of the layer are considered. Next, the Si atom with the least distance to all other pre-attached molecules is searched, keeping the minimum distance of  $\sqrt{0.59/\pi} \text{ nm}$ . This atom is converted from a simple silicon atom into one with a pre-attached variant. This search for atoms with minimal but valid distance is repeated until no further pre-attached molecule can be placed. This procedure results in a certain amount of already chemically absorbed  $\gamma$ -MPS on the fiber surface, cf. Figure 3.1.

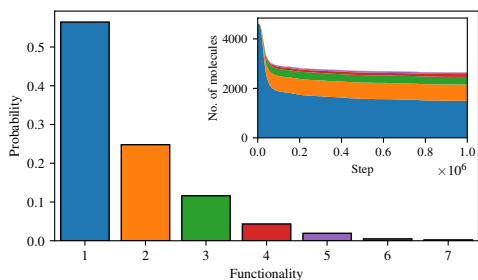


**Figure 3.5:** Distribution of the number of functional groups of the coupling agent after the simulation of the condensation reaction and the temporal evolution in the inset.

In contrast, the main sizing layer consists of free hydrolyzed coupling agent monomers and UPPH resin acting as a film former, as they are considered to be only physically absorbed initially. The exact composition of the sizing can vary greatly in industrial applications. In this work, 30wt% hydrolyzed  $\gamma$ -MPS and 70wt% film former are assumed, which is within the range reported in the literature [62, 123, 132]. The sizing molecules are placed between the fiber surface layers with the previously attached coupling agent molecules. The composition of the film former corresponds to the pure resin layer, and the detailed number of individual molecules of the sizing as well as the surface layer are listed in Table 3.2. Since the process attempts to mimic real-world processing of FRP, the condensation reaction takes place without the pure resin system, as the sizing is applied and dried during the manufacture of the glass fiber. In addition, if it is assumed that the resin is not involved in the condensation reaction, the computational effort can also be reduced. Finally, these molecules, the hydrolyzed  $\gamma$ -MPS and the film former, with the exception of the pre-attached  $\gamma$ -MPS, are again randomly positioned in a large domain and subsequently compressed to an approximate density of  $1 \text{ g cm}^{-3}$ . This is followed by equilibration at 373.15 K with an ambient pressure of 1 atm applied via the fiber surfaces.

### 3.3.3 Condensation reaction

In the condensation reaction, the hydrolyzed  $\gamma$ -MPS monomers undergo a process to form oligomers. These oligomers can emerge from the physically absorbed coupling agent molecules of the sizing layer. In addition, the chemically absorbed sizing on the fiber surface, consisting of the pre-attached coupling agent molecules, also participates in the condensation process: Hydrogen bonds between the hydroxyl group and the silicon atoms form covalent bonds while water is being given off, see right in Figure 3.3.

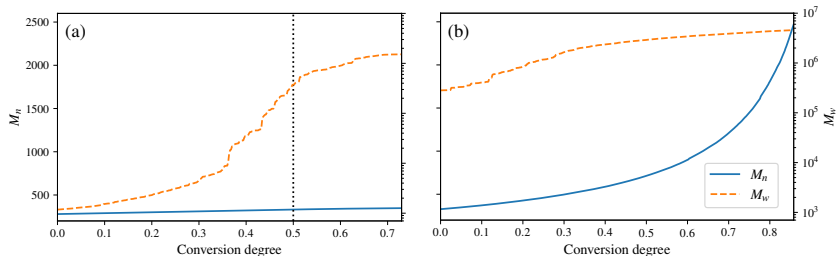
The reaction is conducted starting with the configuration of the previous step, at 373.15 K and 1 atm, to take into account the conditions of the glass fiber manufacturing. Furthermore, the domain is assumed to be periodic tangentially to the fiber surface. Normal to the surface, the rigid silicon atoms limit the domain. In addition, the initial reaction probability is artificially reduced and steadily increased during the course of the condensation process. This is done to ensure a numerically stable simulation, otherwise the very high reaction speed at the beginning would lead to instabilities.

Figure 3.5 shows the final distribution of the number of functional groups in the condensed sizing. Although dimers and trimers are present, the amount of longer oligomers is relatively low, and most of the coupling agent is still present as a monomer. The inset in Figure 3.5 illustrates the development of these groups over time. At the beginning of the simulation, despite the lower probability, the reaction exhibits a high condensation rate, thereafter the rate decreases until the end of the simulation. Although it was observed that the number of oligomers increases with time and their functionality also increases, the distribution of the coupling agent does not completely converge to a steady state (i.e. the lines in the inset of Fig. 3.5 are not perfectly flat at long times). Several reasons seem plausible for the high proportion of monomers in the final distribution: This can be attributed to the basic reaction algorithm, e.g. the water is removed instantly, whereas technically the water has to diffuse through the system to a free surface. As the condensation is a reversible process, these water

molecules could undergo multiple reactions, influencing the final distribution of  $\gamma$ -MPS. Moreover, the full atomic approach used in this work does not allow for the very long timescale for such a condensation reaction in real life. A possible solution could be to omit the condensation reaction and instead work with oligomers from the beginning. However, since detailed information on the distribution of coupling agent oligomers, especially in realistic sizes, is not available in the literature, this approach would raise further issues. In contrast, a study of the condensation stage, e.g., based on a coarse-grained approach such as a united-atom model, could potentially go to longer time scales and provide detailed information about such a distribution. However, such a model would still need to be parameterised based on the fully atomistic model used here. Although such a study is highly desirable, it would be a non-trivial undertaking and is beyond the scope of this work. Moreover, it is expected that other assumptions in the introduction of the model lead to a higher uncertainty in the results. Therefore, the limitations of the presented approach for the condensation reaction are acknowledged, but the possibility to study the interaction between surface sizing and resin is nevertheless greatly extended.

### 3.3.4 Pure resin layer

In order to include a pure UPPH resin layer, a (separate) realistic block of resin must be created first. Therefore, the UPPH resin molecules, which are multiples of the system introduced by Schwab and Denniston [76], see Table 3.2, are randomly placed. As in the previous steps, the system is then compressed to an approximate density of  $1.109 \text{ g cm}^{-3}$ , cf. [76], and subsequently equilibrated at 293.15 K. During this process, the approach of Berendsen et al. [100] is used to control the ambient pressure of 1 atm, which could be used as the domain is assumed to be periodic in all directions.



**Figure 3.6:** Evolution of the number average molar mass  $M_n$  and mass average molar mass  $M_w$  for the polyurethane reaction (a) and radical polymerization (b), over the conversion degree.

### 3.3.5 Complete system

In a final step, the complete system is assembled with all three layers: First, the surface sizing system is partitioned to form the outer layers. The final sizing layer is chosen to be about  $50.0 \text{ \AA}$  thick. Thus, all molecules for which the distance of their center of geometry to the fiber surfaces is below this value are extracted and form the final sizing layers. Therefore, the components of the sizing layer differ from the initial surface-sizing system described in Table 3.2, while approximately maintaining the relative composition. Moreover, the molecules of the resin layer are unwrapped in the normal direction, since the assumption of periodicity is no longer valid. Subsequently, the resin layer is placed between the both surface-sizing layers with a slight initial distance. This system is again compressed to an approximate density of  $1 \text{ g cm}^{-3}$ , followed by equilibration at ambient pressure of 1 atm and 293.15 K.

The system consists of two rigid layers of silicon atoms, followed by the sizing layers, with a  $\approx 130 \text{ \AA}$  thick layer of resin in the center. The resulting total domain has a base area of  $200 \times 200 \text{ \AA}$  and a  $\approx 243 \text{ \AA}$  large extent in the fiber normal direction. Based on this system, cf. left of Figure 3.4, the two stage polymerization reaction is carried out.

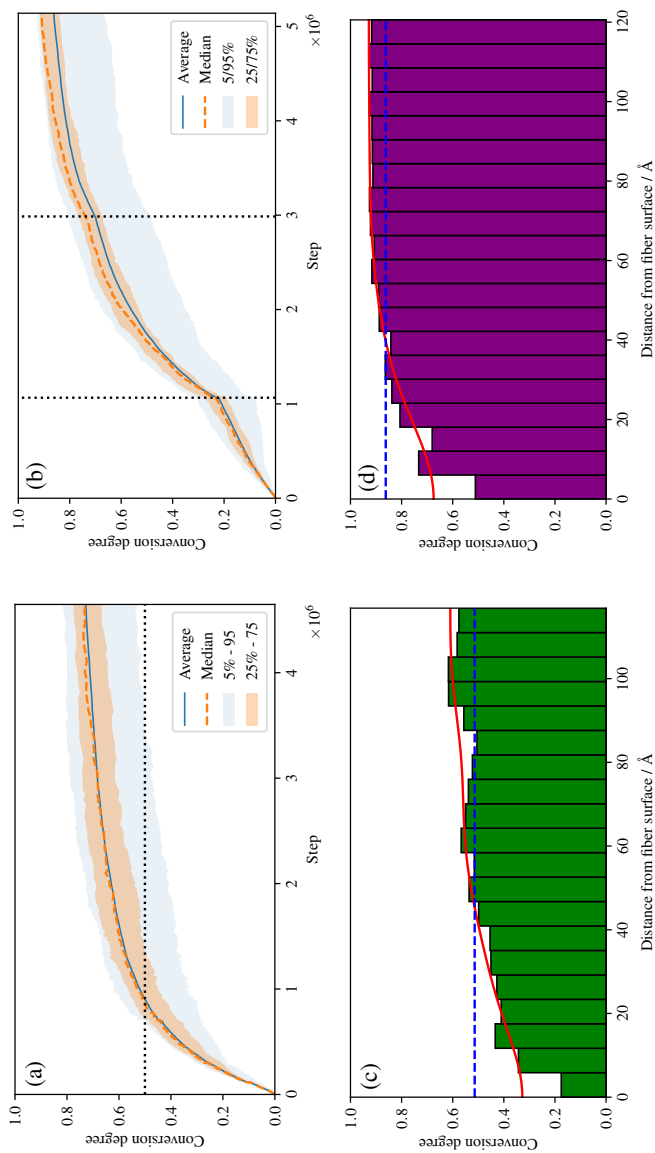


**Figure 3.7:** Temporal evolution of the conversion degree of the polyurethane reaction (a), and the radical polymerization (b) over the simulations. The median, average, as well as percentiles of the underlying spatial binning are displayed. And the spatial distribution of the conversion degree of the polyurethane (c) and radical polymerization (d) at the end of the simulation. In addition to the histograms, the average and a smooth representation of the data (KDE) are displayed.

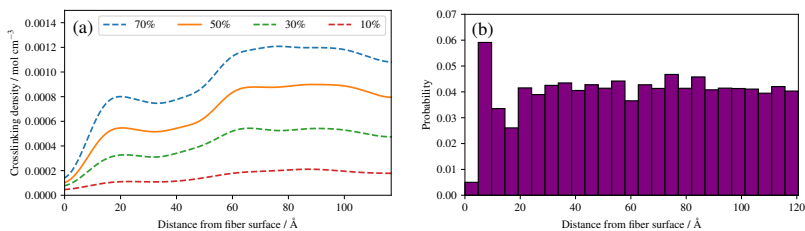


**Figure 3.8:** (a) Spatial distribution of the crosslinking density of the polyurethane reaction at different conversion degrees based on a smooth representation of the data (KDE). (b) Spatial distribution of the relative frequency of radical chains at the end of the radical polymerization.

### 3.3.6 Polyurethane reaction

During the reaction, the unsaturated polyurethane reacts with the isocyanate groups of the (P)-MDI, resulting in a polyaddition reaction that finally yields long polyurethane molecules. This reaction is carried out at 353.15 K and ambient pressure [7]. In order to speed up the simulation,  $\pm 1.5$  charges are added to the initiator atoms of the reaction. As discussed by Schwab and Denniston [76], without auxiliary charges, the polymerization reaction would be too slow for the time scale used in MD simulations. Furthermore, they demonstrated the negligible influence of the charges on the results.

In the center of Figure 3.4, the whole system is shown at 50% conversion. In addition, the cross-links of the isocyanates and the unsaturated polyester are highlighted, and cutouts illustrate the development over time, i.e. the increase in cross-link density. Furthermore, the reader is referred to the ESI of [2] for a complete animation of the reaction. The evolution of the molar masses weighted by the number  $M_n$  and the molar mass  $M_w$  versus the conversion degree is shown in Figure 3.6a. The detailed temporal evolution of the conversion degree over the simulation is plotted in Figure 3.7a and, in addition to the average value, the median and some quantiles are also displayed. The initial fast reaction rate seems to converge quite quickly. Also, despite the average and mean values being nearly the same, it could be observed that the lowest 5% of

the bins had much lower conversion degrees than the average. The domain is then binned based on the distance to the fiber surface to produce Figure 3.7c which shows the spatial distribution of the binning of the conversion degree over the distance to the glass fiber surface. In addition, the average value and a Kernel Density Estimator (KDE) are displayed. The KDE is an estimate for the underlying probability density function of a random variable, and therefore provides a smooth function estimate of the distribution. The figure exhibits the highest conversion degree in the resin layer, far away from the surface. And it decreases steadily towards the glass fiber surface. Since the conversion degree refers to the relative number of reactions that took place in each bin, it is not possible to discuss the spatial distribution of the total number of reactions that occurred based on such a quantity. Therefore, Figure 3.8a shows the spatial distribution of cross-link density, i.e. a smooth representation of the number of cross-links per volume in each bin during the reaction.

In the technical SMC process, the B-stage material represents only a semi-finished product, which can also be assumed to be not fully cured. In this work, a conversion degree of 50 % of the PU reaction is assumed as the starting point for the radical reaction. Especially since the definition of the conversion degree can vary: In this work, the number of actual reactions relative to the theoretical number of possible reactions is used. In contrast, an experimentally determined degree of conversion may differ, since the total number of possible reactions is generally unknown. In Figure 3.6a a drastic increase of  $M_w$  at around 30–40 % conversion can be observed. This jump over orders of magnitude indicates the phase-like transition from liquid resin to rubbery B-stage material. As the maturing of B-stage is optional [7], the assumed conversion degree of 50 % as a basis for radical polymerization is in the range of higher  $M_w$  and is considered a reasonable choice. A variation of this choice in combination with the investigation of the influence on final properties is high desirable, but beyond the scope of this work.

Regarding the crosslinking density, cf. Figure 3.8a, clearly different regimes can be identified for the sizing and resin layers during polymerization. This

is most likely due to the fact that the coupling agent in the sizing layer dilutes the UPPH resin of the sizing and thus, the final density of (P-)MDI is reduced. Moreover, near the fiber, the amount of  $\gamma$ -MPS is high due to the pre-attached coupling agent, therefore the conversion degree is the lowest, which leads also to the low conversion degree in the 5 % quantile in Figure 3.7a.

The spatial distribution of the benzene on the (P-)MDI and the unsaturated polyester during the polyurethane reaction is shown in the appendix A.2. While the distribution of the unsaturated polyester is quite smooth, the distribution of (P-)MDI is uneven. This behavior is less pronounced in the resulting crosslink density. Finally, an almost smooth transition from the resin layer to the surface and to the fiber of the conversion degree can be observed in Figure 3.7c. Since the (P-)MDI consist of the largest molecules in the system, the uneven distribution most likely results from the generation of the system in combination with the limited system size. A reason why a smooth conversion degree nevertheless occurs is not evident to the authors, but could be the subject of subsequent work. However, an experimental investigation of this very thin boundary layer would be very desirable as it would allow a comparison.

### 3.3.7 Radical polymerization

The B-staged material of the previous step is further processed in the radical polymerization: Under high temperature and pressure, the fiber-reinforced UPPH resin flows in the molds and cures completely. Therefore, a temperature of 418 K, and a pressure of 50bar in addition to the ambient pressure is assumed to account for the conditions in the SMC process [7]. Moreover, the reaction is conducted starting with the 50 % conversion configuration of the PU reaction.

In the right of Figure 3.4, the final system after the reaction is shown. The resulting radical chains are highlighted, and the cutouts show the evolution of these chains over time. As before, for a complete animation of the reaction, the reader is referred to appendix A.2. In addition, the evolution of the molecular

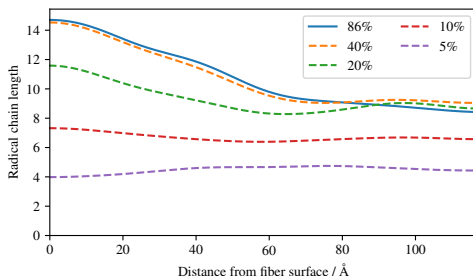


**Figure 3.9:** Spatial distribution of the radical chains length between PU crosslinks at different conversion degrees based on a smooth representation of the data (KDE) during the radical polymerization.

weights are shown in Figure 3.6b. For the molecular weight  $M_w$  there is no sharp increase during the reaction, since there is no phase transition, compared to the PU reaction. Rather a smooth transition from rubbery to solid during the flow in the mold can be observed. In contrast,  $M_n$  exhibits a strongly nonlinear increase when styrene monomers, initially high in number but low in molecular weight, forms chains during polymerization.

For the visualization of the temporal evolution of the conversion degree over the simulation in Figure 3.7b, the same approach as before is used. In addition, the vertical dotted lines mark an increase in the additional charges to accelerate the reaction and avoid excessive computational effort. For the start, charges of  $\pm 1.0$  were chosen, which are increased by  $\pm 0.25$  for each increment. Since the value of these charges has no direct physical effect other than hastening the reaction, no influence of the increase is expected if they are chosen within an acceptable range, cf. [76], which is not exceeded in this work. Furthermore, the spatial distribution of the conversion degree is shown in Figure 3.7d along with the average and a KDE, with the latter providing a smooth interpolation. Moreover, Figure 3.8b displays the relative frequency of radical chains in relation to the distance to the fiber surface. Finally, the length of the radical chains and the spatial dependency, is plotted in Figure 3.9 during the polymerization. The length of a chain is measured by the number of carbon atoms between

crosslinks of the radical chains with the PU. In the resin layer, the average length of the radical chains is about the same. In contrast, these chains are longer in the sizing, as the reduced amount of PU in this layer provides less possibilities for crosslinking. Moreover, at low conversion degrees, the chain length is almost uniform and only becomes longer towards the surface at the end of the reaction. In contrast, the resin layer reaches its final chain length rather early in the simulation. The  $\gamma$ -MPS, which may be part of the radical chain, allows these larger gaps between the PU to be bridged, but is less mobile compared to the small styrene molecules. Therefore, building these longer chains between the less present PU requires more time.

It can be observed that some parts of the system have a much lower conversion degree, which distorts the displayed quantiles and also causes the difference between the average and median, in Figure 3.7b. This also indicates that even with a longer simulation time, a complete conversion seem not feasible. Schwab and Denniston [76] were able to archive a higher final conversion degree and could avoid the need to raise the additional charges repeatedly. However, in this work, the fiber surfaces restrict the movement of the molecules. This reduced diffusivity in the normal direction to the surface results in lower overall reactivity and thus lower conversion. Also, the typical styrene odor of the final component indicates that complete conversion is not achieved in industrial applications. In addition, as before in the UP reaction, the definition of the conversion degree may differ: The conversion degree used in this work, based on the theoretical possible reactions, may overestimate an experimental determined degree of conversion. From this reduced mobility, the result is that the lowest conversion is near to the surface, and is highest in the resin layer (see Figure 3.7d).

In Figure 3.10, the benzene of styrene is plotted during the radical polymerization. The benzenes are distinguished into monomeric (left) and reacted variants (right). While the unreacted benzene increases abruptly at the surface and at the interface between the size and the resin layer, the reacted styrene shows a more even distribution, increasing from the surface to the pure resin layer. Figures

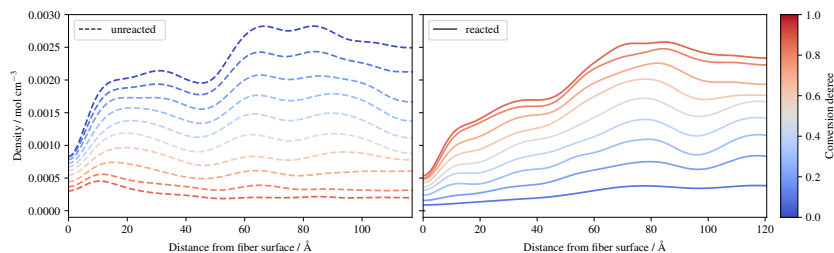


**Figure 3.10:** Spatial distribution of the benzene of styrene during radical polymerization. A distinction is made between monomeric, not yet reacted styrene (left) and reacted styrene in radical chains (right).

for the distribution of all styrene benzenes, as well as for the benzenes of other constituents and the silicon of the  $\gamma$ -MPS, can be found in appendix A.2. Together with the conversion degree (Figure 3.7d) and the frequency of the radical chains (Figure 3.8b), they indicate that molecules, especially small molecules such as styrene, are able to compensate for the different composition of the sizing and resin layers. So the conversion degree does not suddenly drop at the interface, rather the highly agile styrene appears to partially diffuse into the various layers, resulting in a smooth distribution of conversion.

In the distribution of the radical chains, cf. Figure 3.8b, two things can be noted: Firstly, directly at the fiber surface there are almost no chains, but a high peak of chains near to the fiber can be observed. Secondly, there is an almost uniform distribution of the radical chains in the rest of the domain. The latter indicates that the presented system is able to generate a highly linked system via radical chains. This occurs despite the presence of coupling agent in the physically absorbed layer of the sizing, as the  $\gamma$ -MPS can take part in the radical polymerization. While the peak close to the surface results from a layering effect of the pre-attached  $\gamma$ -MPS: The functionality to react with the radicals have all approximately the same distance to the fiber surface. A more detailed spatial distribution of silicon atoms of the  $\gamma$ -MPS during the polymerization reactions is provided in appendix A.2. In addition, the quality of the crosslinking may vary locally and is moreover quite anisotropic near to

the fiber surface. To illustrate these behaviors, a second animation of the radical reaction is provided in appendix A.2. In this, two detail views of sections at the surface are plotted: One for which radicals create a strong connected layer at the surface, with some connection normal to the surface. In the other, no radicals diffuse near to this chemical absorbed  $\gamma$ -MPS layer, resulting in only a few radical chains and therefore an only loosely cross-linked surface.

### 3.4 Interim conclusion

Based on molecular dynamics simulations, a UPPH resin system was extended by adding a fiber surface and sizing layer. From a number of possible coupling agents for the sizing,  $\gamma$ -MPS was selected and a rigid silicon layer was created to mimic the glass fiber surface. Furthermore, the coupling agents were placed as monomers in the domain and a condensation reaction was modeled yielding dimers and higher oligomers in the sizing layer prior to the final two-stage polymerization. In an additional preliminary step, the three generated layers – resin, sizing, and fiber surface – were placed in the final system and equilibrated. Based on the work of Schwab and Denniston [76], the two-stage polymerization of the UPPH resin was conducted on this system. Subsequent evaluations of the quantities during the reactions were carried out. In addition, the system was also evaluated along the normal of the fiber surface, allowing a spatial analysis of the fiber-size-resin system. Due to a lack of information in the literature, a direct comparison of the results was not practicable. Nevertheless, the method provides an alternative approach to the characterization of the resin-glass interface. For further work, collaboration with experimental investigations would be highly desirable. Especially since the results show an almost smooth transition of the degree of conversion between the different layers. This seems counterintuitive, since the different layers differ greatly in their composition. Moreover, anisotropic radical polymerization could be observed near the fiber surface, emphasizing the importance of the choice of constituents of the sizing, especially the coupling agent. Based on the final cured system,

further investigation of the generated system could be performed. An evaluation of the material properties of the system, such as the crack resistance of the fiber-sizing resin interface, would be of great interest, but is beyond the scope of this work. Instead, the curing and possible crack formation during the curing on higher length scales, considering multiple fibers, will be considered in the following chapters.

## 4 Structure generator for FRPs

Fiber-reinforced polymers (FRPs) consist of fibers and resin in which the fibers are embedded. The final microstructure can vary depending on the manufacturing process and materials used. In particular, the ratio of fiber length to diameter has a strong influence on the structure. The compression molding process, which is under consideration in this work, results in long, curved fibers, which form fiber bundles from many individual fibers, cf. Figure 2.3.

The generation of microstructures of straight fibers up to a certain aspect ratio is e.g. described by Schneider [133]. This approach was recently extended to curved fibers by Schneider [134], allowing for higher aspect ratio and more complex structures. These approaches are based on the Sequential Addition and Migration (SAM) algorithm. Fibers are added to the system in multiple steps and iteratively migrated to reduce fiber overlap and fulfill other constraints, such as a desired effective fiber orientation.

In contrast, in this work an approach is presented that is based on molecular dynamics and the Discrete Element Method (DEM). The idea of DEM, which is closely related to molecular dynamics, was proposed by Cundall and Strack [135] for the simulation of the motion of granular media and is a well-established method for describing motion of rigid bodies and an overview is given e.g. by Kafashan et al. [136]. The approach of the present work is restricted to translational degrees of freedom of the particles and thus differs from the classical DEM. The latter often also considers rotational degrees of freedom, and therefore also has to account for angular velocities and torques. In addition, the presented method uses a basic contact model of the DEM. However, friction is neglected and potentials for bonds and angles between fiber

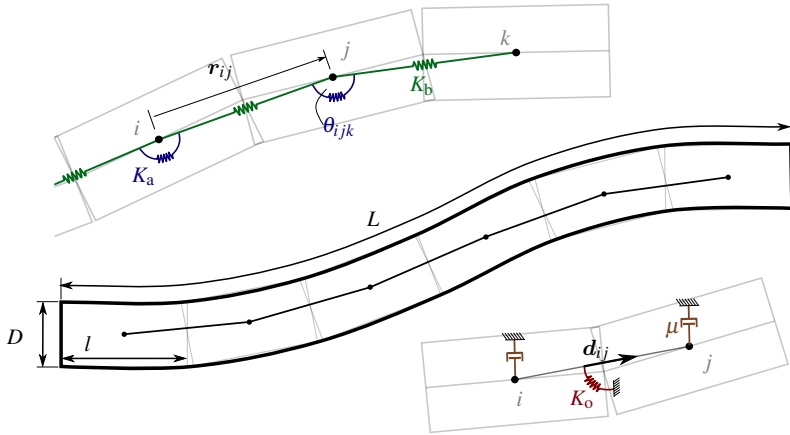


**Figure 4.1:** Interaction of segments in a single curved fiber. Center: A curved fiber with diameter  $D$ , length  $L$  consisting of  $N$  connected segments with length  $l$ . Top: Harmonic bond between consecutive segments with connection vector  $r_{ij}$  and stiffness  $K_b$  as well as bond angle  $\theta_{ij,k}$  and bending stiffness  $K_a$ . Bottom: Contribution due to a mismatch in orientation with a stiffness  $K_o$  and damping by a viscosity  $\mu$ .

segments are introduced. The ability to prescribe a fiber orientation through a fiber orientation tensor has also been implemented in the model, based on the work of Schneider [133].

## 4.1 Fiber description

A system with multiple curved fibers is considered. Each fiber is described by the diameter  $D$ , the length  $L$  and consists of  $N$  connected segments, each with a length  $l = L/N$ , cf. Figure 4.1. Note that the orientation of a fiber segment is not a degree of freedom, but is implicitly given by the position of the segments. For inner segments, the final orientation follows from the normalized average of the neighborhood connection vector, while the orientation of outer segments follows directly from the normalized connection vector, cf. Figure 4.2.

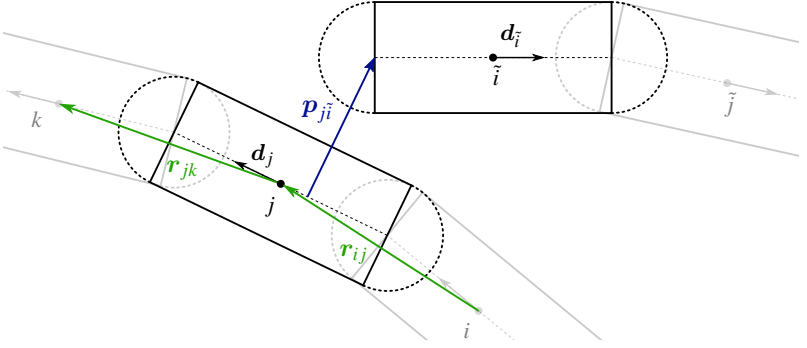


**Figure 4.2:** Connection and orientation vectors, in a fiber and between segments of different fibers. The vectors  $\mathbf{r}_{ij}, \mathbf{r}_{jk}$  describe the connection between the centers of the individual segments, while the unit direction vectors  $\mathbf{d}_j, \mathbf{d}_i$  are averaged from them. The connection vector  $\mathbf{p}_{\tilde{j}i}$  describes the shortest vector between the axis of segments of different fibers.

**Potential energy function** Analogous to classical molecular dynamics, cf. Section 2.5, the potential energy function  $U$  can be introduced by

$$U = \sum_{i,\tilde{i}} U_{i\tilde{i}}^{\text{over}} + \sum_{i>j} U_{ij}^{\text{bond}} + \sum_{i>j>k} U_{ijk}^{\text{angle}} + \sum_{i>j} U_{ij}^{\text{ori}}, \quad (4.1)$$

with a term  $U_{i\tilde{i}}^{\text{over}}$  due to overlapping segments, due to energy stored in the bond of sequential connected segments ( $U_{ij}^{\text{bond}}$ ), and due to bending of segments angle ( $U_{ijk}^{\text{angle}}$ ). In addition, an energy associated with a mismatch in fiber orientation with respect to a prescribed orientation is added via  $U_{ij}^{\text{ori}}$ . Note that the subscript indices  $i\tilde{i}$  denote the interaction between segment  $i$  of one fiber segment and segment  $\tilde{i}$  of another fiber, cf. Figure 4.2, while the indices  $ij$  and  $ijk$  denote two or three consecutive segments of a fiber. The corresponding sums are performed over sets so that all possible interactions of different fibers as well as interactions between individual fibers are considered.

A basic contact model for the potential of overlapping fiber segments is given by

$$U_{i\tilde{i}}^{\text{over}} = \frac{1}{2}K \begin{cases} (|\mathbf{p}_{i\tilde{i}}| - D)^2, & |\mathbf{p}_{i\tilde{i}}| < D \\ 0, & \text{else,} \end{cases} \quad (4.2)$$

with the shortest connection vector  $\mathbf{p}_{i\tilde{i}}$  between the axis of segments of different fibers  $i$  and  $\tilde{i}$ , the norm of a vector  $|\cdot|$ , and a stiffness  $K$ , cf. Figure 4.1 and Figure 4.2. For the computation of the shortest connection vector the algorithm of Pournin et al. [137] is used. The potential for energy in connected fiber segments is given by

$$U_{ij}^{\text{b}} = \frac{1}{2}K_{\text{b}} (|\mathbf{r}_{ij}| - l)^2, \quad (4.3)$$

with the connection vector  $\mathbf{r}_{ij}$  and stiffness  $K_{\text{b}}$ , see Figure 4.1. This formulation penalizes any deviation from  $l$  of the length of a fiber segment. For an angle  $\theta_{ijk}$  between three fiber segments  $i, j$  and  $k$ , the energy follows by

$$U_{ijk}^{\text{a}} = \frac{1}{2}K_{\text{a}}\theta_{ijk}^2, \quad (4.4)$$

with a bending stiffness  $K_{\text{a}}$  that accounts for the energy stored in the fiber due to curvature. Furthermore, the energy for the orientation of a fiber segment is given by

$$U_{ij}^{\text{ori}} = \frac{1}{2}K_{\text{o}} (\mathbf{A} - \tilde{\mathbf{A}}) \cdot (\mathbf{r}_{ij} \otimes \mathbf{r}_{ij}), \quad (4.5)$$

with a parameter  $K_{\text{o}}$  and the prescribed 2<sup>nd</sup> order fiber orientation tensor  $\mathbf{A}$ . The actual fiber orientation of the system follows with

$$\tilde{\mathbf{A}} = \frac{1}{\tilde{N}} \sum_{i>j} \mathbf{d}_{ij} \otimes \mathbf{d}_{ij}, \quad (4.6)$$

which consists of a sum over the number of defined orientation vectors  $\tilde{N}$  with with the corresponding indices  $i$  and  $j$ .

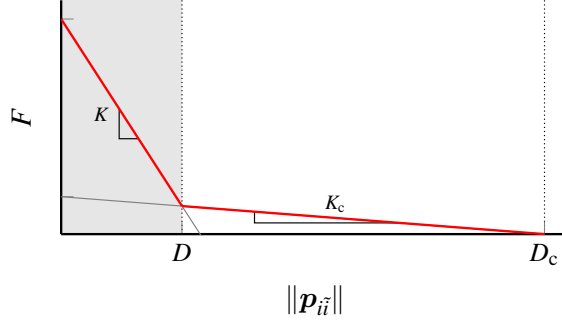


**Figure 4.3:** Implemented force due to overlapping fiber segments. In contrast to the potential  $U_{ii}^{\text{over}}$ , a second stiffness  $K_c$  is introduced. While  $K_c$  is applied from a distance  $D_c$ , the contribution of  $K$  is added below the distance  $D$ .

**Viscous damping** Based on classical molecular dynamics, the equations of motion can be derived from Equations (2.49) and (2.51). Together with a velocity Verlet integration, cf. Section 2.5.2, an NVE ensemble follows. To remove energy from the system, a viscous damping force with a viscosity  $\mu$  is added and the final force follows by

$$\mathbf{f}_i = - \left( \frac{\partial U}{\partial \mathbf{x}_i} + \mu \mathbf{v}_i \right). \quad (4.7)$$

## 4.2 Results

The velocity Verlet integration requires an evaluation of the forces. In addition to the force derived from Equation 4.7, an additional force has been added. The force due to the overlapping of the segments, cf.  $U_{ii}^{\text{over}}$ , was extended by a second term with reduced stiffness but increased distance, cf. Figure 4.3. This additional force should mimic the repulsive force of e.g. a classical Lennard-Jones potential in order to accelerate the generation of non-overlapping structures.

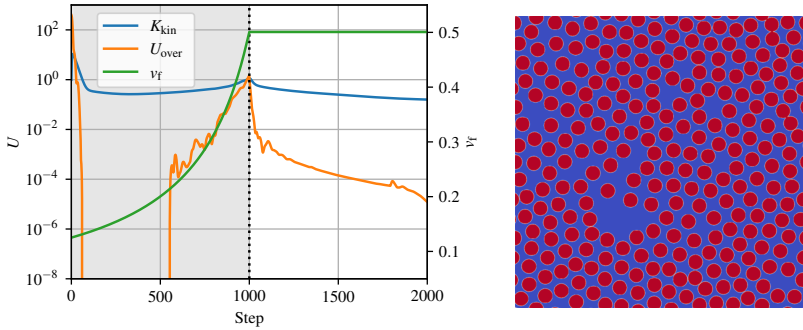


**Figure 4.4:** Left: Evolution of the energies due to overlapping particles  $U_{over}$ , the kinetic energy  $K_{kin}$  and the fiber volume fraction  $v_f$  during the iterations of the generation procedure. Right: Generated square 2D microstructure with unidirectional fibers and a size of 200  $\mu\text{m}$  and 50 % fiber volume fraction.

Description	Symbol	Value
Fiber diameter	$D$	10 $\mu\text{m}$
	$D_c$	15 $\mu\text{m}$
Stiffness	$K$	1 $\frac{\text{kg}}{\text{s}^2}$
	$K_c$	$1 \times 10^{-2} \frac{\text{kg}}{\text{s}^2}$
Viscosity	$\mu$	0.5 $\frac{\text{kg}}{\text{s}}$
Time step	$\Delta t$	1 s

**Table 4.1:** Parameters for the generation fiber structures.

In this work, three different simplifications of a real fiber-reinforced microstructure are considered and described in the following sections. Furthermore, all domain boundaries are considered to be periodic in all directions during the generation.

**Two-dimensional unidirectional fibers** Assuming a matrix reinforced by straight unidirectional fibers with a high aspect ratio, the fiber description can be reduced to the cross sections of the fibers. The generally three-dimensional problem can be reduced in two dimensions. Furthermore, the fiber description does not need to consider multiple fiber segments, angles or orientations. Ultimately, the problem of generating non-overlapping fibers is reduced to placing non-overlapping circles. Therefore, the introduced potentials and forces are simplified accordingly. To avoid inappropriate initial placement of the fibers, the fibers are randomly placed in a much larger domain. In the first step a compression of the domain is performed. In a subsequent step, the system is equilibrated in the sense of a classical MD simulation, which leads to the final microstructures. For a complete list of parameters, the reader is referred to Table 4.1.

Figure 4.4 shows an example of a generated microstructure. The right part of the figure shows the final cross section of such a two-dimensional unidirectional fiber structure with a volume fraction of 50%. The left panel depicts the evolution of the energies due to overlapping particles  $U_{\text{over}}$ , the kinetic energy  $K_{\text{kin}}$  and the fiber volume fraction  $v_f$  during the iterations of the generation procedure. The final value of  $U_{\text{over}}$  indicates that the fibers do not overlap and the remaining energy can be associated with the force due to the low stiffness  $K_c$ , cf. Figure 4.3, leading to a non-zero kinetic energy even for long simulation times.

**Two-dimensional curved fibers** As an alternative to unidirectional fibers, the fibers can be assumed to be placed in one plane. This allows accounting for curved fibers, along with energies in bonds, angles, as well as different fiber orientations. Still it allows a reduction of the general system to a 2D system. Therefore, the number of possible interactions is greatly reduced and the individual calculation can also be simplified. The parameters for generating the structures are listed in Table 4.1 and Table 4.2. In addition, an orientation is chosen with 90% probability in the preferred direction.

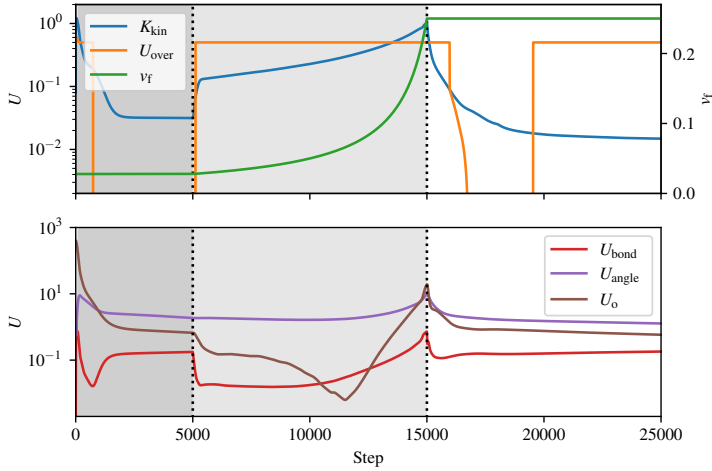


**Figure 4.5:** Evolution of the different energies and the fiber volume fraction  $v_f$  during the iterations of the generation procedure.

Description	Symbol	Value
Fiber length	$L$	200 $\mu\text{m}$
No. segments	$N$	20 (2D), 10 (3D)
Stiffness	$K_b$	$1.0 \frac{\text{kg}}{\text{s}^2}$
	$K_a$	$1.0 \times 10^1 \frac{\text{kg} \mu\text{m}^2}{\text{s}^2}$
	$K_o$	$1.0 \times 10^1 \frac{\text{kg}}{\text{s}^2}$

**Table 4.2:** Additional parameters for the generation of curved fiber structures. The remaining parameters are listed in Table 4.1.

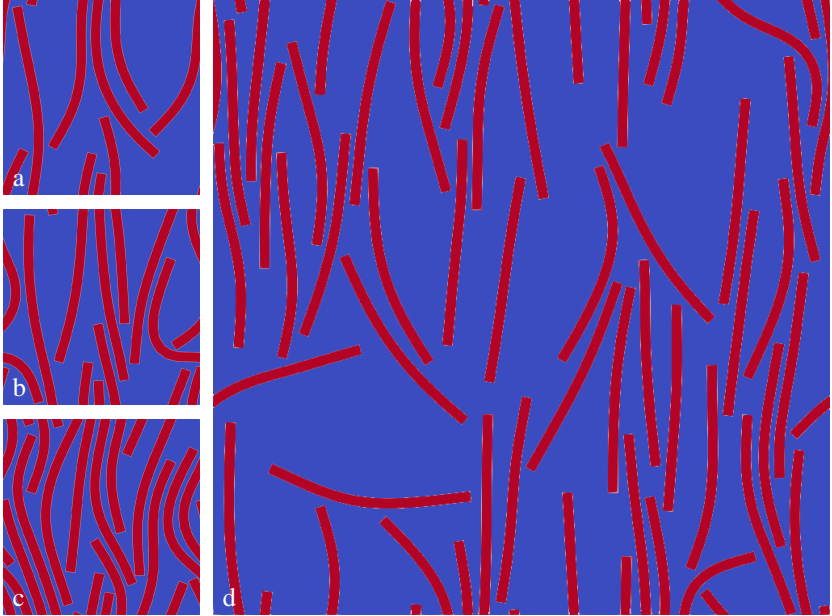


**Figure 4.6:** Generated quadratic 2D microstructures with curved fiber. Smaller  $200\ \mu\text{m}$  systems with 25 % (a), 35 % (b), and 50 % (c) fiber volume fraction. And a larger  $600\ \mu\text{m}$  system with 25 % fiber volume fraction (d).

Figure 4.6 depicts generated two-dimensional curved fiber structures for different domain sizes and volume fractions. Figure 4.5 shows the evolution of the energy contributions as well as the volume fraction over the simulation time. The generation procedure consists of three steps. The fibers are randomly placed in a large system to avoid overlapping fibers, which can lead to unstable behavior. After compressing the domain, the system is equilibrated to obtain the final microstructure. Although the two-dimensional final structures represent fibers with a circular cross section, they are treated differently in this work. The reduction to the two-dimensional case is chosen mainly to reduce

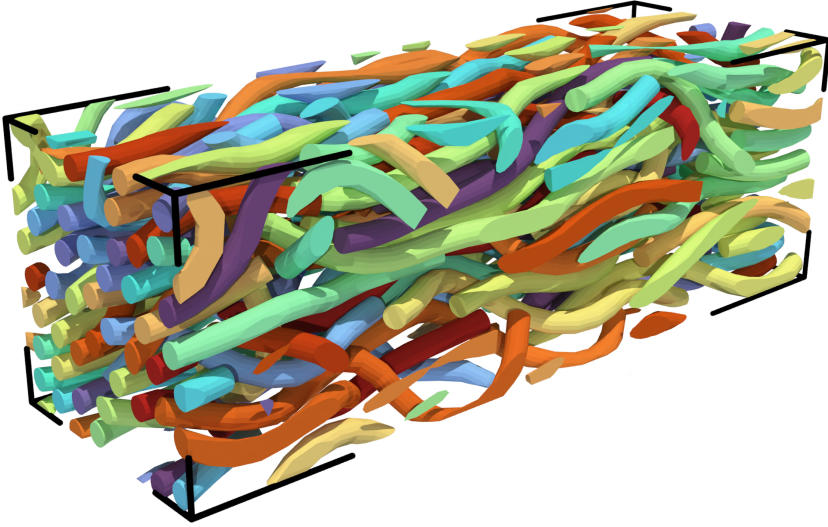


**Figure 4.7:** Generated 3D microstructures with curved fiber and a system size of  $360 \times 120 \times 120 \mu\text{m}$  and 25 % fiber volume fraction.

the computational effort in subsequent steps. As a disadvantage, the properties of round fibers are lost and instead an infinitely thick structure is depicted based on the generated structures.

**Three-dimensional curved fibers** Finally, the introduced fiber description can be considered in the general three-dimensional case. For the latter case, the parameters for generating the structures are listed in Table 4.1 and Table 4.2. Note that the number of segments is reduced to 10 to limit the number of degrees of freedom compared to the last section. Moreover, the orientation in the preferred direction is chosen to 80 % and 10 % in both other directions. In addition, the size of the simulation domain is modified according to the preferred direction and the aspect ratio of the fiber. An exemplary final three-dimensional fiber-reinforced structure with curved fibers is shown in Figure 4.7.

# 5 Curing simulations of FRTS on a micro scale

After considering the curing of UPPH resin in combination with a glass fiber based on molecular dynamics simulation in Chapter 3 at the nanoscale, the curing simulations are performed at the microscopic length scale. First, based on continuum mechanics, the heat equation is derived and a curing model, along with curing shrinkage and thermal expansion strain, is introduced. Finally, various fiber-reinforced volume elements (see Chapter 4) are generated to study the curing degree, temperature, and stress distribution during a compression molding process.

## 5.1 Model

The curing model of this work is based on the work of Schwab [138]. However, instead of introducing the phasefield and the degree of cure as separate degrees of freedom, a derivation based on a thermomechanically weakly coupled theory is chosen, cf. e.g. Prahs et al. [139]. Based on such a model, a source term based on the curing model and a strain decomposition are introduced to account for thermal strains and curing shrinkage.

**Clausius-Duhem inequality** In the following, following the small deformation theory, a constant mass density  $\rho$  is assumed. Furthermore, the Helmholtz free energy is decomposed by

$$\psi = \psi_{el} + \psi_{\theta}, \quad \psi_{el} \neq \psi_{el}(\theta), \quad \psi_{\theta} \neq \psi_{\theta}(\varepsilon), \quad (5.1)$$

into a purely elastic and a purely thermal contribution. The CDI, cf. Section 2.2.2, follows by

$$\sigma \cdot \dot{\varepsilon} - \rho \dot{\psi} - \rho \eta \dot{\theta} - \frac{\mathbf{q} \cdot \mathbf{g}}{\theta} \geq 0 \quad (5.2)$$

and, taking into account equation Equation (5.1) it can be rewritten as

$$\left( \sigma - \rho \frac{\partial \psi}{\partial \varepsilon} \right) \cdot \dot{\varepsilon} - \rho \left( \eta + \frac{\partial \psi}{\partial \theta} \right) \dot{\theta} - \frac{\mathbf{q} \cdot \mathbf{g}}{\theta} \geq 0. \quad (5.3)$$

This results in the potential relations

$$\sigma = \rho \frac{\partial \psi}{\partial \varepsilon}, \quad \eta = - \frac{\partial \psi}{\partial \theta}, \quad (5.4)$$

cf. eg. [85].

**Heat conduction** The localized balance of internal energy, cf. Equation (2.15), is given by

$$\rho \dot{e} = \rho r + \sigma \cdot \dot{\varepsilon} - \text{div}(\mathbf{q}). \quad (5.5)$$

With  $e = \psi + \eta \theta + \eta \dot{\theta}$  and using the derived potential relations, the balance can be rewritten as

$$\rho \frac{\partial \psi}{\partial \varepsilon} \cdot \dot{\varepsilon} + \rho \frac{\partial \psi}{\partial \theta} \dot{\theta} - \rho \frac{\partial^2 \psi}{\partial \theta \partial \theta} \dot{\theta} - \rho \frac{\partial \psi}{\partial \theta} \dot{\theta} = \rho r + \rho \frac{\partial \psi}{\partial \varepsilon} \cdot \dot{\varepsilon} - \text{div}(\mathbf{q}). \quad (5.6)$$

This can be further simplified, leading to

$$-\rho \frac{\partial^2 \psi}{\partial \theta \partial \theta} \dot{\theta} = \rho r - \operatorname{div}(\mathbf{q}), \quad (5.7)$$

and with the definition of the specific heat capacity at constant volume  $c_V = -\rho \frac{\partial^2 \psi}{\partial \theta \partial \theta}$ , the heat equation is given by

$$c_V \dot{\theta} = \rho r - \operatorname{div}(\mathbf{q}). \quad (5.8)$$

**Thermal jump conditions** Analogous to the mechanical jump conditions, cf. Section 2.3.3, jump conditions can also be formulated accounting for thermal measures. The effective temperature gradient  $\mathbf{g}$  and the effective heat flux  $\mathbf{q}$  are decomposed by a linear interpolation with the order parameters given by

$$\mathbf{q} = \sum_{\alpha}^N \phi^{\alpha} \mathbf{q}^{\alpha}, \quad \mathbf{g} = \sum_{\alpha}^N \phi^{\alpha} \mathbf{g}^{\alpha}, \quad (5.9)$$

with the phase-specific fields  $\mathbf{q}^{\alpha}, \mathbf{g}^{\alpha}$  for each phase. In addition, the Fourier law

$$\mathbf{q}^{\alpha} = -\kappa^{\alpha} \mathbf{1} \mathbf{g}^{\alpha}, \quad (5.10)$$

with isotropic thermal conductivity  $\kappa^{\alpha}$  is introduced for each phase. This is followed by the thermal jump conditions

$$[[\mathbf{q}]]^{\alpha\beta} \mathbf{n}^{\alpha\beta} = 0, \quad [[\mathbf{g}]]^{\alpha\beta} = \tilde{a}^{\alpha\beta} \mathbf{n}^{\alpha\beta}, \quad (5.11)$$

which limit the heat flux in the normal direction and a scalar jump in the temperature gradient  $\tilde{a}^{\alpha\beta}$ . Based on this assumption, an effective, generally anisotropic, thermal conductivity can be determined as a function of the order parameters, their orientation, and the individual thermal conductivities of the phases.

**Strain decomposition** The effective strain is decomposed into phase-specific strains  $\varepsilon^\alpha$ , and these are further decomposed by

$$\varepsilon = \sum_{\alpha}^N \phi^{\alpha} \varepsilon^{\alpha}, \quad \varepsilon^{\alpha} = \varepsilon_{\text{el}}^{\alpha} + \varepsilon_{\theta}^{\alpha} + \varepsilon_{\chi}^{\alpha}, \quad (5.12)$$

with an elastic contribution  $\varepsilon_{\text{el}}^{\alpha}$ , a thermal strain  $\varepsilon_{\theta}^{\alpha}$ , and a strain  $\varepsilon_{\chi}^{\alpha}$  due to curing shrinkage. The latter can be formulated by

$$\varepsilon_{\theta}^{\alpha} = \alpha^{\alpha} \mathbf{1} (\theta - \theta_{\text{ref}}^{\alpha}), \quad \varepsilon_{\chi}^{\alpha} = \frac{\chi_r^{\alpha}}{3} \mathbf{1} \zeta^{\alpha}, \quad (5.13)$$

with a reference temperature  $\theta_{\text{ref}}^{\alpha}$  at which the thermal strain disappears, a thermal expansion coefficient  $\alpha^{\alpha}$ , the total curing shrinkage  $\chi_r^{\alpha}$  and the curing degree  $\zeta^{\alpha}$  for a phase  $\alpha$  denoted by the superscript. In addition, the phase-specific stresses and strain energy densities are reformulated in terms of the elastic strain, yielding

$$\boldsymbol{\sigma}^{\alpha} = \mathbb{C}^{\alpha} \left[ \varepsilon^{\alpha} - \varepsilon_{\theta}^{\alpha} - \varepsilon_{\chi}^{\alpha} \right], \quad (5.14)$$

$$f^{\alpha} = \frac{1}{2} \left( \varepsilon^{\alpha} - \varepsilon_{\theta}^{\alpha} - \varepsilon_{\chi}^{\alpha} \right) \cdot \mathbb{C}^{\alpha} \left[ \varepsilon^{\alpha} - \varepsilon_{\theta}^{\alpha} - \varepsilon_{\chi}^{\alpha} \right]. \quad (5.15)$$

**Reaction enthalpy** With the specific enthalpy  $h$ , the degree of cure  $\zeta^{\alpha}$  of a phase  $\alpha$  can be defined by

$$\zeta^{\alpha}(t) = \frac{h^{\alpha}(t)}{h^{\alpha,\text{tot}}}, \quad (5.16)$$

with the total reaction enthalpy  $h^{\alpha,\text{tot}} \leq 0$ . Further the rate of curing degree is constrained by  $\dot{\zeta}^{\alpha} \geq 0$  to satisfy the second law of thermodynamics. An ansatz for the source term of the heat equation (5.8) is introduced by

$$\rho r = - \sum_{\alpha}^N \phi^{\alpha} \dot{\zeta}^{\alpha} h^{\alpha,\text{tot}}. \quad (5.17)$$

**Kamal-Sourour model** The model for predicting the curing process of UPPH is based on the Kamal-Sourour kinetic model [140, 141]. This approach was recently applied to an epoxy resin by Bernath et al. [142]. The degree of cure  $\zeta^\alpha \in [0, 1]$  describes the degree of conversion of the underlying polymerization from uncured state  $\zeta^\alpha = 0$  to the fully cured state  $\zeta^\alpha = 1$  of one phase or subregion  $\alpha$ . It can also be phenomenologically related to the amount of enthalpy provided by the polymerization, cf. Equation (5.16). The rate of cure follows by the ordinary differential equation

$$\dot{\zeta}^\alpha(\zeta^\alpha, \theta) = (k^{\alpha,1}(\theta) + k^{\alpha,2}(\theta)(\zeta^\alpha)^m)(1 - \zeta^\alpha)^n, \quad (5.18)$$

with the exponents  $m, n$  and the kinetic functions  $k^{\alpha,1}, k^{\alpha,2}$ . The latter can be described by the Arrhenius equations

$$k^{\alpha,1}(\theta) = A^{\alpha,1} \exp\left(-\frac{E^{\alpha,1}}{R\theta}\right), \quad k^{\alpha,2}(\theta) = A^{\alpha,2} \exp\left(-\frac{E^{\alpha,2}}{R\theta}\right), \quad (5.19)$$

with the prefactors  $A^{\alpha,1}, A^{\alpha,2}$ , the activation energies  $E^{\alpha,1}, E^{\alpha,2}$  and the universal gas constant  $R$ .

**Glass transition temperature** The glass transition temperature  $\theta^{\alpha,g}$  describes a change of state of polymers. Below  $\theta^{\alpha,g}$  the material is often characterized by brittle material behavior, while above the glass transition temperature it often exhibits viscous behavior, which can be associated with a rubbery state. In the context of the curing process, there is no expected evolution of the degree of cure below the transition temperature. Since the Kamal-Sourour model does not account for such a transition, the approach of DiBenedetto [143] is used to describe the glass transition temperature as a function of the degree of cure, yielding

$$\frac{\theta^{\alpha,g}(\zeta^\alpha) - \theta^{\alpha,g0}}{\theta^{\alpha,g\infty} - \theta^{\alpha,g0}} = \frac{\lambda^\alpha \zeta^\alpha}{1 - (1 - \lambda^\alpha) \zeta^\alpha}, \quad (5.20)$$

Description	Symbol	Value
Mass density	$\rho$	2575 $\frac{\text{kg}}{\text{m}^3}$
Specific heat capacity	$c_v$	802.4 $\frac{\text{J}}{\text{kgK}}$
Thermal conductivity	$\kappa$	1.275 $\frac{\text{W}}{\text{mK}}$
Bulk modulus	$K$	46.5 GPa
Shear modulus	$G$	33 GPa
Thermal expansion coefficient	$\alpha$	$1 \times 10^{-6} \frac{1}{\text{K}}$

**Table 5.1:** Material parameters for the glass fiber. Values are taken from Schwab [138] (Table 4.12), besides the thermal expansion coefficient.

with the glass transition temperature  $\theta^{\alpha, g^0}$  for no cure and fully cured  $\theta^{\alpha, g^\infty}$ , respectively, and the parameter  $\lambda^\alpha$ , which can be determined e.g. experimentally [142] or by molecular dynamics simulations [76].

## 5.2 Results

Although the model was introduced with a degree of cure for all phases, i.e. materials, in the following only the resin undergoes a curing process and solely exhibits curing shrinkage. Therefore, in the following, the superscript is omitted for quantities related to cure, but always denotes the quantity of the resin material.

The material properties used for the glass fiber are listed in Table 5.1 and are assumed to be constant over the considered temperatures. For both resin and glass fiber, the reference temperature  $\theta_{\text{ref}}^\alpha$  is assumed to be 293 K. In contrast, the references to the material properties of the UPPH resin used, including curing parameters, are listed in Table 5.2. Many of the parameters are temperature and/or cure dependent. This dependence is modeled by linear or bilinear interpolation between the tabular data provided in the corresponding references.

Description	Symbol	Dependency	Reference
Mass density	$\rho$	$\theta, \zeta$	[76], Table 9
Specific heat capacity	$c_v$	$\theta, \zeta$	[76], ESI Table S4
Thermal conductivity	$\kappa$	$\theta, \zeta$	[76], ESI Table S6
Bulk modulus	$K$	$\theta, \zeta$	[76], ESI Table S7
Shear modulus <sup>a</sup>	$G$	$\theta, \zeta$	[138], Table 4.11
Thermal expansion coefficients	$\alpha$	$\theta^g, \zeta$	[76], Table 11
Volume shrinkage	$\chi_t$	$\theta$	[76], Table 8
Reaction enthalpy	$h^{\text{tot}}$	–	[76], Table 10
Kamal-Sourour parameters <sup>b</sup>	$A^1, A^2, E^1, E^2, m, n$	–	[138], Table 4.11
DiBenedetto parameters	$\theta^{g^0}, \theta^{g^\infty}, \lambda$	–	[138], Table 4.11

**Table 5.2:** References for the material parameters for the UPPH resin based on the work of Schwab and Denniston [76] and Schwab [138].

<sup>a</sup>In addition 212 MPa for 293 K and zero curing degree is assumed.

<sup>b</sup>The unit of  $A^1, A^2$  in Schwab [138] should be, based on a personal communication, be  $\text{min}^{-1}$  and have been corrected accordingly.

The maximum absolute principal stress is defined by

$$\sigma^* = \max_{i=1,2,3} |\sigma^i|, \quad (5.21)$$

which is used to visualize the stress states of the microstructures during curing. In addition, the volume average is defined by

$$\langle \psi \rangle = \frac{1}{V} \int_{\Omega} \psi \, dv \quad (5.22)$$

for a arbitrary field  $\psi$ .

**Boundary and initial conditions** The initial temperature of the simulation domain is defined as room temperature with 293 K. While the initial curing degree is set to  $1 \times 10^{-3}$  to avoid numerical difficulties due to the singular point of the model at zero curing degree. The boundaries are all considered periodic, except in one direction, which is associated with two sides of the molds, denoted by  $\partial\Omega_M$ . Therefore, the normal displacement are restricted in this direction with

$$\mathbf{u} \cdot \mathbf{n} = 0, \quad \text{on } \partial\Omega_M, \quad (5.23)$$

with the outer normal  $\mathbf{n}$  of the boundary. For the heat equation, a Robin-type boundary condition is chosen on these boundaries. The heat flux is given by

$$\mathbf{q} \cdot \mathbf{n} = h(\theta - \theta_{\infty}), \quad \text{on } \partial\Omega_M, \quad (5.24)$$

with a heat transfer coefficient  $h$  and the environmental temperature  $\theta_{\infty}$ . In the following, a variation of the domain size is investigated. The total thickness of the component is assumed to be 2 mm and the heat transfer coefficient is chosen as  $h = C/\Delta l$ , with the length difference  $\Delta l$  between the simulation domain and the total thickness of the component, and the coefficient  $C = 1 \times 10^{-2} \text{ W m}^{-1} \text{ K}^{-1}$ . This approach takes into account the thermal damping of the component not modeled and avoids overly high heat fluxes for smaller simulation domains.

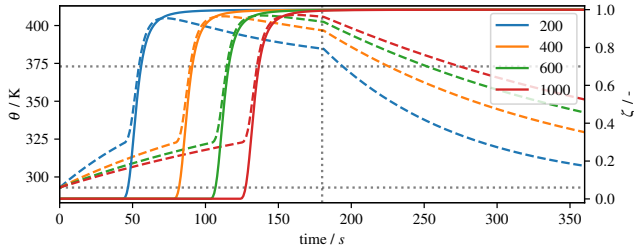


**Figure 5.1:** Temporal evolution of effective curing degree  $\langle \zeta \rangle$  (solid line) and effective temperature  $\langle \theta \rangle$  (dashed line) during the cure process for **pure resin** and different system sizes in  $\mu\text{m}$ .

To model the compound molding process, the simulation is divided into two steps:

- Closing the molds and heating the SMC prepreg to initialize the curing process. This is accomplished by setting  $\theta_\infty$  to 373 K.
- The molds are opened and the final component is cooled to room temperature. Therefore,  $\theta_\infty$  is reset to 273 K after 3 minutes.

### 5.2.1 Pure resin

In the first step, a homogeneous domain with pure UPPH resin is considered to see the influence of the reinforcement by the glass fibers in the subsequently sections. Figure 5.1 shows the effective curing degree  $\langle \zeta \rangle$  and the effective temperature  $\langle \theta \rangle$  during the curing simulation. After reaching the initial glass transition temperature of 323 K, the curing starts and due to the exothermic reaction, the temperature increases and reaches temperatures above  $\theta_\infty$ . The curing degree reaches the final value quite early, before the cured resin slowly cools down to room temperature. The different domain sizes have different thermal inertia and heat transfer coefficients, resulting in different heating and cooling kinetics due to the boundary conditions. In contrast, the evolution of the curing degree is only slightly affected, except for a time shift.

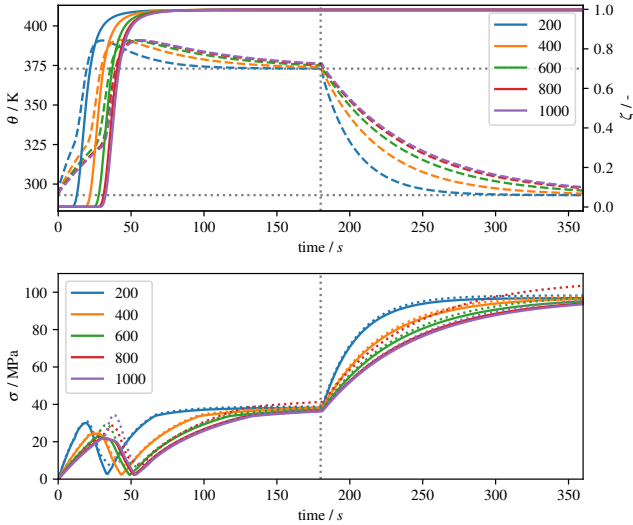


**Figure 5.2:** Top: Temporal evolution of effective curing degree  $\langle \zeta \rangle$  (solid line) and effective temperature  $\langle \theta \rangle$  (dashed line). Bottom: Temporal evolution of effective maximum principal stress  $\langle \sigma^* \rangle$  (solid line) and local maximum principal stress (dashed line). These are plotted during the curing process for **unidirectional fiber-reinforced** domains with a fiber volume fraction of 25 % and different system sizes in  $\mu\text{m}$ .

## 5.2.2 Unidirectional fiber-reinforced

In the next step, simulation studies with unidirectionally fiber-reinforced domains, cf. Section 4.2, are investigated. Figure 5.2 displays the effective curing degree, the effective temperature and the maximum principal stress  $\langle \sigma^* \rangle$  during the curing simulation of a domain with a volume fraction of 25 %. In contrast to the pure resin, the high conductivity and relatively low heat capacity of the glass fiber increase the rate of the effective temperature. This leads to an earlier start of the cure process and the final room temperature is also reached earlier. The maximum principal stress is caused by the interaction of strains due to thermal expansion, curing shrinkage and the different stiffness of both materials, which changes during the curing process. The highest effective and

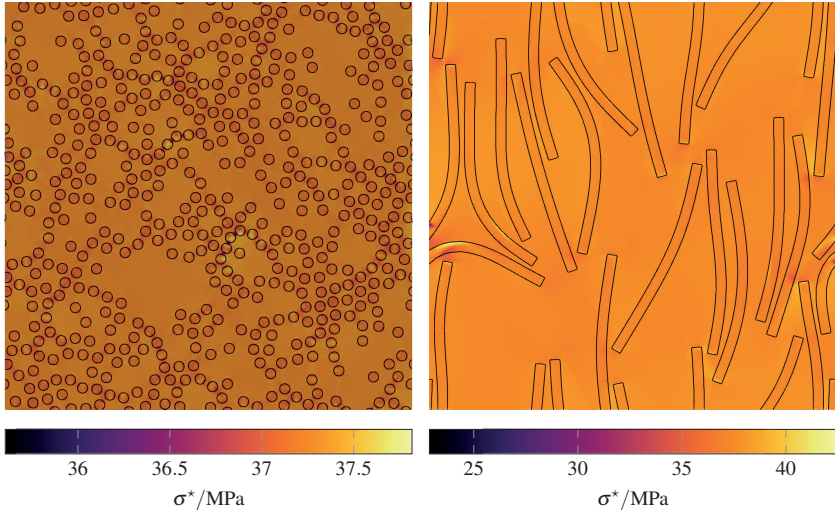


**Figure 5.3:** Distribution of maximum principal stress  $\sigma^*$  for a square domain of  $400\ \mu\text{m}$  length with a fiber volume fraction of 25 % for a unidirectional fiber-reinforced system (left) and a two-dimensional curved fiber-reinforced system (right) after curing simulation.

local values were observed at room temperature after curing. This indicates that the final curing shrinkage is the main cause of these stresses. Figure 5.3 shows an example of the final distribution of the maximum principal stress for a 25 % volume fraction domain. In the resin-rich areas, the stress is mostly homogeneous, while the fiber cross section introduces local stress concentrations.

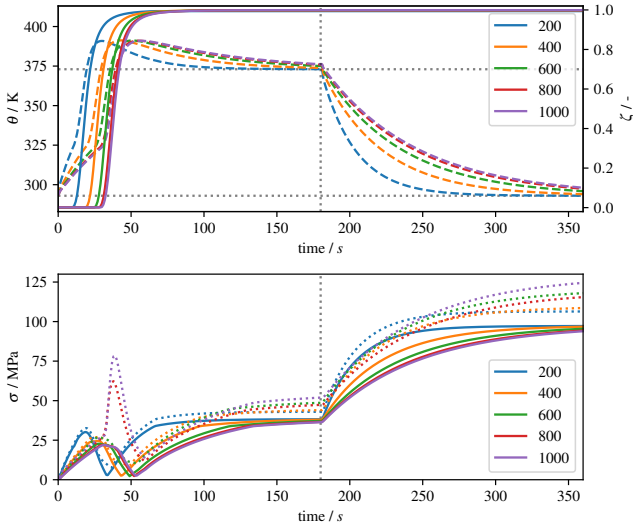


**Figure 5.4:** Top: Temporal evolution of effective curing degree  $\langle \zeta \rangle$  (solid line) and effective temperature  $\langle \theta \rangle$  (dashed line). Bottom: Temporal evolution of effective maximum principal stress  $\langle \sigma^* \rangle$  (solid line) and local maximum principal stress (dashed line). These are plotted during the curing process for **two-dimensional curved fiber-reinforced** domains with 25 % fiber volume fraction and different system sizes in  $\mu\text{m}$ .

### 5.2.3 Two-dimensional curved fibers

Figure 5.3 illustrates the final distribution of the maximum principal stress for a 25 % volume fraction domain with a curved fiber in two dimensions, cf. Section 4.2. In contrast to the unidirectional fiber-reinforced system, the distribution is more homogeneous because the curved fiber domains contain larger resin-rich areas for a given fiber volume fraction. However, the sharp corner of the curved fibers introduces locally higher stresses. Figure 5.4 shows the temperature, curing degree, and maximum principal stress over time. While the temperature and curing degree are similar to the unidirectionally fiber-reinforced variant, higher principal stress can be observed. In particular, some ensembles show a peak of the local maximum stress at the beginning of the cure.

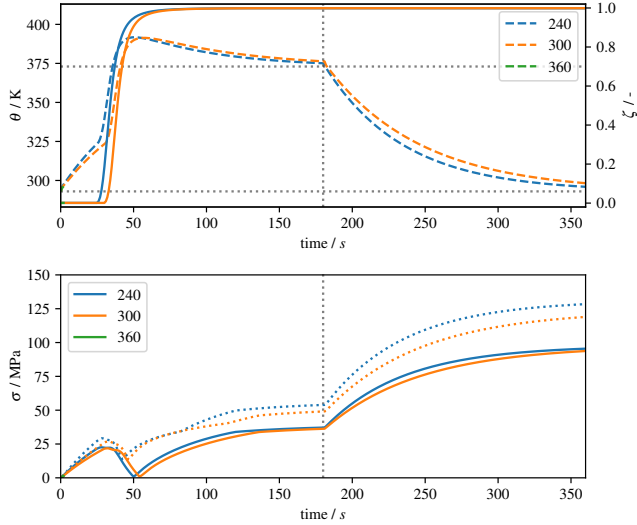


**Figure 5.5:** Top: Temporal evolution of effective curing degree ( $\langle \zeta \rangle$ ) (solid line) and effective temperature ( $\langle \theta \rangle$ ) (dashed line). Bottom: Temporal evolution of effective maximum principal stress ( $\langle \sigma^* \rangle$ ) (solid line) and local maximum principal stress (dashed line). The is plotted during the curing process for **three-dimensional curved fiber-reinforced** domains and different and different system sizes in  $\mu\text{m}$ .

## 5.2.4 Three-dimensional curved fibers

Finally curing simulations of three-dimensional curved fiber, cf. Section 4.2, are conducted. Figure 5.5 shows the temperature, curing degree, and maximum principal stress over time. While the curing and temperature evolution is similar to the two-dimensional cases the simulation demonstrate higher maximum principal stresses, since the full three-dimensional feature of the curved fibers can be depicted correctly. The maximum principal stresses are visualized in Figure 5.6, whereas regions with lower values are omitted and only the regions of high stresses are highlighted in color.

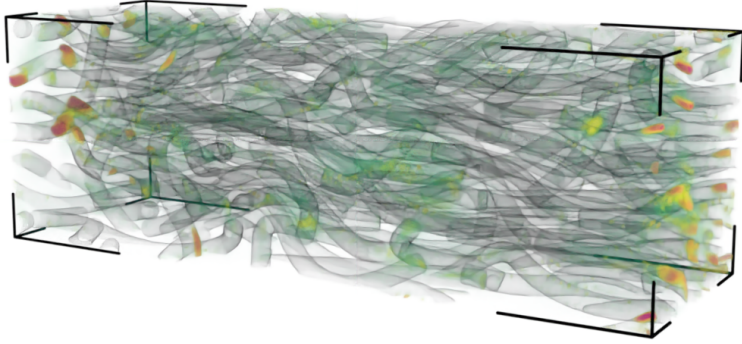


**Figure 5.6:** Distribution of maximum principal stress  $\sigma^*$  of a three-dimensional curved fiber-reinforced system with 25 % fiber volume fraction after curing simulation. Red highlights maximum values, while lower values have reduced opacity to ensure clarity.

## 5.2.5 Comparison

During curing, the material parameters of UPPH materials change significantly. However, when different volume fractions are considered, the change in e.g. effective conductivity and thermal inertia is dominated by the glass fiber. The difference in the evolution of cure degree and temperature for different abstraction levels of the volume element or selected ensemble seems to be small. In contrast, the mechanical behavior seems to be different for the three levels of abstraction. Therefore, a study with varying fiber volume fraction is performed for all three variants of the fiber-reinforced system. For each type and volume fraction, simulations were performed on 5 different ensembles with a size of  $400 \times 400 \mu\text{m}$  (2D) and  $240 \times 80 \times 80 \mu\text{m}$  (3D), respectively. Figure 5.7 shows the maximum principal stress over the fiber volume fraction for these cases. Therefore, both the effective value and the maximum value are plotted and confidence intervals are provided. Almost no scatter for the effective maximum principal stress can be observed despite the use of different ensembles. Only a larger difference between the two-dimensional and three-dimensional cases is present. This indicates that the different geometry of the two-dimensional cases does not cause any difference in the effective behavior, only the change

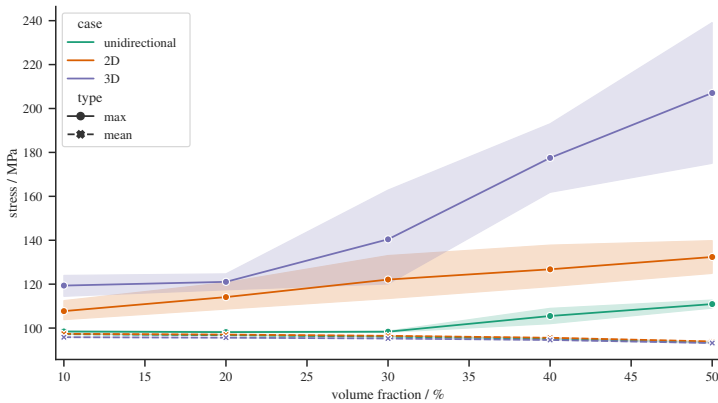


**Figure 5.7:** Maximum principal stress  $\sigma^*$  over fiber volume fraction for unidirectional, 2D curved and 3D curved fibers. The effective value as well as the maximum value are plotted. Based on different ensembles, a confidence interval is also provided.

to a three-dimensional strain state leads to higher stresses. In addition, the value decreases for higher volume fractions because the a higher fraction of the domain do not exhibit curing shrinkage.

The local maximum principal stress increases with the complexity of the microstructure. The unidirectional fiber-reinforced systems have the lowest value and the three-dimensional curved fiber case the highest value. The ability to generate complex three-dimensional stress states increases with the complexity of the represented fiber shape. Also, with higher fiber volume fractions, the likelihood of unfavorable fiber positions, and thus areas of stress concentration increases. In particular, a strong increase in stress of the three-dimensional system from 20 % to 40 % volume fraction can be observed.

It can be concluded that while simplifying the real microstructure of FRTS to two-dimensional structures does introduce an error in predicting stresses, it nevertheless allows investigating the basic qualitative mechanism of the mechanical behavior of glass fiber-reinforced UPPH resin at reduced computational costs.



## 6 Phase-field modeling of crack propagation in heterogeneous materials

In this chapter, phase-field models for crack propagation are introduced and their application especially to heterogeneous systems such as FRPs is discussed. First, a crack propagation model for a homogeneous system is presented, which is based on simple but well-established models from the literature. Subsequently, two models for heterogeneous systems follow by generalization of the homogeneous model. The single-crack order parameter (SCOP) model describes fracture by a single parameter for all phases, i.e. materials. In contrast, multiple parameters are introduced for the multi-crack order parameters (MCOP). Along with some numerical remarks and an extension to a single-obstacle potential, numerical results are discussed. A qualitative and quantitative comparison of the SCOP and MCOP is performed. Furthermore, the basic Voigt-Taylor scheme is compared to the mechanical jump condition framework, cf. Section 2.3 and Schneider et al. [60]. Finally, the application of these models to FRPs will be demonstrated, restricted to systems with external loads, excluding the curing process. This chapter is mainly based on the work of Schöller et al. [1, 3], denoted by footnotes, but also includes several extensions of these works.

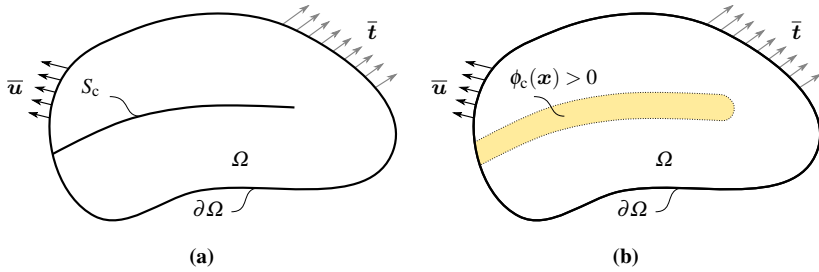


**Figure 6.1:** Schematic homogeneous domain with a sharp crack interface (a) and a diffuse crack interface in yellow (b).

## 6.1 Phase-field crack propagation models<sup>1</sup>

### 6.1.1 Classical homogeneous model

For a material body  $\Omega \in \mathbb{R}^n$   $n \in \{1, 2, 3\}$ , in an Euclidean space, the displacement vector  $\mathbf{u}$  relates the position vector of a material point in the current configuration relative to the reference configuration. The boundary of the body  $\partial\Omega \in \mathbb{R}^{n-1}$  consists of a subset  $\partial\Omega_D$ , on which a Dirichlet boundary condition is applied, by prescribing the displacement vector  $\mathbf{u} = \bar{\mathbf{u}}$ , while a Neumann boundary condition is imposed on  $\partial\Omega_N$ , for which the stress vector  $\mathbf{t} = \bar{\mathbf{t}}$  is specified. For both boundaries,  $\partial\Omega_D \cup \partial\Omega_N = \partial\Omega$  and  $\partial\Omega_D \cap \partial\Omega_N = \emptyset$  must apply. In addition, the body contains a sharp crack surface  $S_c$ .

<sup>1</sup>The content of this section has been taken directly from Schöller et al. [1] with minor linguistic changes.

**Free energy functional** For a homogeneous domain containing a sharp crack, cf. Figure 6.1a, the free energy functional is proposed by

$$\mathcal{F}[\mathbf{u}] = \int_{\Omega} f_{\text{el}}(\mathbf{u}) \, dv + \int_{S_c} G_c \, da, \quad (6.1)$$

with a strain energy density  $f_{\text{el}}(\mathbf{u})$  and a critical energy release rate  $G_c$ , which describes the surface energy density  $\gamma$  for the sharp crack surface by  $G_c = 2\gamma$ . The introduction of the crack order parameter  $\phi_c \in [0, 1]$  enables a smooth transition of the material state. For  $\phi_c = 1$ , the material is fully broken, for  $\phi_c = 0$ , it remains undamaged. Following Kuhn and Müller [28], this allows the free energy (6.1) to be rewritten by a volume integral

$$\mathcal{F}[\mathbf{u}, \phi_c, \nabla \phi_c] = \int_{\Omega} \underbrace{h(\phi_c) f_{\text{el}}(\mathbf{u}) + \frac{1}{2} G_c \left( \varepsilon_{\phi_c} |\nabla \phi_c|^2 + \frac{1}{\varepsilon_{\phi_c}} \phi_c^2 \right)}_{f(\mathbf{u}, \phi_c, \nabla \phi_c)} \, dv, \quad (6.2)$$

cf. Figure 6.1b. The strain energy density is degraded by the function  $h(\phi_c) = (1 - \phi_c)^2$ . For a general discussion of degradation functions, the reader is referred to Kuhn et al. [144]. The energy of the crack is parameterized by  $\phi_c^2$  and a gradient term with the spatial gradient  $\nabla \phi_c = \text{grad}(\phi_c)$  and its norm  $|\nabla \phi_c| = \sqrt{\nabla \phi_c \cdot \nabla \phi_c}$ . In addition, the length parameter  $\varepsilon_{\phi_c}$  defines the width of the diffuse interface.

**Strain energy density** The elastic term of the free energy functional (6.2) is modeled by an elastic potential, assuming small deformations. Thus, the strain energy density reads

$$f_{\text{el}}(\mathbf{u}) = \frac{1}{2} \boldsymbol{\sigma} \cdot \boldsymbol{\varepsilon}, \quad (6.3)$$

with the strain tensor  $\varepsilon = \text{sym}(\text{grad}(\mathbf{u}))$ , where  $\text{sym}(\cdot)$  denotes the symmetric part of a second order tensor. In addition, Hooke's law

$$\boldsymbol{\sigma} = \mathbb{C}[\boldsymbol{\varepsilon}], \quad (6.4)$$

is assumed, with the symmetric Cauchy stress tensor  $\boldsymbol{\sigma}$ , and the 4<sup>th</sup> order stiffness tensor  $\mathbb{C}$ . Moreover, body forces are neglected and a quasi-static behavior is subsequently considered. For an isotropic case, this constitutive equation simplifies to  $\boldsymbol{\sigma} = \lambda \text{tr}(\boldsymbol{\varepsilon}) \mathbf{1} + 2\mu\boldsymbol{\varepsilon}$ , with the Lamé parameters  $\lambda$  and  $\mu$ , the second-order identity tensor  $\mathbf{1}$ , and the trace operator  $\text{tr}(\cdot)$ . The Lamé parameters can also be expressed by Young's modulus  $E$  and Poisson's ratio  $\nu$ , using

$$\lambda = \frac{E\nu}{(1+\nu)(1-2\nu)}, \quad \mu = \frac{E}{2(1+\nu)}. \quad (6.5)$$

As cracks typically do not evolve under compression loads, several approaches exist to split the strain energy density into a tension and compression part. By only degrading the tension part, this results in a more physical crack propagation behavior. Early tension-compression splits were introduced by Amor et al. [145], Miehe et al. [146] and Henry and Levine [26]. More recent variants were proposed by Ambati et. al [34], Strobl and Seelig [147] and Storm et al. [148]. Despite their significance, none of these variants is considered here, in order to reduce the complexity of the proposed model. However, an extension to most of the established tension-compression splits could be applied straightforwardly. Applying Equation (6.3) and (6.4) to the functional (6.2), yields

$$\mathcal{F}[\mathbf{u}, \phi_c, \nabla\phi_c] = \int_{\Omega} \frac{1}{2} h(\phi_c) (\mathbb{C}[\boldsymbol{\varepsilon}] \cdot \boldsymbol{\varepsilon} + \frac{1}{2} G_c \left( \varepsilon_{\phi_c} |\nabla\phi_c|^2 + \frac{1}{\varepsilon_{\phi_c}} \phi_c^2 \right)) dv. \quad (6.6)$$

**Balance of linear momentum** Following the approach of Kuhn et al. [28], the minimization of the free energy functional (6.6), with respect to the displacement yields the balance of linear momentum

$$\operatorname{div}(h(\phi_c)\boldsymbol{\sigma}) = \mathbf{o}. \quad (6.7)$$

**Evolution equation** The evolution equation of the order parameter  $\phi_c$  can be described by an Allen-Cahn equation [89]

$$\varepsilon_{\phi_c} \dot{\phi}_c = -M \frac{\delta \mathcal{F}}{\delta \phi_c} = -M \left( \frac{\partial f(\mathbf{u}, \phi_c, \nabla \phi_c)}{\partial \phi_c} - \operatorname{div} \left( \frac{\partial f(\mathbf{u}, \phi_c, \nabla \phi_c)}{\partial \nabla \phi_c} \right) \right), \quad (6.8)$$

with a mobility parameter  $M \geq 0$ ,  $\nabla \phi_c \cdot \mathbf{n} = 0$  on  $\partial\Omega$  and the outer normal vector  $\mathbf{n}$  on the boundary.

**Analytical crack profile** For a one-dimensional stationary crack without mechanical loads, and thus with vanishing mechanical driving force, the evolution equation according to (6.8) is able to reproduce the correct surface energies of a sharp interface and leads to the analytical profile [29]

$$\phi_c(x) = \exp\left(-\frac{|x|}{\varepsilon_{\phi_c}}\right), \quad (6.9)$$

which is displayed in Figure 6.2a.

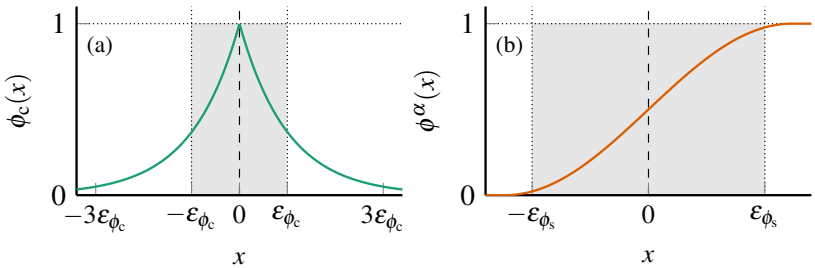


**Figure 6.2:** Analytical order parameter profile for crack (a) and solid (b), for a corresponding sharp crack and a solid-solid interface at  $x = 0$ , respectively.

**Irreversibility condition** Various approaches for the realization of an irreversibility condition for the evolution equation are listed in the literature: Bourdin et al. [27] used a Dirichlet boundary condition. In contrast, Miehe et al. [29] introduced a strain history function to realize the irreversibility of crack order parameter. More recent approaches use the augmented Lagrangian method [149], a primal-dual-active set [150], a complementarity system [151], or the interior point method [152]. The model introduced above reproduces the correct sharp interface energy in the case of the analytical profile (6.9). Since mechanical loads are considered here, the strain energy density contributes to the evolution equation of the order parameter (6.8). This leads to a distorted profile, if crack healing is prevented completely, and therefore to an error in the represented energy, if the applied load is removed completely. As the objective of this work is to investigate the possibility of different models to reproduce the sharp interface energies, the irreversibility is realized by a Dirichlet boundary condition, where the evolution equation is not restricted in general, but all fully damaged points remain damaged, using a boundary condition  $\phi_c = 1$ , where a point is assumed to be fully damaged by  $\phi_c \geq 0.99$  using a numerical threshold. This improves the numerical behavior and has a negligible effect on the results. Nevertheless, the models presented in the present work could also be realized with other approaches to the irreversibility condition, which are listed above.

### 6.1.2 Heterogeneous single-crack order parameter (SCOP) phase-field model

**Solid order parameters** To distinguish different regions of a heterogeneous body, the order parameters  $\phi^\alpha \in [0, 1], \forall \alpha = 1, \dots, N$  are introduced for  $N$  different regions, which can be arranged in the tuple

$$\phi = \{\phi^1, \phi^2, \dots, \phi^N\}. \quad (6.10)$$

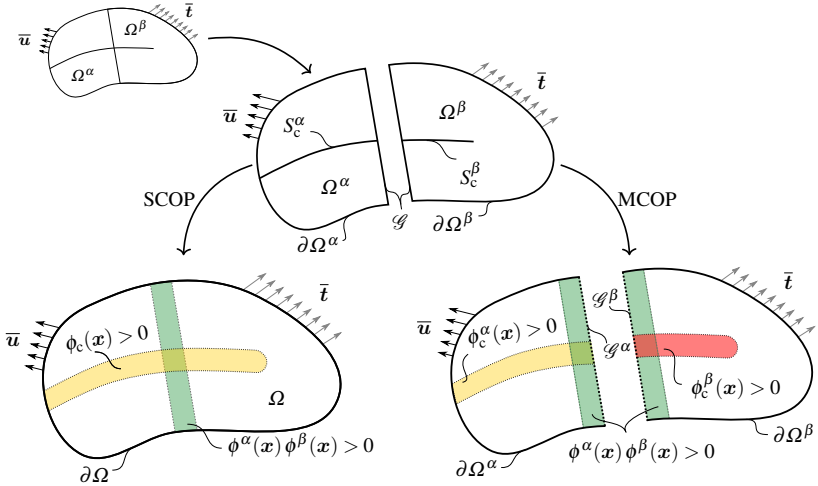


**Figure 6.3:** Schematic heterogeneous domain for the SCOP and MCOP models: The initial domain is schematically drawn on the top left. The subdomains are visualized separately in the center, with a sharp crack interface. In the lower left, the SCOP model is shown with its diffuse crack interfaces in yellow, whereas in the lower right, the MCOP model is displayed with several diffuse crack interfaces in the subdomains  $\Omega^\alpha$  and  $\Omega^\beta$  in red and yellow. The diffuse solid interface  $\phi^\alpha(\mathbf{x})\phi^\beta(\mathbf{x})$  is indicated in green.

A bulk region of phase  $\alpha$  is represented by  $\phi^\alpha = 1$ , while a diffuse interface is represented by  $0 < \phi^\alpha < 1$ . As the order parameters can be interpreted as the volume fraction of the corresponding regions, the condition

$$\sum_{\alpha=1}^N \phi^\alpha = 1 \quad (6.11)$$

has to be fulfilled. By extending the free energy functional (6.1) with interfacial terms between the regions, a multiphase-field model can be formulated as

proposed by Nestler et al. [46]. Using a double obstacle phase-field potential results in an analytical one-dimensional profile for a binary interface:

$$\phi^\alpha(x) = \frac{1}{2} \left( 1 + \sin \left( \frac{\pi}{l_s} x \right) \right), \quad -\frac{l_s}{2} \leq x \leq \frac{l_s}{2}, \quad (6.12)$$

as shown by Steinbach et al. [153], which is presented in Figure 6.2b. It is characterized by the interface width  $l_s$  or, analogous to the crack profile, by a length parameter  $\varepsilon_{\phi_s} = 4/\pi^2 l_s$ . Since no changes of  $\phi^\alpha$  are examined in this work, an extension of the free energy and a derivation of a classical multiphase-field is omitted. Instead, the analytical profile (6.12) is utilized to parameterize the domain, resulting in diffuse and smooth volumetric interfaces, cf. Figure 6.3.

**Free energy functional** To account for heterogeneous materials, the domain  $\Omega$  can be decomposed into subdomains  $\Omega^\alpha$  with constant material properties, cf. Figure 6.3. Thus, the energy functional for sharp interfaces follows by

$$\mathcal{F}[\mathbf{u}] = \sum_{\alpha}^N \int_{\Omega^\alpha} f_{\text{el}}^\alpha(\mathbf{u}) \, dv + \sum_{\alpha}^N \int_{S_c^\alpha} G_c^\alpha \, da. \quad (6.13)$$

In the context of the SCOP model, and thus, in contrast to the functional (6.1), the strain energy densities  $f_{\text{el}}^\alpha$  as well as the critical energy release rates  $G_c^\alpha$  are phase-specific, denoted by the phase index  $\alpha$ . The energy of each subdomain is given by an integral of energy densities over  $\Omega^\alpha$ , which can be parameterized using an indicator function and expanded to  $\Omega$ . Subsequently, the order parameters of the solid phase field can be used as a smooth approximation to the indicator function [154, 155]. This leads to a linear interpolation of the energy densities with the solid order parameters  $\phi$ , cf. for example Nestler et al. [46], yielding

$$\mathcal{F}[\mathbf{u}] = \int_{\Omega} \sum_{\alpha}^N \phi^\alpha f_{\text{el}}^\alpha(\mathbf{u}) \, dv + \int_{S_c} \sum_{\alpha}^N \phi^\alpha G_c^\alpha \, da. \quad (6.14)$$

As for the classic homogeneous model, a crack order parameter  $\phi_c$  is introduced to describe the damage of the domain smoothly, and the free energy of a heterogeneous body is given by

$$\begin{aligned} \mathcal{F}[\mathbf{u}, \phi_c, \nabla\phi_c] = & \int_{\Omega} h(\phi_c) \sum_{\alpha}^N \phi^{\alpha} f_{\text{el}}^{\alpha} \\ & + \frac{1}{2} \sum_{\alpha}^N \phi^{\alpha} G_c^{\alpha} \left( \varepsilon_{\phi_c} |\nabla\phi_c|^2 + \frac{1}{\varepsilon_{\phi_c}} \phi_c^2 \right) \text{d}v, \end{aligned} \quad (6.15)$$

$$f_{\text{el}}^{\alpha} = \frac{1}{2} \boldsymbol{\sigma}^{\alpha} \cdot \boldsymbol{\varepsilon}^{\alpha}, \quad \boldsymbol{\sigma}^{\alpha} = \mathbb{C}^{\alpha} [\boldsymbol{\varepsilon}^{\alpha}]. \quad (6.16)$$

In general, the phase-inherent stresses and strains are unknown. To determine an overall material behavior, further assumptions have to be made. This is widely investigated in the context of phase-field modeling [56–59, 61]. Recently, Prajapati et al. [47] introduced a model that applies the homogenization scheme proposed by Schneider et al. [61] in the context of a phase-field fracture model. Nevertheless, for simplicity, a Voigt-Taylor homogenization scheme is used in this work, assuming equal strains in each phase

$$\boldsymbol{\varepsilon}^{\alpha} = \boldsymbol{\varepsilon} \quad \forall \alpha = 1, \dots, N, \quad (6.17)$$

acknowledging the limited capabilities of this scheme [22, 58]. By applying (6.17) and (6.16) to the functional (6.15) this yields

$$\begin{aligned} \mathcal{F}[\mathbf{u}, \phi_c, \nabla\phi_c] = & \int_{\Omega} \frac{1}{2} h(\phi_c) \sum_{\alpha}^N \phi^{\alpha} (\mathbb{C}^{\alpha} [\boldsymbol{\varepsilon}]) \cdot \boldsymbol{\varepsilon} \\ & + \frac{1}{2} \sum_{\alpha}^N \phi^{\alpha} G_c^{\alpha} \left( \varepsilon_{\phi_c} |\nabla\phi_c|^2 + \frac{1}{\varepsilon_{\phi_c}} \phi_c^2 \right) \text{d}v. \end{aligned} \quad (6.18)$$

Note that the procedure to obtain the evolution equations of the crack order parameter and the balance of linear momentum is the same as for the classical phase-field crack propagation model in Section 6.1.1, but now including interpolations of the phase-specific stiffnesses and critical energy release rates with the order parameters  $\phi^\alpha$ .

### 6.1.3 Heterogeneous multi-crack order parameter (MCOP) phase-field model

**Order parameters** As in the previous section, a tuple of order parameters,

$$\phi = \{\phi^1, \phi^2, \dots, \phi^N\}, \quad \sum_{\alpha=1}^N \phi^\alpha = 1, \quad (6.19)$$

is introduced to parameterize different regions of a heterogeneous body. In addition, a tuple consisting of separate crack order parameters  $\phi_c^\alpha \in [0, 1]$ , for each solid phase,

$$\phi_c = \{\phi_c^1, \phi_c^2, \dots, \phi_c^N\}, \quad (6.20)$$

is introduced. Each crack order parameter  $\phi_c^\alpha$  tracks the damage of the corresponding solid region  $\alpha$ . For  $\phi_c^\alpha = 1$ , for instance, the complete volume fraction  $\phi^\alpha$  is damaged, while other solid regions are not affected by  $\phi_c^\alpha$ , cf. Figure 6.3.

**Free energy functional** The MCOP model combines the functional given by Equation (6.14), used as the basis for the SCOP model, with the individual degradation of the strain energy densities  $f_{el}^\alpha$  by means of multiple crack order parameters according to Equation (6.20). In addition, the critical energy release

rates  $G_c^\alpha$  are also parameterized by the individual crack order parameters. This results in the free energy functional

$$\begin{aligned} \mathcal{F}[\mathbf{u}, \phi_c, \nabla \phi_c] &= \int_{\Omega} \sum_{\alpha}^N \phi^\alpha h(\phi_c^\alpha) f_{\text{el}}^\alpha \\ &\quad + \frac{1}{2} \sum_{\alpha}^N \phi^\alpha G_c^\alpha \left( \varepsilon_{\phi_c} |\nabla \phi_c^\alpha|^2 + \frac{1}{\varepsilon_{\phi_c}} (\phi_c^\alpha)^2 \right) \text{d}v, \end{aligned} \quad (6.21)$$

with  $\nabla \phi_c = \{\nabla \phi_c^1, \nabla \phi_c^2, \dots, \nabla \phi_c^N\}$ . The free energy functional for each subdomain  $\Omega^\alpha$  can be identified by

$$\begin{aligned} \mathcal{F}^\alpha[\mathbf{u}, \phi_c^\alpha, \nabla \phi_c^\alpha] &= \int_{\Omega} \phi^\alpha f^\alpha(\mathbf{u}, \phi_c^\alpha, \nabla \phi_c^\alpha) \text{d}v \\ &= \int_{\Omega^\alpha} \underbrace{h(\phi_c^\alpha) f_{\text{el}}^\alpha + \frac{1}{2} G_c^\alpha \left( \varepsilon_{\phi_c} |\nabla \phi_c^\alpha|^2 + \frac{1}{\varepsilon_{\phi_c}} (\phi_c^\alpha)^2 \right)}_{f^\alpha(\mathbf{u}, \phi_c^\alpha, \nabla \phi_c^\alpha)} \text{d}v. \end{aligned} \quad (6.22)$$

With Equation (6.16) and, as in the previous model, the assumption of the Voigt-Taylor scheme (6.17), the functional for the whole domain and each subdomain is obtained by

$$\begin{aligned} \mathcal{F}^\alpha[\mathbf{u}, \phi_c^\alpha, \nabla \phi_c^\alpha] &= \int_{\Omega^\alpha} \frac{1}{2} h(\phi_c^\alpha) (\mathbb{C}^\alpha [\boldsymbol{\varepsilon}]) \cdot \boldsymbol{\varepsilon} \\ &\quad + \frac{1}{2} G_c^\alpha \left( \varepsilon_{\phi_c} |\nabla \phi_c^\alpha|^2 + \frac{1}{\varepsilon_{\phi_c}} (\phi_c^\alpha)^2 \right) \text{d}v, \end{aligned} \quad (6.23)$$

$$\begin{aligned} \mathcal{F}[\mathbf{u}, \phi_c, \nabla \phi_c] &= \int_{\Omega} \frac{1}{2} \sum_{\alpha=1}^N \phi^\alpha h(\phi_c^\alpha) (\mathbb{C}^\alpha [\boldsymbol{\varepsilon}]) \cdot \boldsymbol{\varepsilon} \\ &\quad + \frac{1}{2} \sum_{\alpha=1}^N \phi^\alpha G_c^\alpha \left( \varepsilon_{\phi_c} |\nabla \phi_c^\alpha|^2 + \frac{1}{\varepsilon_{\phi_c}} (\phi_c^\alpha)^2 \right) \text{d}v. \end{aligned} \quad (6.24)$$

As in the previous models, minimizing the latter functional with respect to the displacements yields the balance of linear momentum and is therefore omitted here.

**Evolution equation** For each crack order parameter an Allen-Cahn equation,

$$\begin{aligned} \varepsilon_{\phi_c} \dot{\phi}_c^\alpha &= -M^\alpha \frac{\delta \mathcal{F}^\alpha}{\delta \phi_c^\alpha} \\ &= -M^\alpha \left( \frac{\partial f^\alpha(\mathbf{u}, \phi_c^\alpha, \nabla \phi_c^\alpha)}{\partial \phi_c^\alpha} - \operatorname{div} \left( \frac{\partial f^\alpha(\mathbf{u}, \phi_c^\alpha, \nabla \phi_c^\alpha)}{\partial \nabla \phi_c^\alpha} \right) \right), \end{aligned} \quad (6.25)$$

with a mobility  $M^\alpha \geq 0$  is postulated. These evolution equations are defined on the subdomains  $\Omega^\alpha$ , whereas on the boundary  $\partial\Omega^\alpha$  a homogeneous Neumann boundary condition with  $\nabla \phi_c^\alpha \cdot \mathbf{n} = 0$  applies. In contrast, the boundary  $\mathcal{G}^\alpha$ , resulting from the smooth transition of  $\mathcal{G}$  (cf. Figure 6.3), has to be treated separately. Neither a classical Neumann nor a Dirichlet boundary condition is a reasonable choice. A Neumann boundary condition would enforce a certain flux across the boundary. For example, a zero flux would result in a crack propagation direction perpendicular to the boundary. A Dirichlet boundary condition, on the other hand, would constrain the order parameter  $\phi_c^\alpha$  and thus the crack propagation. More complex boundary conditions, such as absorbing boundary conditions, or Robin type boundary conditions, could constitute more physical boundary conditions. Since these are neither widely used nor trivial to implement, an alternative approach is proposed: The evolution equation is extended to the whole domain  $\Omega$ , but the elastic driving force is restricted to  $\Omega^\alpha$ , and considered to vanish anywhere else. This results in a continuous calculation of the crack order parameters, not restricted to the inner boundary, each with similar terms, as in the homogeneous model, but with phase-specific quantities. Outside the subdomain  $\Omega^\alpha$ , the phasefield is continued in the sense of the exponential profile (6.9), reproducing the correct sharp interface energy in a diffuse context. The coupling of these different equations takes place solely through the interpolation of the strain energy density. In addition, an irreversibility

condition for each evolution equation is used: As in Section 6.1.1, each crack order parameter is kept damaged by means of the additional constraint  $\phi_c^\alpha = 1$ , if  $\phi_c^\alpha \geq 0.99$ .

## 6.1.4 Comparison

**Classic homogeneous model** Section 6.1.1 introduced a crack propagation model based on established models from the literature. Many extensions and modifications to such a model can be found in the literature, which can improve the model for many applications [48, 50, 148]. Nevertheless, such extensions are avoided intentionally, reducing the complexity, as the model is used as the basis for the introduced heterogeneous SCOP and MCOP models. In the scope of this work, no implementation of the classical model is conducted. While the limitations of the classical model are acknowledged, many of the established modifications might also be applied to the novel MCOP model, while retaining the advantages of this approach. Nevertheless, the classical model could be extended to heterogeneous systems, e.g. based on element-wise constant material properties in the context of the FEM. On the other hand, the SCOP model with the limit of a sharp interface would yield the same results.

**Single-crack order parameter (SCOP) models** The SCOP model, introduced in Section 6.1.2, is similar to models from the literature [22, 47, 48]. However, there are some differences:

- Schneider et al. [22] introduced the order parameters  $\phi^\alpha$  and the crack order parameter  $\phi_c$  in the same tuple  $\phi$ . Therefore,  $\phi_c$  also contributes to the summation condition (6.11). This results in a model where the phases show transitions to a common crack phase. In addition, the interpolation function  $h(\phi_c)$  must then normalize with respect to  $\sum_\alpha^N \phi^\alpha$ , while the crack energy is also considered in the evaluation equation of the phases, and vice versa.

- Prajapati et al. [47] and Späth et al. [48] used a similar approach as Schneider et al. [22], but the crack evolution equation is assumed to be independent of the order parameters  $\phi^\alpha$ , and is solely used to determine effective material properties.
- In this work, the order parameters  $\phi^\alpha$  and the crack order parameter  $\phi_c$  are introduced separately, and the damage of all phases is represented by  $\phi_c$ , but without any phase transitions from these to the crack phase. This results in a model similar to Prajapati et al. [47] or Späth et al. [48], but without requiring a normalization of the interpolation function.
- Due to the similarities to established models, the SCOP model is used as a reference model in the following 2D examples.

<p>SCOP :</p> $0 = \operatorname{div} \left( h(\phi_c) \sum_{\alpha}^N \phi^\alpha \boldsymbol{\sigma}^\alpha \right),$ $\dot{\phi}_c \frac{1}{M} = \sum_{\alpha}^N \phi^\alpha G_c^\alpha \left( \Delta \phi_c - \frac{1}{\varepsilon_{\phi_c}^2} \phi_c \right) + \sum_{\alpha}^N G_c^\alpha \nabla \phi^\alpha \cdot \nabla \phi_c - \frac{1}{\varepsilon_{\phi_c}} \frac{\partial h(\phi_c)}{\partial \phi_c} \sum_{\alpha}^N \phi^\alpha f_{el}^\alpha$ <p>MCOP :</p> $0 = \operatorname{div} \left( \sum_{\alpha}^N h(\phi_c^\alpha) \phi^\alpha \boldsymbol{\sigma}^\alpha \right),$ $\dot{\phi}_c^\alpha \frac{1}{M^\alpha} = G_c^\alpha \left( \Delta \phi_c^\alpha - \frac{1}{\varepsilon_{\phi_c}^2} \phi_c^\alpha \right) - \frac{1}{\varepsilon_{\phi_c}} \frac{\partial h(\phi_c^\alpha)}{\partial \phi_c^\alpha} f_{el}^\alpha, \quad \forall \alpha = 1, \dots, N$
--

**Table 6.1:** Comparison of the terms in the balance of linear momentum and the evolution equation of the SCOP and MCOP model<sup>2</sup>.  $\Delta \cdot$  denotes the Laplacian operator.

<sup>2</sup>An error in the derivation from Schöller et al. [1] has been corrected in this work.

**SCOP vs MCOP model** Both models introduce a tuple of order parameters for the parametrization of the domain, thereby accounting for the heterogeneity of the body. The differences between both models are summarized in the following.

- *SCOP model*: Only a single crack order parameter is considered. Thus, all regions are equally damaged. Both, the balance of linear momentum as well as the evolution equation of the crack order parameter are obtained by minimization of the functional  $\mathcal{F}$  with respect to the total domain  $\Omega$ .
- *MCOP model*: A tuple of crack order parameters is introduced. Thus, the damage of a region is described by its own order parameter, which allows a more advanced degradation of the strain energy. Moreover, functionals  $\mathcal{F}^\alpha$  are introduced on subdomains  $\Omega^\alpha$ . As for the SCOP model, the balance of linear momentum is obtained by the minimization of the total functional with respect to the total domain. However, the evolution equations of the crack order parameter are obtained by the minimization of the functionals  $\mathcal{F}^\alpha$  with respect to the domain  $\Omega^\alpha$  of the corresponding crack order parameter. Each evolution equation also recovers the classic model, while maintaining a constant crack surface energy and many of the advantages of this model.

Furthermore, the differences in the evolution equations and linear momentum balances are summarized in Table 6.1.

## 6.2 Numerical treatment<sup>3</sup>

**Influence of the crack length parameter  $\varepsilon_{\phi_c}$**  Regarding phase-field crack models for simulations, it has been repeatedly shown that the length parameter used to determining the width of the diffuse transition between damaged material points and undamaged material points has an effect on the simulation results, see [28, 29, 48], for example. This is especially true when considering crack initiation processes, for which often  $\varepsilon_{\phi_c}$  is treated as material property, cf., e.g. Tanné et al. [156]. Recently, Kumar et al. [157] discussed crack nucleation in the context of phase-field modeling and promoted an alternative approach for nucleation treatment. If initial cracks exist and the transition width is compatible with the discretization grid and the domain size, the influence of  $\varepsilon_{\phi_c}$  is not significant [156, 158–160]. This difficulty was extensively studied in [161], and it was concluded that the length parameter should be considered as a material property that depends on the tensile strength of a material. Tanné et al. [156] derived a possible solution for the correct determination of the length parameter. However, if the length parameter is considered as a material property, especially on small length scales, this often leads to difficulties, as the compatibility between the length parameter, the discretization grid, and the domain size is no longer guaranteed. To eliminate this sensitivity, Wu et al. [162] introduced an approach for brittle materials. Since the presented model is a completely new interpretation of the regularized crack problem, the approach by Wu et al.’s is not considered, to reduce complexity. For a clear presentation of the new model, the disadvantages and the problem of the dependence of the simulation results on the length parameter are acknowledged but not taken into account. However, improving the model towards parameter insensitivity is nevertheless straight forward with the approach published in Wu et al. [162].

---

<sup>3</sup>The content of this section has been taken directly from Schöllner et al. [1] with minor linguistic changes.

**Algorithm 2:** Staggered scheme for SCOP

---

```

initialize  $\phi_c$ 
initialize boundary condition
 $t \leftarrow t_0$ 
while  $t < t_{\text{end}}$  do
  loop
    solve lin. momentum balance
    // cf. Table 6.1
    solve evolution eq. for  $\phi_c$  // cf.
    Table 6.1
     $\phi_c \leftarrow \phi_c + \Delta t \dot{\phi}_c$ 
    adapt mesh
     $static \leftarrow |\dot{\phi}_c|_{\infty} < \varepsilon_{\phi_c}$ 
    if  $static$  then
       $t \leftarrow t + \Delta t$ 
      increment boundary
      condition
      break
    end
  end
end

```

---

**Algorithm 3:** Staggered scheme for MCOP

---

```

initialize  $\phi_c \quad \forall \alpha = 1, \dots, N$ 
initialize boundary condition
 $t \leftarrow t_0$ 
while  $t < t_{\text{end}}$  do
  loop
    solve lin. momentum balance
    // cf. Table 6.1
    for  $\alpha = 1$  to  $N$  do
      solve evolution eq. for  $\phi_c^\alpha$ 
      // cf. Table 6.1
       $\phi_c^\alpha \leftarrow \phi_c^\alpha + \Delta t \dot{\phi}_c^\alpha$ 
    end
    adapt mesh
     $static \leftarrow \max_{\alpha=1, \dots, N} |\dot{\phi}_c^\alpha|_{\infty} < \varepsilon_{\phi_c}$ 
    if  $static$  then
       $t \leftarrow t + \Delta t$ 
      increment boundary
      condition
      break
    end
  end
end

```

---

**Numerical discretization** The proposed models result in a system of partial differential equations, consisting of the balance of linear momentum and multiple evolution equations for the crack order parameters. In this work the staggered approach of Miehe et al. [29] is used, which is based on a operator split. Each partial differential equation is solved by assuming the other fields constant. Together with a time stepping scheme

$$\phi_c^{n+1} = \phi_c^n + \Delta t \dot{\phi}_c, \quad \phi_c^{\alpha, n+1} = \phi_c^{\alpha, n} + \Delta t \dot{\phi}_c^\alpha, \quad (6.26)$$

and a time step  $\Delta t$ , this results in linear partial differential equations. The index  $n$  denotes the order parameters for an old time step, while  $n + 1$  denotes the order parameter for a new time step.

In order to ensure a quasi-static crack propagation, the steady state conditions

$$|\dot{\phi}_c|_\infty < e_{\phi_c}, \quad |\dot{\phi}_c^\alpha|_\infty < e_{\phi_c} \quad (6.27)$$

are introduced, with the infinity norm  $|\cdot|_\infty$  and a tolerance parameter  $e_{\phi_c} = 10^{-4}$ . After solving the individual equations in each iteration, the condition is evaluated. Only if the condition is fulfilled, the system will progress further in time. As a consequence there is an inner iteration loop, which solves each equation subsequently, until a steady state is reached, and an outer loop, which can be associated with a physical time and a time-dependent load, using boundary conditions. The procedure corresponding to this approach is illustrated as pseudocode in Algorithm 2 for the SCOP model and compared to the MCOP model (Algorithm 3). The mobilities  $M$  and  $M^\alpha$  also reduce to numerical parameters and will not influence the results within a certain reasonable numerical range. In addition, an exemplary study of the evolution of these staggered systems and their iterations is conducted in A.3. In order to solve the partial differential equations, a FEM approach, based on the C++ finite element library DEAL.II [163], is used<sup>4</sup>. In this work, first-order Lagrange finite elements and a second-order Gauss-Legendre quadrature rule for numerical integration are used. The evolution equations are solved using an implicit time stepping procedure (cf. Equation (6.26)), except for the elastic driving force term, which is considered explicitly in time. Adaptive mesh refinement (AMR) is used to reduce the computational effort. Especially for the setup chosen in section 6.4.2, big domains are required which are computationally unfeasible on a uniform mesh. In this work a basic AMR strategy is used, and the reader is referred to, for example, Heister et al. [150] for a more state-of-the-art AMR approach. The strategy of our current approach uses different criteria for refinement or coarsening for the evolution equation and the equilibrium of the linear momentum. Based on the gradient of the order parameter or strain energy density and the extent of the elements, discrete changes are calculated for each element. If

---

<sup>4</sup>Results taken from Schöllner et al. [1, 3] were conducted based on DEAL.II, and all additional phase-field simulation studies used an implementation in the PACE3D framework [164].

certain values are exceeded or undershot, the element is refined, or coarsened, respectively. In addition, this procedure is explicitly evaluated in time. Despite limitations of the strategy acknowledged, it enables the computation of bigger domains. Combined with a very conservative refinement controlled by the values for refinement and coarsening, and frequent execution, the strategy has proven its robustness. However, this has the disadvantage of low computational optimization compared to more advanced approaches such as those of Heister et al. [150]. Nevertheless, it provides huge improvements over a uniform mesh.

**Residual stiffness** For a FEM approach, an interpolation function  $h(\phi_s)$ , which will be zero for a fully broken state, will result in a singular stiffness and an ill-posed problem. This can be avoided by replacing the degradation function by

$$\tilde{h}(\phi_c) = \begin{cases} h(\phi_c) & 1 - \phi_c > \phi_s^{\text{th}}, \\ h(\phi_c^{\text{th}}) & \text{else,} \end{cases} \quad (6.28)$$

with a threshold value  $\phi_s^{\text{th}} = 10^{-4}$ . This function will preserve a certain value and even ensures a residual stiffness even for completely damaged regions.

## 6.3 Extension to a single-obstacle potential

So far, only a phase-field crack propagation models based on a quadratic potential term have been introduced. In the context of the classical phase-field models, this is often referred to as the single-well potential, or in the context of the mechanical community as the *AT2* model, cf. e.g [156]. An alternative

formulation used the single-obstacle potential, leading to the *ATI* model. The free energy for the SCOP model follows with

$$\begin{aligned} \mathcal{F}[\mathbf{u}, \phi_c, \nabla \phi_c] &= \int_{\Omega} h(\phi_c) \sum_{\alpha}^N \phi^{\alpha} f_{\text{el}}^{\alpha} \\ &+ \frac{1}{2} \sum_{\alpha}^N \phi^{\alpha} G_c^{\alpha} \left( \varepsilon_{\phi_c} |\nabla \phi_c|^2 + \frac{9}{16\varepsilon_{\phi_c}} \phi_c \right) dv, \end{aligned} \quad (6.29)$$

where the prefactor 9/16 ensures the representation of the corrected surface energy of a corresponding sharp crack surface. Analogously, the free energy for the MCOP model can be rewritten as

$$\begin{aligned} \mathcal{F}^{\alpha}[\mathbf{u}, \phi_c^{\alpha}, \nabla \phi_c^{\alpha}] &= \int_{\Omega^{\alpha}} h(\phi_c^{\alpha}) f_{\text{el}}^{\alpha} \\ &+ \frac{1}{2} G_c^{\alpha} \left( \varepsilon_{\phi_c} |\nabla \phi_c^{\alpha}|^2 + \frac{9}{16\varepsilon_{\phi_c}} \phi_c^{\alpha} \right) dv. \end{aligned} \quad (6.30)$$

Note that the use of a single-obstacle potential leads to a constant term in the evolution equation. To ensure that  $\phi_c, \phi_c^{\alpha} \in [0, 1] \forall \alpha = 1, \dots, N$ , further techniques such as the active set method or the augmented Lagrangian method, cf. e.g [149, 150], have to be used. However, the single-obstacle variant has some advantages. Since the derivation of the potential term does not vanish for zero damage, the analytical profile has a finite width. Together with the well-defined obstacle against initial crack growth, this leads to more localized crack growth and avoids damaged materials even far away from the crack tip.

In the following work, both the single-well and the single-obstacle variants will be used. Since the single-well potential is well established in the literature, most of the basic investigations will be performed based on it, if not stated otherwise. Subsequently, e.g., some applications to FRPs will also be performed with both models or, due to the numerical advantages, only with the single-obstacle model.

## 6.4 Results

**Effective crack order parameters**<sup>5</sup> In order to be able to compare the results of the SCOP and MCOP model, additional effective order parameters are introduced. An order parameter  $\phi^\alpha$  can be decomposed into an effectively damaged part  $\tilde{\phi}_c^\alpha$  and an effectively undamaged part  $\tilde{\phi}_s^\alpha$ :

$$\phi^\alpha = \tilde{\phi}_c^\alpha + \tilde{\phi}_s^\alpha. \quad (6.31)$$

Each of these parts is defined using the individual crack order parameters of the MCOP model

$$\tilde{\phi}_c^\alpha = \phi^\alpha \phi_c^\alpha, \quad \tilde{\phi}_s^\alpha = \phi^\alpha (1 - \phi_c^\alpha). \quad (6.32)$$

Also a totally effective crack order parameter is formulated:

$$\tilde{\phi}_c = \sum_{\alpha=1}^N \tilde{\phi}_c^\alpha. \quad (6.33)$$

Note that these effective quantities describe the damaged and the undamaged fraction with respect to  $\sum_{\alpha}^N \phi^\alpha = 1$ , which is in contrast to  $\phi_c^\alpha$ , which only describes the ratio of damage with respect to  $\phi^\alpha$ .

### 6.4.1 Steady-state profiles in 1D<sup>5</sup>

To illustrate the difficulties of the heterogeneous SCOP model, steady-state profiles are examined for different model parameters and compared to the analytical solution. For the sake of simplicity, the system is assumed as binary and one-dimensional, while no mechanical loads are considered. Instead, a completely damaged point, in the middle of the domain, is placed and imposed

---

<sup>5</sup>The content of this section has been taken directly from Schöller et al. [1] with minor linguistic changes.

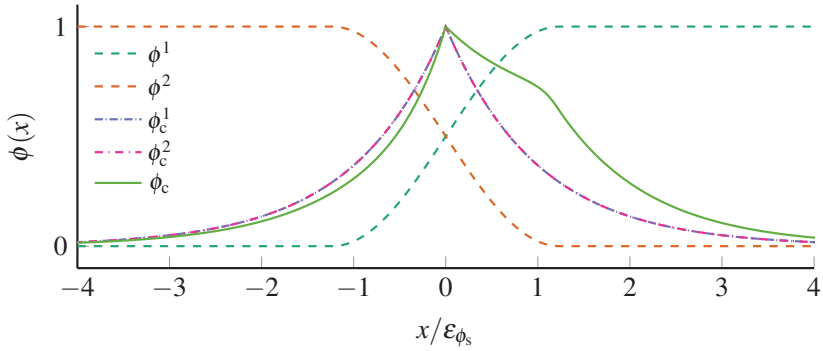


**Figure 6.4:** Steady state profiles for a diffuse interface at  $x = 0$ , with  $G_c^2/G_c^1 = 100$  and  $\epsilon_{\phi_c} = \epsilon_{\phi_s}$ .

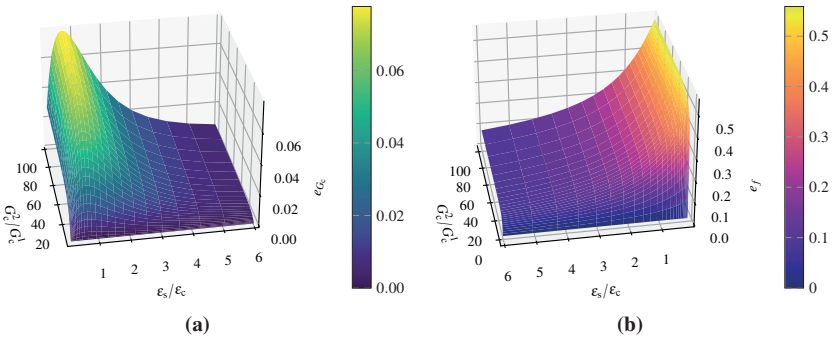


**Figure 6.5:** (a) Error of the total crack energies  $e_{G_c}$ . (b) Maximum of the local error of the energy density  $e_f$  (b) and a diffuse interface with varying model parameters.

via the boundary condition  $\phi_c = 1$  or  $\phi_c^\alpha = 1$ , respectively. In addition, an interface with different critical energy release rates for both materials is also placed in the middle of the domain. In Figure 6.4, exemplary steady-state profiles  $\phi_c$ , for the SCOP model, and  $\phi_c^\alpha$ , for the MCOP model, are shown along with the imposed interface. Note that a high contrast of the crack surface energies  $G_c^2/G_c^1 = 100$  and the same length parameters  $\varepsilon_{\phi_c} = \varepsilon_{\phi_s}$  are chosen. This results in a highly distorted profile for the SCOP model, compared to the analytical profile, due to the additional spatial gradient in  $\sum_\alpha^N \phi^\alpha G_c^\alpha$ . In contrast, the evolution equations of the MCOP model are independent, as the coupling is modeled purely by the degradation of the strain energy density, which is not present here. Together with the constant  $G_c^\alpha$ , this will avoid any distortions, and the analytical profile is reproduced.

The distorted profiles result in different energy densities and do not yield the analytically desired crack surface energy  $G_c^* = 1/2 (G_c^1 + G_c^2)$  when integrated over the domain. For the investigation of these deviations in the total energy, the error estimator deviation

$$e_{G_c} = \left| \frac{\mathcal{F} - G_c^*}{G_c^*} \right| \quad (6.34)$$

is introduced. For varying ratios of the critical energy release rates and interface widths, the deviations are displayed in Figure 6.5a. Due to the higher spatial gradient in the critical energy release rate, an increasing deviation for a higher contrast  $G_c^2/G_c^1$ , can be observed. For  $\varepsilon_{\phi_s} \gg \varepsilon_{\phi_c}$ , the change of the critical energy release rate is distributed over a larger physical width, leading to lower spatial gradients and lower deviations. If the case  $\varepsilon_{\phi_s} \ll \varepsilon_{\phi_c}$  is considered, the spatial gradient increases, but its influence is limited to only a part of the crack interface, resulting in a relatively low deviation for the total energy of the system. From a numerical point of view,  $\varepsilon_{\phi_s} \approx \varepsilon_{\phi_c}$  is desired to reduce the effort of resolving both interfaces. In this case, however the deviation is rather high. The deviations shown here do not exceed  $\approx 7.8\%$ , which seems

tolerable. Nevertheless, the maximum local deviation of the energy density can be defined by

$$e_f = \frac{|f - f^*|}{f} \Bigg|_{x=x_{\max}}, \quad (6.35)$$

with the analytical energy density  $f^*$ , defined by the analytical profile, and is evaluated at  $x_{\max}$ , for which the absolute difference of the density is highest. For the various parameters, this local deviations is shown in Figure 6.5b, which also shows an increasing deviation with higher  $G_c^2/G_c^1$ . With increasing  $\varepsilon_{\phi_s}/\varepsilon_{\phi_c}$ , the spatial gradient in  $\sum_{\alpha}^N \phi^{\alpha} G_c^{\alpha}$  becomes more local, which also increase the deviations. For the MCOP model, the error quantities  $e_{G_c}$  and  $e_f$  will vanish, as the profiles are identical to the analytical ones and will reproduce the correct crack surface energy  $G_c^*$ .

Although a high contrast in the surface energies only produces moderate deviations in the total energy, the local deviations of the energy density is an order of magnitude higher. So far, no crack propagation behavior has been considered. However, it is expected that the inability of the SCOP model to reproduce the energy density and total crack surface energy will also influence the evolution of the crack, which will be investigated in the subsequent sections.

## 6.4.2 Sloped binary interface<sup>6</sup>

This section follows the investigations by Henry [55]. Along with a binary interface, an initial crack is placed in a two-dimensional rectangular domain, with an angle  $\varphi$  between them, cf. Figure 6.6. Note that the real size of the domain is large, compared to the interface widths, to avoid any influence from the boundaries.

---

<sup>6</sup>The content of this section has been taken directly from Schöller et al. [1] with minor linguistic changes.

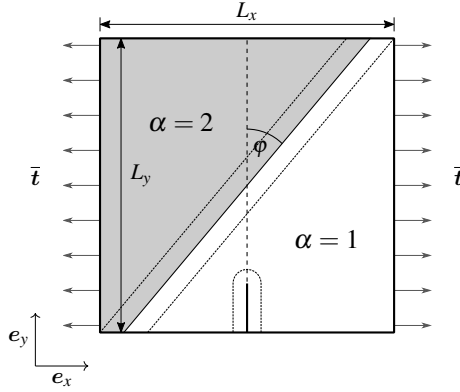


**Figure 6.6:** Exemplary structure of an inclined interface, with an angle  $\varphi$  between the binary interface and the initial crack. A time-dependent stress is applied on the left and right boundary.

In order to reduce complexity and avoid any influence of the chosen homogenization scheme, the elastic material behavior of both regions is assumed to be equal and isotropic with  $\lambda^1 = \lambda^2$ ,  $\mu^1 = \mu^2$ . In his work, Henry imposed displacement boundary conditions, but in order to use the LEFM theory in the present work, stress boundary conditions are employed to apply an initial mode I crack opening. For a straight crack the stress intensity factor results from

$$K_I = A\sigma\sqrt{a}, \quad (6.36)$$

with the generally unknown prefactor  $A$ , the crack length  $a$ , and the stress  $\sigma$ , far away from the crack, which hence is associated with the stress vector  $\bar{t}$  of the boundary condition, cf. Figure 6.6. If the stress is increased monotonously, this results in crack propagation above a critical stress, followed by an unstable crack growth. To be able to investigate the behavior of the crack propagation models, a quasi static crack growth with  $K_I = K_{Ic}$  is desirable for a constant critical value  $K_{Ic}$ . To obtain such a stable crack growth, the applied stress will be increased after each time step. If the crack propagates, measured by an enlargement of the domain,  $\phi_c = 1$  holds, the stress at the boundaries is reduced

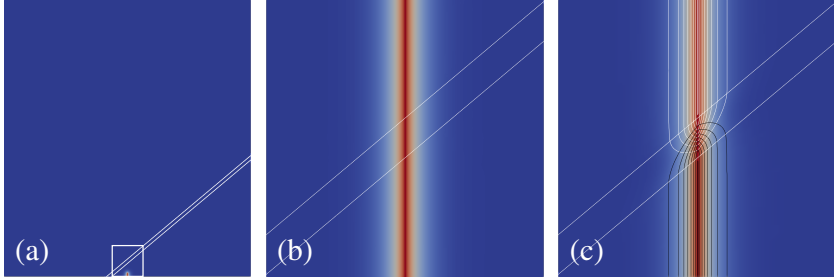


**Figure 6.7:** Simulation domain with an initial crack and a marked and enlarged artificial interface region (a). The crack order parameter  $\phi_c$  for the SCOP model (b) and  $\tilde{\phi}_c$  for the MCOP model (c), with contour lines for  $\tilde{\phi}_c^1$  and  $\tilde{\phi}_c^2$ . In addition, the solid boundaries of the interface are shown.

below an estimated new critical value, which is based on the crack growth  $\Delta a$ . Furthermore, the stress increment for each time step is also reduced. This approach aims to achieve linear crack growth over time and avoid unstable crack growth.

**Artificial interface** Firstly, the interface between the region is considered as artificial. Hence, the crack resistance is assumed to be equal,  $G_c^1 = G_c^2$ , together with the same stiffness, both regions can be considered to consist of the same material. The ratio of the interface width parameter of the solid and the crack is  $\varepsilon_{\phi_c}/l_s = 2/5$ , and for the interface angle,  $\varphi = 50^\circ$  is chosen. The results after simulating a mode I crack propagation of such a system are shown in Figure 6.7: It could be observed that the initial crack propagated straight through the domain, despite the presence of the interface. For the MCOP model, contour lines of the effective parts  $\tilde{\phi}_c^1$  and  $\tilde{\phi}_c^2$  are displayed, additionally. In the solid interface, the crack is transferred from one region to another, continuing the total effective crack, consisting of the sum of  $\tilde{\phi}_c^\alpha$ . The resulting effective crack  $\tilde{\phi}_c$  of the MCOP model is comparable to  $\phi_c$  of the SCOP model. In Figure 6.8a, the temporal evolution of the crack length  $a$ , normalized by the initial crack length  $a_0$ , is plotted against the normalized simulation time. Here, both

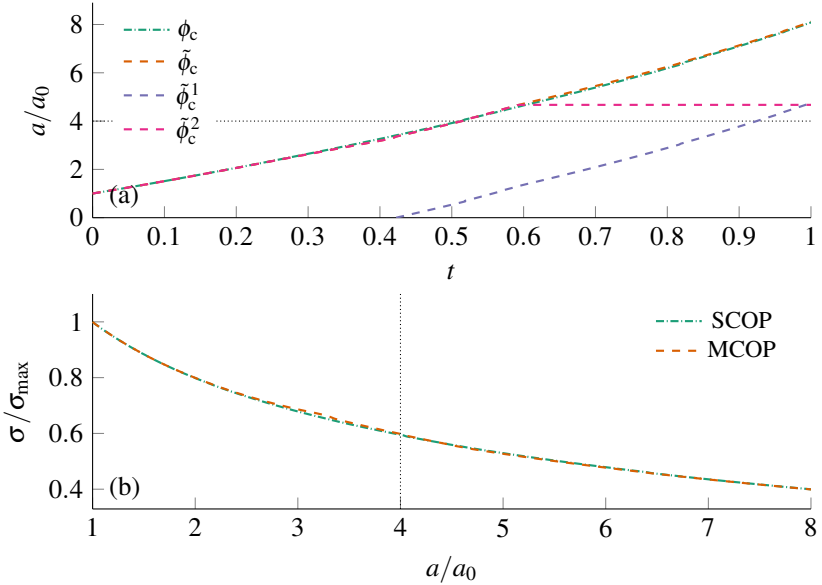


**Figure 6.8:** Normalized temporal evolution of the crack length (a), and the stress at the boundary, applied against the crack length (b), for the SCOP and MCOP model with  $\theta = 50^\circ$ .

models also showed the same effective behavior, and the transfer of the crack propagation, from one crack order parameter  $\phi_c^\alpha$  to the other, can be observed. The evolution of the applied stress  $\sigma$ , normalized by the critical stress to propagate the initial crack  $\sigma_0$ , is displayed in Figure 6.8b. Because of the way the boundary condition is applied, it should be noted that only the time step is shown in which the crack grows, while the other steps are omitted. The models show similar profiles and coincide with the expected profile from LEFM, cf. Equation (6.36). Regardless of the use of multiple crack order parameters, the novel MCOP model is able to reproduce the crack path and kinetics of the SCOP model. Furthermore, the presented approach ensures quasi-static crack growth and produces an almost linear crack growth over time, as well as the desired relation between applied stress and crack length.

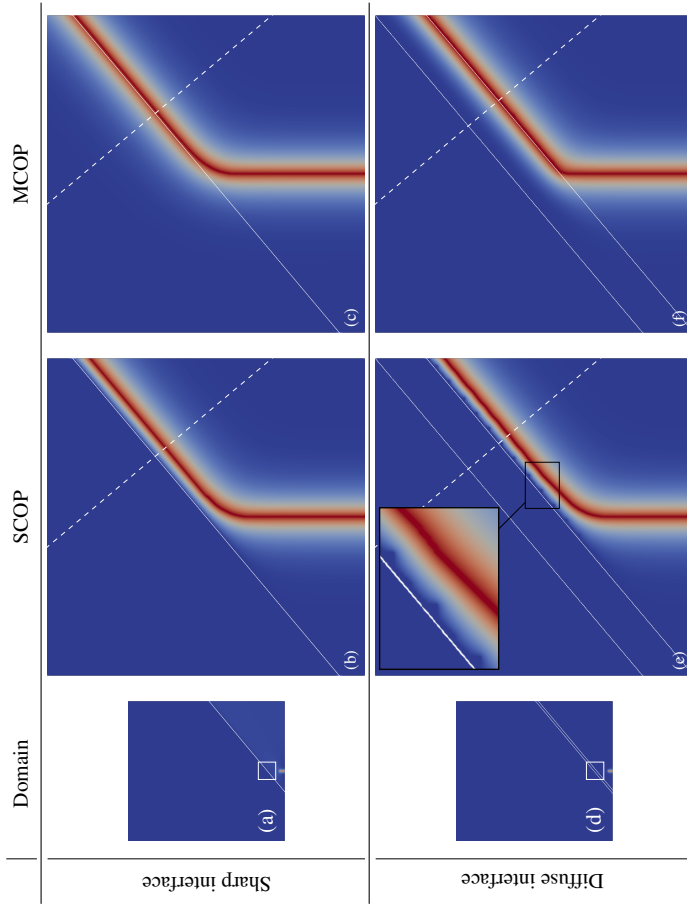


**Figure 6.9:** Crack propagation along the sloped interface, for sharp and diffuse interfaces: Simulation domain with an initial crack and a marked and enlarged interface region (a,d). The crack order parameter  $\phi_c$  and  $\phi_c$  for the MCOP model (b,e) and  $\phi_c$  for the SCOP model (c,f), after the crack propagated along the infinitely tough interface. In addition, the solid boundaries of the interface and the cross-section of Figure 6.10 are shown.

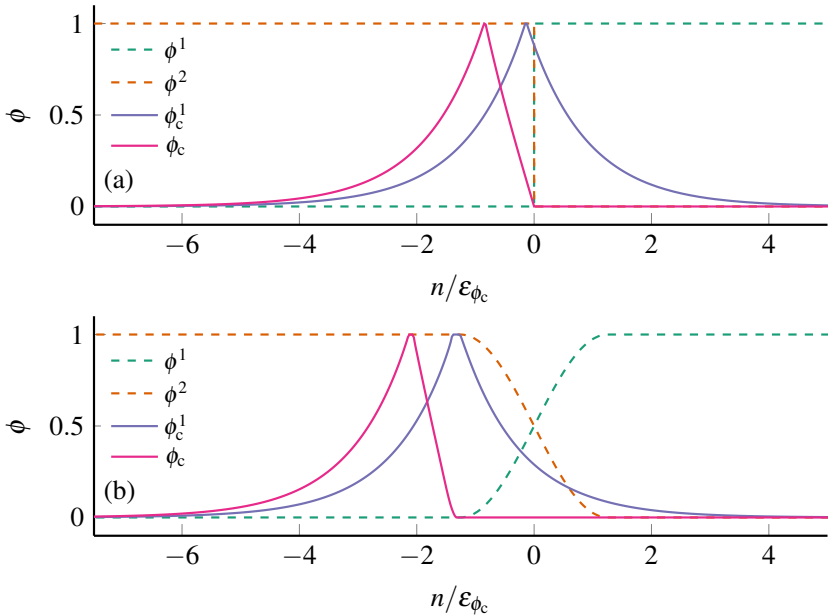


**Figure 6.10:** Cross-section with the underlying solid interface, along the binary interface of the SCOP and MCOP model, shown in Figure 6.9, for a sharp (a) and diffuse interface (b).

**Infinitely tough region** The other limiting case of crack propagation with a binary interface is an infinitely tough interface, which can be obtained when  $G_c^2 = \infty$ , which ensures that the upper region cannot be damaged at all and enforces the crack to grow along the interface. For both regions, the same stiffness parameters are used, while the boundary condition is applied as before.

In Figure 6.9, the crack path for both heterogeneous models and  $\varphi = 50^\circ$  are shown, considering both a sharp solid interface (a-c) and a diffuse solid interface (d-f). The marked cross section is also drawn in Figure 6.10 along with the solid interface. The SCOP model shows a non-physical behavior in some aspects:

- Due to the interpolation of the individual critical energy release rates  $G_c^\alpha$  and the infinitely tough upper region, no crack can occur there or in the interface region. This constrains the crack propagation in such a way that the crack is deflected before it reaches the solid interface.
- This interpolation also causes problems as to how the crack grows along the interface. Because the order parameter in the interface must be zero, this leads to a certain distance of the crack from the interface.
- For the diffuse interface, the high gradients of  $\phi_c$  towards the interface combined with the nonconforming mesh cause numerical issues, leading to numerical artifacts, as shown in the magnification of Figure 6.9b. Regarding the sharp interface, which requires a conforming mesh, these artifacts are not present.

In contrast, the MCOP model exhibits fewer of these difficulties: For the diffuse interface, the crack grows straight up to the interface, where it performs distinct deflection. The deflection is less pronounced for the sharp interface due to the loss of the driving force immediately beyond the interface. However, for both the diffuse and sharp interfaces, the crack continues directly at the edge of the interface, and the crack exhibits the desired analytical profile of the diffuse interface, as illustrated in Figure 6.10.

For a quantitative comparison of the models, the approach of Henry [55] and the analytical analysis of Amestoy and Leblond [13] are used and briefly introduced, in the following. The stress intensity factors for the crack modes I and II of the straight crack, i.e., before the deflection of the crack at the interface, results from

$$K_I = A\sigma_0\sqrt{a}, \quad K_{II} = 0. \quad (6.37)$$

In contrast, the stress intensity factors can be described by

$$\hat{K}_I = f(\varphi)K_{I0}, \quad \hat{K}_{II} = g(\varphi)K_{I0}, \quad (6.38)$$

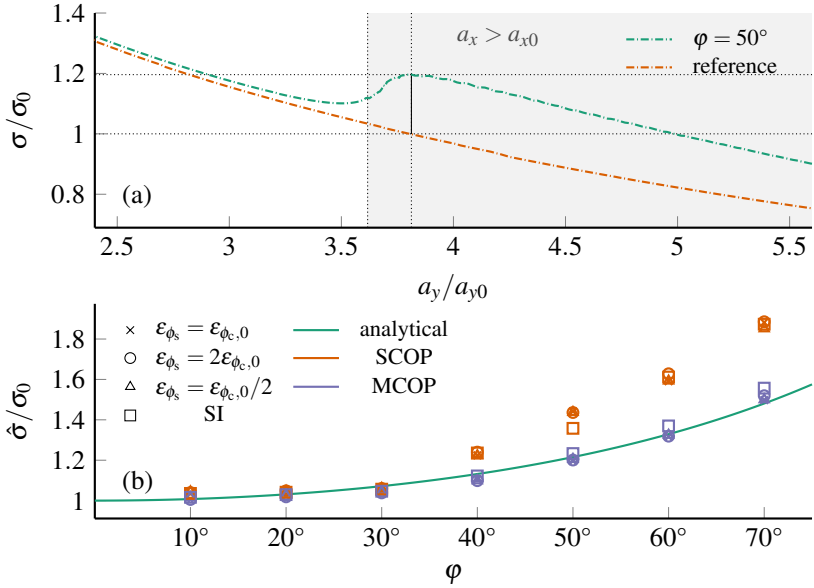


**Figure 6.11:** Exemplary visualization of the evaluation of the crack propagation (a) and comparison with an analytical solution for the SCOP and MCOP model (b), for a crack propagating along an infinitely tough interface, with a different angle  $\theta$ . Various solid length parameters  $\varepsilon_{\phi_c}$  as well as a sharp interface (SI) are examined.

directly after the kink of the crack path, where  $f(\varphi)$  and  $g(\varphi)$  are given by Amestoy and Leblond [13].  $K_{I0}$  is the stress intensity factor right before the kink of the mode I crack. The energy release rates after the kink  $\hat{G}$  results from

$$\hat{G} = \frac{\hat{K}_I^2 + \hat{K}_{II}^2}{E'}, \quad (6.39)$$

while the ratio of  $\hat{G}$  and the energy release rates before the kink  $G_0$  can be expressed using the analytical solution

$$\frac{\hat{G}}{G_0} = f(\varphi)^2 + g(\varphi)^2, \quad (6.40)$$

with  $E' = E/(1 - \nu^2)$ . With Equation (6.37), this ratio can also be given by

$$\frac{\hat{G}}{G_0} = \left( \frac{\hat{\sigma}}{\sigma_0} \right)^2, \quad (6.41)$$

using the applied stress at the interface after the kink  $\hat{\sigma}$ , and a reference stress  $\sigma_0$ , representing the stress of a straight crack with the same crack length in the  $y$ -direction. In Figure 6.11a, an exemplary illustration of the evaluation procedure is given. When the crack hits the interface, the critical stress for propagation increases, which can be observed by a peak in the graph. By determining the maximum value of this peak for which  $a_x > a_{x0}$  holds, and comparing it with the reference stress  $\hat{\sigma}$  of a simulation without a solid interface but with the same crack length in the  $y$ -direction  $a_y$ , a comparison with the analytical solution is possible. In Figure 6.11b, this procedure was conducted for both models, several angles, sharp and diffuse interfaces. For small angles, both approaches show a fairly good agreement with the analytical solution. For higher angles, however, the SCOP model strongly differs from the solution, while the MCOP model still agrees with the analytical solution from the LEFM. Note that a variation of the width of the solid interface was also conducted, where the sharp interface can be considered as a limiting case. Neither increasing nor decreasing of the interface width has any significant effect on the results. For a mesh convergence study of this setup the reader is referred to Section A.3.

In conclusion, regarding the SCOP model, neither the crack grows to the interface, nor is the model able to reproduce the stress increase at which crack propagation occurs along the inclined interface. In contrast, the MCOP model propagates to the interface, develops more significant deflection, and predicts the increase in stress according to theory. Regarding the comparison with sharp solid interfaces, no significant differences could be found. This limits the novel MCOP model not only to the application at diffuse interfaces, but also allows for the application to sharp interfaces. Concerning the diffuse boundary approach, both SCOP and MCOP avoid the need for conforming meshes. However, the MCOP model offers the possibility to extend the homogenization scheme, e.g., by considering jump conditions [22, 90].

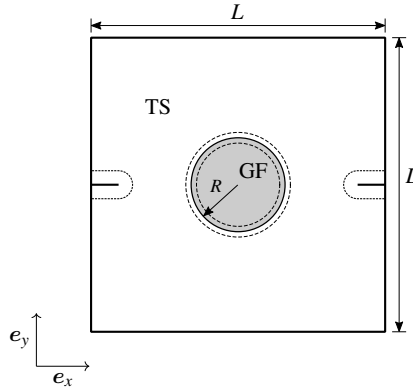


**Figure 6.12:** Schematic of a single inclusion problem. A square plate with side length  $L$ , a spherical glass fiber (GF) inclusion with radius  $R$ , is embedded in a thermoset (TS) matrix. In some studies, an initial crack is placed at the boundary.

### 6.4.3 Single inclusion problem

To motivate the use of mechanical jump conditions, cf. Section 2.3.3, a single inclusion problem (SIP) is considered. Therefore, a square plate with a spherical glass fiber (GF) inclusion is embedded in a thermoset (TS) matrix, cf. Figure 6.12. The fiber is represented in the context of a phase-field method, i.e. a diffuse interface describes a smooth transition from the matrix to the inclusion, cf. Section 2.3. The strain energy densities of such a system under different loads and different homogenization schemes are then investigated. Finally, an crack propagation simulation with an initial crack is performed with the single-obstacle and single-well and both homogenization schemes.

#### 6.4.3.1 Strain energy densities

First, the effective strain energy density  $f_{el}$  and the phase-specific strain energy densities of both phases are discussed. Therefore, the SIP without initial

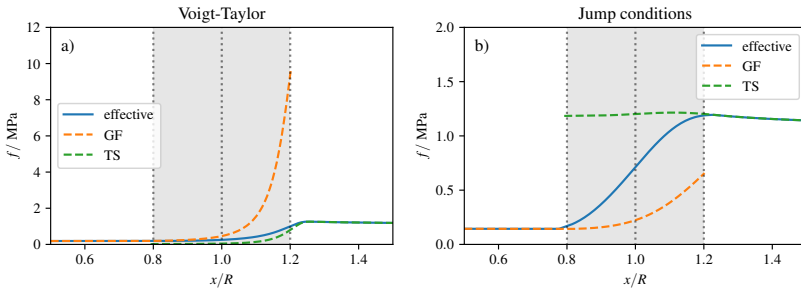


**Figure 6.13:** The effective and the phase-specific strain energy densities of a single inclusion problem with displacement boundary conditions for the Voigt-Taylor scheme (a) and considering jump conditions (b). The diffuse interface is highlighted in gray.

cracks is considered, cf. Figure 6.12. All following evaluations of the quantities are performed from the center of the inclusion along the diagonal of the square domain. The elastic material parameters for both materials are listed in Table 6.2.

**Displacement boundary conditions** In the two-dimensional domain, a plane strain state is assumed. In addition, the orthogonal displacement components at the boundary are constrained to yield 1% macroscopic strain. Figure 6.13 shows the strain energy densities for the Voigt-Taylor scheme and when considering jump conditions. In both cases, the effective value is lower in the inclusion due to the higher stiffness of the inclusion, and a smooth diffusion to the higher value of the matrix can be observed. When considering jump conditions, the phase-specific strain energy density of the inclusion is lower than the effective value, as well as the value of the matrix, throughout the diffuse whole interface. In contrast, the Voigt-Taylor scheme leads to a large increase in the strain energy density of the inclusion towards the outer boundary of the diffuse interface. The values of the matrix is also in the order of magnitude lower than that of the inclusion. Since the phase-specific strain energy densities are part of the driving force for crack propagation in the

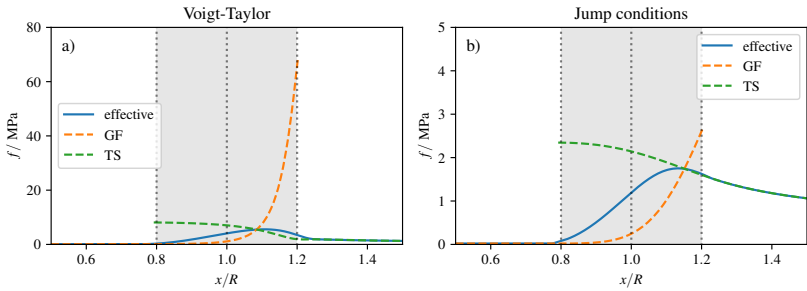


**Figure 6.14:** The total effective and the phase-specific strain energy densities of a single inclusion problem with eigenstrains in the matrix for the Voigt-Taylor scheme (a) and considering jump conditions (b). The diffuse interface is highlighted in gray.

context of the MCOP model, the use of the jump condition is preferable. In this case, for example, assuming the same crack resistance, crack nucleation of the inclusion would be favorable for the Voigt-Taylor scheme. For the jump condition a crack nucleation of the matrix occurs only for a significant higher load.

**Eigenstrains in the matrix** In addition to the external load due to a displacement boundary condition, the system is extended to include an eigenstrain in the matrix material, e.g., to mimic curing shrinkage. Therefore, the orthogonal displacement components at the boundary are set to zero and an inelastic strain of  $-2\%$  of the matrix is assumed. As before, Figure 6.13 shows the strain energy densities for the Voigt-Taylor scheme and if jump conditions are considered. In both cases, the qualitative behavior is similar. Towards the outer boundary of the interface, the energy density of the inclusion exceeds that of the matrix. Also, the highest effective value is at a similar distance from the center. A quantitative comparison reveals that in particular the strain energy density of the glass fiber is predicted to be more than 20 times higher compared to the jump condition framework. In the context of the MCOP model, this would lead to vastly different eigenstrains required to initiate crack growth.

### 6.4.3.2 Crack propagation

Next, the setup is extended to crack growth, so an initial crack is placed in the domain, cf. Figure 6.12. In addition, the eigenstrain, which mimics the shrinkage during curing, is applied linearly in time, allowing the single-obstacle and single-well potentials, as well as the Voigt-Taylor and jump condition schemes, to be compared. The elastic material parameters for both materials are listed in Table 6.2 and the crack resistances are assumed with  $G_c^{\text{TS}} = G_c^{\text{GF}} = 50 \text{ J m}^{-2}$ .

**Boundary and initial conditions** A decomposition of the strain of the matrix, the thermoset (TS), is defined by

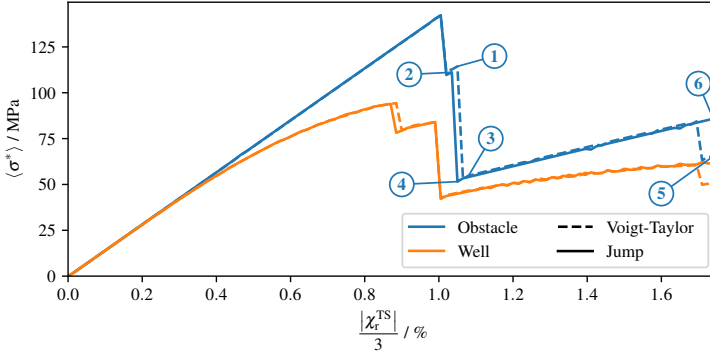
$$\boldsymbol{\varepsilon}^{\text{TS}} = \boldsymbol{\varepsilon}_{\text{el}}^{\text{TS}} + \boldsymbol{\varepsilon}_{\chi}^{\text{TS}}, \quad (6.42)$$

cf. Section 5. Therefore,  $\boldsymbol{\varepsilon}_{\chi}^{\text{TS}}$  accounts for a volume change due to curing and is prescribed in this section by

$$\boldsymbol{\varepsilon}_{\chi}^{\text{TS}} = \frac{\chi^{\text{TS}}(t)}{3} \mathbf{1}, \quad (6.43)$$

where  $\chi^{\text{TS}}$  is initially zero ( $\chi^{\text{TS}}(t=0) = 0$ ) and decreases linearly with time to mimic curing shrinkage. In addition, an effective plane strain state and periodic boundaries are assumed and thermal effects are neglected.

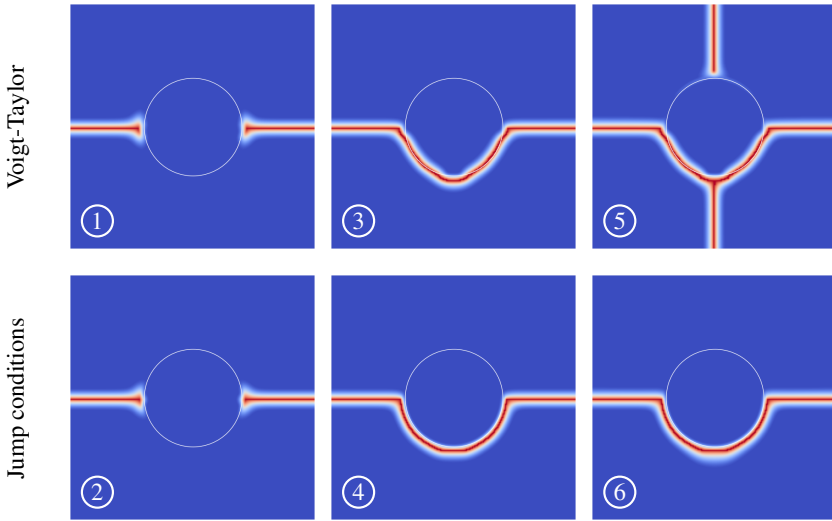
**Results** Figure 6.15 shows the effective maximum principal stress, cf. Section 5.21 and Equation (5), versus the shrinkage of the thermoset. The evolution is depicted for the single-well and single-obstacle potentials, as well as for the Voigt-Taylor scheme and considering mechanical jump conditions in both cases. The single-well potential shows the typical stress degradation associated with such a model. Even without propagation of the completely broken state, a strong degradation of the effective behavior occurs. In contrast, a sharp decrease in stress is observed for the single-obstacle potential. Unstable crack growth is characterized by an almost stepwise decrease in the stress



**Figure 6.15:** Effective maximum principal stress versus the curing shrinkage of the thermoset, cf. Equation 6.43 for the single-well and single-obstacle potential, using the Voigt-Taylor scheme and considering mechanical jump conditions. In addition, individual time steps are annotated with numbers and displayed in Figure 6.16.

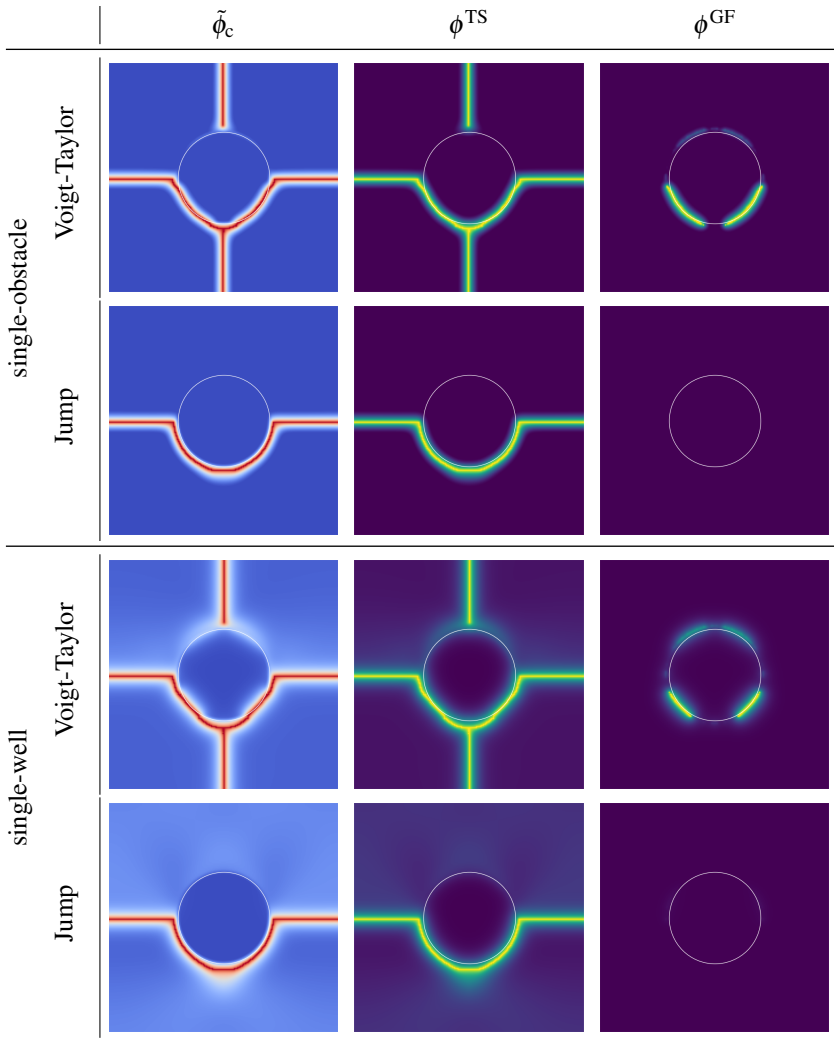
of the corresponding curve and some time steps are labeled with individual numbers. For the latter, the effective crack order parameters are shown in Figure 6.16, although the discussion is restricted to the single-obstacle simulation cases. After the initial crack has grown straight, the interfacial crack stops at the stiffer inclusion, which is an obstacle to direct crack propagation (1,2). In both cases, the Voigt-Taylor scheme and the mechanical jump condition, the crack grows around the inclusion and merge (3,4). However, the Voigt-Taylor scheme exhibits crack growth inside the inclusion, leading to a more triangular crack path, while considering the jump condition leads to a round path outside the inclusion. Subsequently, with the Voigt-Taylor scheme, the cracks grow perpendicular to the initial crack along the cross section with the least matrix, crossing the periodic boundary and finally stopping again at the inclusion (5). For the jump conditions, the same curing shrinkage  $\chi^{\text{TS}}$  is not sufficient to observe any crack growth perpendicular to the initial crack beyond the merging of the crack tips (6).

Figure 6.17 summarizes the final effective crack path  $\tilde{\phi}_c$  for  $\chi^{\text{TS}} = -1.75\%$ , as well as the crack order parameters for both materials  $\phi^{\text{TS}}, \phi^{\text{GF}}$ . As discussed previously, the use of a single-well potential also leads to an increase in the



**Figure 6.16:** Effective crack path for single-obstacle potential, using the Voigt-Taylor scheme, and considering mechanical jump conditions at different time steps, see Figure 6.15. The sharp representation of the inclusion is shown as white contour lines.

crack order parameter far away from the fully broken crack, resulting in a reduced effective stiffness, cf. Figure 6.15. Apart from this characteristic, the final crack paths are similar. Much more noticeable is the influence of the homogenization scheme used, since in addition to Figure 6.16, the contributions to the effective crack order parameter can also be discussed. In all cases where the mechanical jump condition is considered, only the thermoset is damaged, resulting in a circular crack path around the inclusion. The use of the Voigt-Taylor scheme results in a partially completely damaged interface. Since the crack resistances are the same but the Young's moduli differ substantially, such behavior is unexpected in the context of the  $K$  concept, cf. Section 2.4. Finally, the crack path is growing perpendicular to the initial crack in the Voigt-Taylor cases, while the magnitude of the curing shrinkage is not high enough for such a change in crack growth for the jump conditions cases.



**Figure 6.17:** Final crack paths for single-obstacle potential, using the Voigt-Taylor scheme and considering mechanical jump conditions. The effective order parameter  $\tilde{\phi}_c$  as well the phase-specific variants for thermoset  $\phi^{\text{TS}}$  and glass fiber  $\phi^{\text{GF}}$  is displayed.

Material	Elasticity			Fracture		
	$E$	$\nu$	Reference	$G_c$	Parameter	Value
Thermoset	3.45 GPa	0.38	[165]	100.0 J m <sup>-2</sup>	$l_s$	1 $\mu$ m
Glass fiber	73.0 GPa	0.22	[166]	200.0 J m <sup>-2</sup>	$\varepsilon_{\phi_c}$	1.25 $\mu$ m

(a)

(b)

**Table 6.2:** Material properties (a) and interface width parameters (b) for simulating the fracture of FRP volume elements.

### 6.4.4 Application to FRPs<sup>7</sup>

In Section 6.4.2, the same elastic material behavior has been assumed for both regions. But realistic systems with a high contrast in crack resistance will most likely also have a high contrast in their elastic parameters. In this section, a fiber-reinforced polymer (FRP) is chosen to schematically demonstrate the ability of the novel MCOP model to illustrate crack propagation behavior in the context of a material with heterogeneous elastic properties. A quantitative analysis of the results is omitted, as this would most likely require an extension of the model, e.g., a state-of-the-art tension-compression splitting, or accounting for interfacial crack propagation, which is beyond the scope of this work.

The matrix consists of a UPPH resin system [167], reinforced by glass fibers. The material parameters for both materials are given in Table 6.2a, while the interfacial widths used are shown in Table 6.2b. FRPs exhibit a complex fracture behavior: Either the matrix may fail, the fibers may break, or the material may fail due to the debonding of the interface. To investigate crack propagation in such a material, volume elements with a certain fiber volume content, orientation, and periodicity are considered. Boundary conditions, such as normal Neumann or Dirichlet types, do not account for the periodicity of the domain.

<sup>7</sup>The content of this section has been taken directly from Schöller et al. [1, 3] with minor linguistic changes.

Hence a periodic type is chosen: In addition to the periodic order parameters and displacement fields, a superimposed periodic displacement boundary condition [168] is applied in such a way that the macroscopic strain of the volume element follows by

$$\bar{\varepsilon} = \varepsilon(t) \mathbf{e}_x \otimes \mathbf{e}_x, \quad (6.44)$$

where the normal strain in the x-direction,  $\varepsilon(t)$ , will be increased linearly with time, until the volume element exhibits a complete failure.

**Unidirectional 2D volume elements** Firstly, unidirectional fiber reinforced volume elements are investigated. This makes it possible to reduce the system to a 2D system, so as to reduce the computational effort. The square volume elements with a side length of  $100\mu\text{m}$  contains fibers with a radius of  $4\mu\text{m}$ . For different fiber volume fractions  $v_f$ , various realizations will be considered in the following. In Figure 6.18, the effective crack  $\tilde{\phi}_c$  and the contour lines of the fibers are presented in a fully broken state. All realizations show an overall crack direction, perpendicular to the applied load. Thus, the desired and dominant crack opening mode I is reproduced, and the crack paths tend to become more complex, when using a higher fiber volume fraction, as the fibers become an obstacle for the crack, which results in an elongation and contortion of the crack path. This is primarily caused by the lower crack resistance of the matrix. Thus, the crack also often propagates through matrix-dominated regions, but also between fibers caused by stress concentration. Since the MCOP model does not account for the failure mechanism of interfacial debonding, this failure mechanism cannot be observed when the crack propagates in fiber dominated regions. Due to the periodic boundaries, the complete failure of the volume element forces the crack tips to merge. After the merge, partly ‘dead ends’ can thus be observed in some realizations presented in this work.

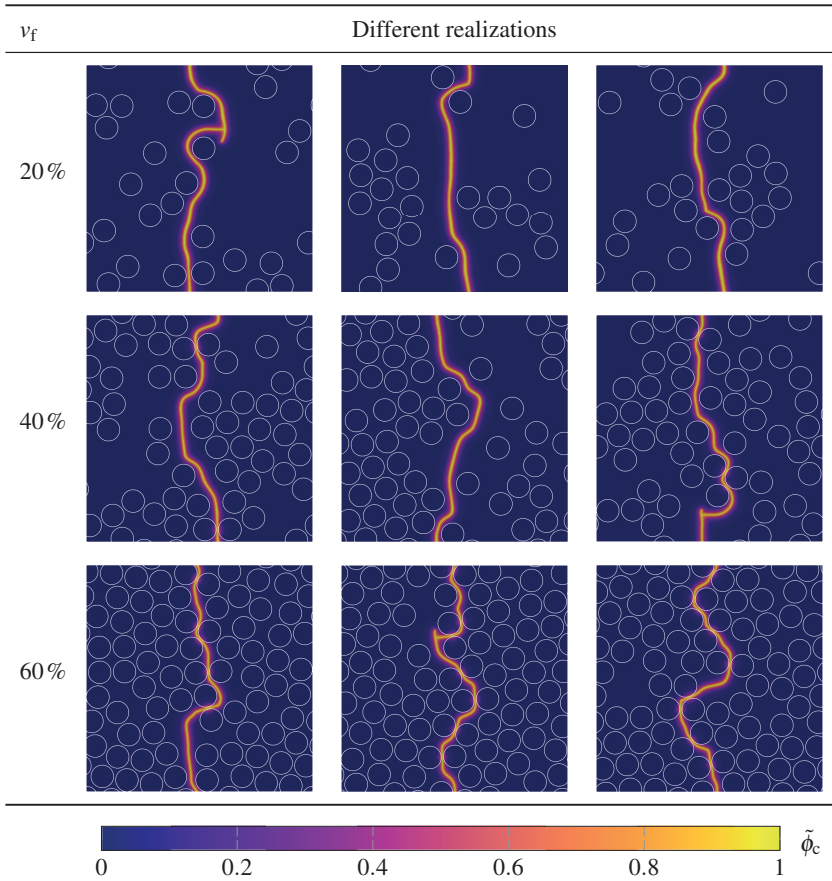


**Figure 6.18:** Different realizations of randomly generated periodic 2D volume elements with unidirectional fibers for varying fiber volume fractions  $v_f$ . Additionally, the effective crack  $\tilde{\phi}_c$ , after uniaxial strain and failure is shown.

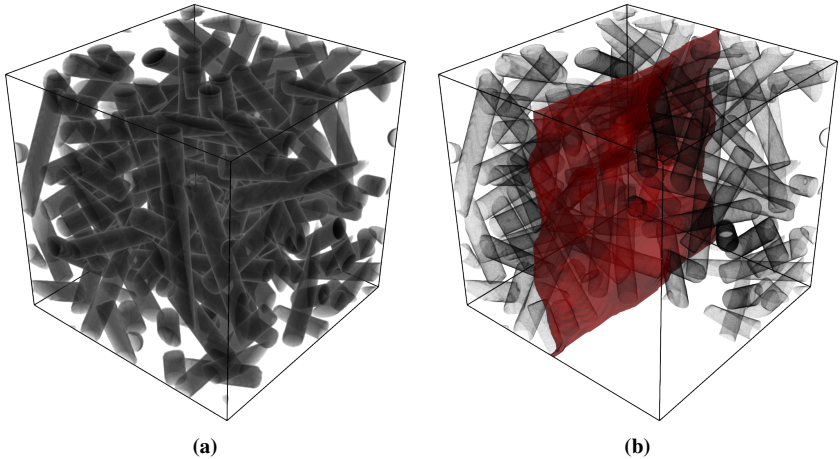


**Figure 6.19:** A randomly generated periodic 3D volume element with isotropic fiber distribution (a) and the fractured volume element after applying an uniaxial strain, highlighted by a red crack surface (b).

**Isotropic 3D volume element** In the case of a 3D volume element, the fiber volume content  $v_f = 25\%$  is chosen with an isotropic orientation distribution. The latter implies that there is no preferential direction in the fiber distribution. As before, the volume element has a side length of  $100\mu\text{m}$ , consisting of fibers with a radius of  $4\mu\text{m}$  and a length of  $80\mu\text{m}$ . The volume element was generated using the approach of Schneider et al. [133] and is shown in Figure 6.19a. As in the 2D case, a macroscopic strain is applied in one direction, in addition to the periodicity, and is increased linearly over time. The failed domain with the red crack surface is shown in Figure 6.19b. As for the 2D simulations, the crack surface is mainly perpendicular to the load direction and occurs solely in the matrix, but still shows a quite complex crack path, due to the fiber distribution and the stress concentration that arise from it.

**Considering mechanical jump conditions** In this section, a glass fiber-reinforced polymer is chosen to schematically demonstrate the advantage of

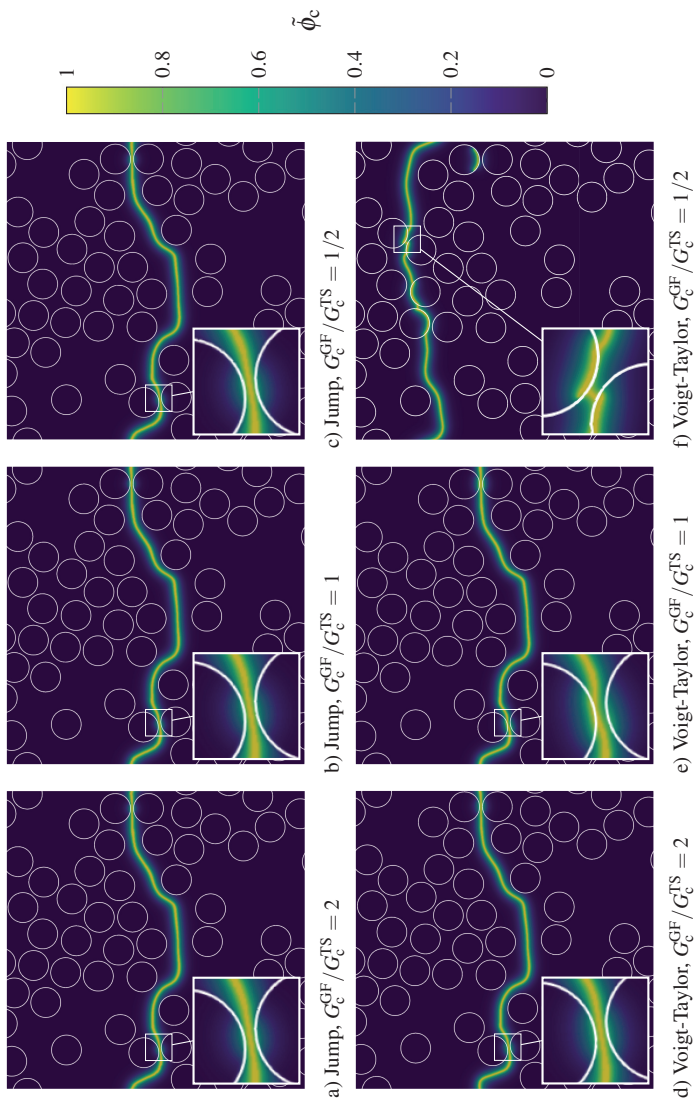


**Figure 6.20:** Crack path of 2D unidirectional fiber-reinforced volume elements after failure if jump condition are considered (a-c) and a Voigt-Taylor scheme (d-f). In addition, the ratio of the crack resistances  $G_c^{GF} / G_c^{TS}$  is varied.

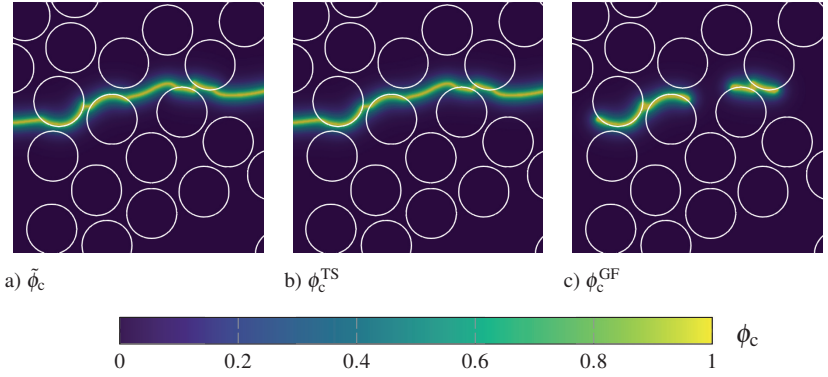


**Figure 6.21:** Detail of the crack path from Figure 6.20f (Voigt-Taylor,  $G_c^{GF}/G_c^{TS} = 1/2$ ) for the effective crack order parameter  $\tilde{\phi}_c$  (a), the thermoset crack order parameter  $\phi_c^{TS}$  (b), and the glass fiber  $\phi_c^{GF}$  (c).

considering mechanical jump condition compared to the application of the Voigt-Taylor scheme in the context of MCOP. This material system is motivated by the high contrast regarding the elastic properties of the matrix material, a thermoset, and the glass fiber: A Young's modulus of  $E^{TS} = 3.45 \text{ GPa}$ , and  $E^{GF} = 73.0 \text{ GPa}$  is assumed for the glass fiber, respectively the thermoset. The Poisson's ratio of fiber and thermoset are  $\nu^{TS} = 0.38$  and  $\nu^{GF} = 0.22$  according to [165, 166]. For simplicity, unidirectional fiber-reinforced volume elements are used. This allows a reduction to a 2D system. A square with a side length of  $100 \mu\text{m}$  and a volume fraction of 40%, with a fiber radius of  $4 \mu\text{m}$  is chosen. As boundary conditions, the macroscopic strain tensor

$$\varepsilon(t) = \bar{\varepsilon}_{xx}(t) e_x \otimes e_x, \quad (6.45)$$

is applied. The function  $\bar{\varepsilon}_{xx}(t)$  will be increased linearly with time, until the volume element fails completely. While the crack resistance of the thermoset is kept constant with  $G_c^{TS} = 100.0 \text{ Jm}^{-2}$ , the crack resistance of the glass fiber is varied. Despite a failure of the fiber being possible under certain circumstances, a failure of the matrix is expected for all ratios used in this work. With the

assumption that the crack surface energy will be minimized and  $G_c^{\text{TS}} > G_c^{\text{GF}}$ , failure of the fiber seems preferential. But even for such a case, the matrix can exhibit a lower crack resistance in the sense of stress intensity factors. So not only the crack surface energy, but also the capability to provide this energy, e.g., by a higher Young's modulus, determines which material component fails. In Figure 6.20 the final crack paths, with the effective crack order parameter field

$$\tilde{\phi}_c = \phi^{\text{TS}} \phi_c^{\text{TS}} + \phi^{\text{GF}} \phi_c^{\text{GF}}, \quad (6.46)$$

are displayed. Regarding the simulations that account for the jump conditions (a-c), the system exhibits the same crack path for all variants. From a nucleation of the crack between close fibers due to stress concentration, a matrix-dominated path is predicted. For the Voigt-Taylor scheme, the two higher ratios (d,e) show the same crack path, even if more fiber damage is present. For the lowest ratio (f) a completely different path is predicted, with damaged fiber, even far away from the final failure crack path. In addition, the crack propagates at the inner side of the fiber interfaces, which is in contrast to the expected behavior. In Figure 6.21 a detailed section of the Figure 6.20f is displayed. In addition to the effective crack order parameter field (a), also the crack order parameters fields of the thermoset (b) and glass fiber (b) are provided. In the latter, it can be observed that in addition to the matrix material also the fiber exhibit completely failure, which is in contrast to the expected behavior.

The macroscopic stress-strain curves are displayed in Figure 6.22. Already in the linear regime of the curves, a difference can be observed: As the Voigt-Taylor scheme describes an upper limit for the elastic energy, it seems reasonable that it exhibits higher stresses. Since it is only accurate for specific cases, such as a parallel material chain, the difference in stress is in accordance to theory [60]. As the failure is dominated by the matrix behavior, the influence of the varied crack resistance of the glass fiber is negligible. However, a small influence during the crack nucleation between two fibers due to the diffuse interface remains. On the contrary, the failures for the Voigt-Taylor scheme occurs at quite different strains. The assumption of same strains for fiber and

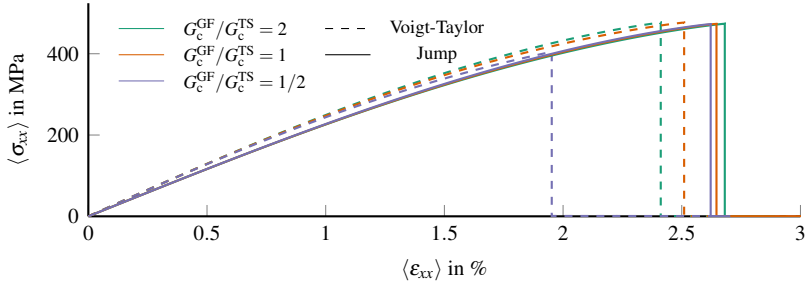


**Figure 6.22:** Macroscopic stress-strain curves of 2D unidirectional fiber-reinforced volume elements for a Voigt-Taylor scheme and if jump condition are considered, with  $\langle \psi \rangle = \frac{1}{V} \int_{\Omega} \psi dv$ . In addition, the ratio of the crack resistances  $G_c^{GF}/G_c^{TS}$  is varied.

matrix leads to high driving forces and therefore an earlier failure of fiber and matrix, compared to the case where jump conditions are considered.

## 6.5 Interim conclusion

In this chapter, different phase-field models for crack propagation in heterogeneous systems have been presented. The SCOP model, which uses a single crack order parameter to account for damage and is based on established approaches, and the novel MCOP model, which uses multiple order parameters to account for damage in each region separately. In combination with the jump condition approach of e.g. Schneider et al. [61], the novel model is able to provide a more accurate representation of the driving forces for crack propagation in heterogeneous materials compared to established crack propagation phase-field models. It has been shown that the MCOP model is able to reproduce the surface energy of the sharp interface for an interfacial crack, while the SCOP has a high error in the local energy density distribution over the diffuse interface. In addition, a study of crack propagation along an sloped interface indicates a higher qualitative and quantitative accuracy of predicting

the crack growth than established models when compared to an analytical solution. Based on a single inclusion problem, the advantages of considering the mechanical jump condition in the MCOP were demonstrated and the single-well and single-obstacle potentials were compared. Moreover, the application of the MCOP model to FRTS was subsequently shown, demonstrating the advantages of the model for such systems, but not limited to this material class. These simulations primarily use boundary conditions to apply the loading, such as a uniaxial tensile test. In contrast, in the following chapter, the curing model from Chapter 5 will induce inelastic strains that cause damage to the FRTS during curing.

# 7 Crack formation during curing of FRTS

In this chapter, the curing simulations of Chapter 5 are combined with the MCOP crack propagation model of Chapter 6 to predict crack formation during the manufacturing process. Therefore, similar to previous simulation studies, crack formation in different levels of abstraction of real microstructures of FRTS are considered and compared. In addition, a modified approach for the choice of an optimal mobility to reduce the computational effort is introduced.

## 7.1 Optimal choice of mobility

The introduced phase-field crack propagation models are solved on the basis of an Allen-Chan type equation, cf. Section 6.1.1, which yields evolution equations for each crack order parameter. Together with the staggered approach, these evolution equations and the linear momentum balance are solved. For the implementation in the context of DEAL.II [163], these PDEs are solved using a time implicit FEM approach. In contrast, the PACE3D frameworks [164] relies on an explicit time integration scheme for the order parameters. In the context of the multiphase-field method, this allows fast execution even for a large number of phases using e.g. local reduced order parameter techniques. A disadvantage of the scheme is the limited numerical stability of the time integration. For crack propagation models, a fixed but otherwise arbitrary mobility is usually chosen and a time step width  $\Delta t$  within the stability region is used. This approach ensures a stable time integration, but can lead to a large number

of inner iterations necessary to satisfy the static crack propagation criterion, cf. Section 6.2. Therefore, an optimal choice of mobility is desirable to reduce the computational cost, and will be derived in the following.

A generic evolution equation for a crack order parameter  $\phi_c^\alpha$  can be written by

$$\dot{\phi}_c^\alpha = A\Delta\phi_c^\alpha + B\phi_c^\alpha + C, \quad (7.1)$$

with a prefactors  $A$  for the diffuse term,  $B$  for the linear term and an independent term  $C$ . In this section the investigation are restricted to the MCOP model with the single-obstacle potential, whereby these prefactors can be identified with

$$A = M^\alpha G_c^\alpha, \quad B = -\frac{2M^\alpha}{\varepsilon_{\phi_c}} f_{el}^\alpha, \quad C = \frac{M^\alpha}{\varepsilon_{\phi_c}} \left( 2f_{el}^\alpha - \frac{9}{32\varepsilon_{\phi_c}} G_c^\alpha \right). \quad (7.2)$$

For the implementation in PACE3D a finite volume approach is chosen. Together with an equidistant grid this leads to a central difference scheme for the second derivatives with

$$\frac{\partial^2 \phi}{\partial x \partial x} \approx \frac{\phi_{i+1} - \phi_i + \phi_{i-1}}{\Delta x^2} \quad (7.3)$$

for a derivative in the spatial direction  $x$  with a cell size  $\Delta x$  in this direction. Based on this, the CFL condition [169, 170]

$$\Delta t \leq \sum_i^3 \frac{\Delta x_i}{|B| \Delta x_i + 2 \frac{A}{\Delta x_i}}, \quad (7.4)$$

can be formulated, with  $i = 1, 2, 3$  for the corresponding direction. With Equation (7.2), and accounting for all spatial direction

$$M^\alpha \Delta t \leq \sum_i^3 \frac{\Delta x_i}{2 \left( \frac{\Delta x_i f_{el}^\alpha}{\varepsilon_{\phi_c}} + \frac{G_c^\alpha}{\Delta x_i} \right)} \quad (7.5)$$

follows. This condition is usually used to determine a stable time step width  $\Delta t$ . Instead, the time step width can be kept constant, to e.g. enable a stable

coupling of other equations such the heat equation, and a stable mobility  $M^\alpha$  could be chosen.

However, instead of choosing a global value for the mobility in this chapter, the value is determined locally for each cell in the grid. Ultimately, this approach results in spatially varying mobilities  $M^\alpha = M^\alpha(\mathbf{x})$ , which is are longer a numerical parameters to chose freely, but are determined by the equality case of Equation (7.5) with a certain safety factor. Note that the finite volume method used usually preserves fluxes. With varying mobilities this characteristic is no longer valid, but since this is not a necessary restriction for the numerical scheme in this work, the chosen approach can be considered as legitimate.

## 7.2 Results

**Material parameters** The elasticity, thermal, curing and fracture material parameters for the UPPH resin and glass fiber are chosen according to the previous simulation studies, cf. Chapter 5. Therefore, most of the resin properties are taken from Schwab and Denniston [76]. A complete list of references for each property is given in Table 5.2. In addition, the material parameters for the glass fiber are listed in Table 5.1. Additionally to these already introduced material parameters, crack resistances  $G_c^\alpha$  are also required and are assumed to be the same as in the previous crack propagation studies in FRPs and are listed in Table 6.2a.

**Boundary and initial conditions** For the boundary and initial conditions for the displacement and temperature field, the same approach is used as in Chapter 5. Therefore, the compression molding process is represented by two steps, a heating from room temperature to 373 K for 3 minutes and a subsequent cooling to room temperature, whereas the curing process takes place during the first phase. The volume elements are considered to be periodic, except

for one direction which is associated with the molds through special boundary conditions, cf. Section 5.2.

For the crack order parameters, an initial crack is placed to avoid cumbersome techniques to consider crack nucleation in a quantitative manner, cf. Section 6.2. Therefore, a crack with 25  $\mu\text{m}$  length is placed in a resin-rich region. Although this approach lacks sophistication, it is considered valid in the context of this work. The results presented are based on generated volume elements and a general statement is possible only based on many of such ensembles. Although several samples are used in this work, they are not enough to be statistically significant. Nevertheless could a manual placed initial crack still give insights to the basic fracture behavior of FRTS. Moreover, such an initial crack can also be associated with imperfections such as voids or a not completely closed flow front resulting from an uneven flow of the initial charge through the geometry of the final component. In this sense a manual placement of an initial crack seems admissible.

**Unidirectional fiber-reinforced thermoset** First, unidirectional fiber-reinforced volume elements in a 2D system are considered. Figure 7.1 shows the final crack path for 10 %, 30 % and 50 % fiber volume content for three different samples. In addition, the initial crack is shown in red contour lines and the corresponding sharp fiber-resin interface is displayed in white contour lines.

Although there is no preferred crack growth direction in the microstructure, the direction of the initial crack also determines the preferred direction of crack growth during cure. Thus, a straight final crack from the initial crack is expected for a pure resin system. For 10 % fiber volume content, only a small deviation from such a straight crack path can be observed. This occurs because the fiber represents an obstacle to straight crack propagation. Some ensemble members, such as Figure 7.1d, show a complete failure of the volume element in one direction, where the fibers only slightly alter the straight crack path. For 30 % fiber volume content, the crack paths are more deflected by the fibers.

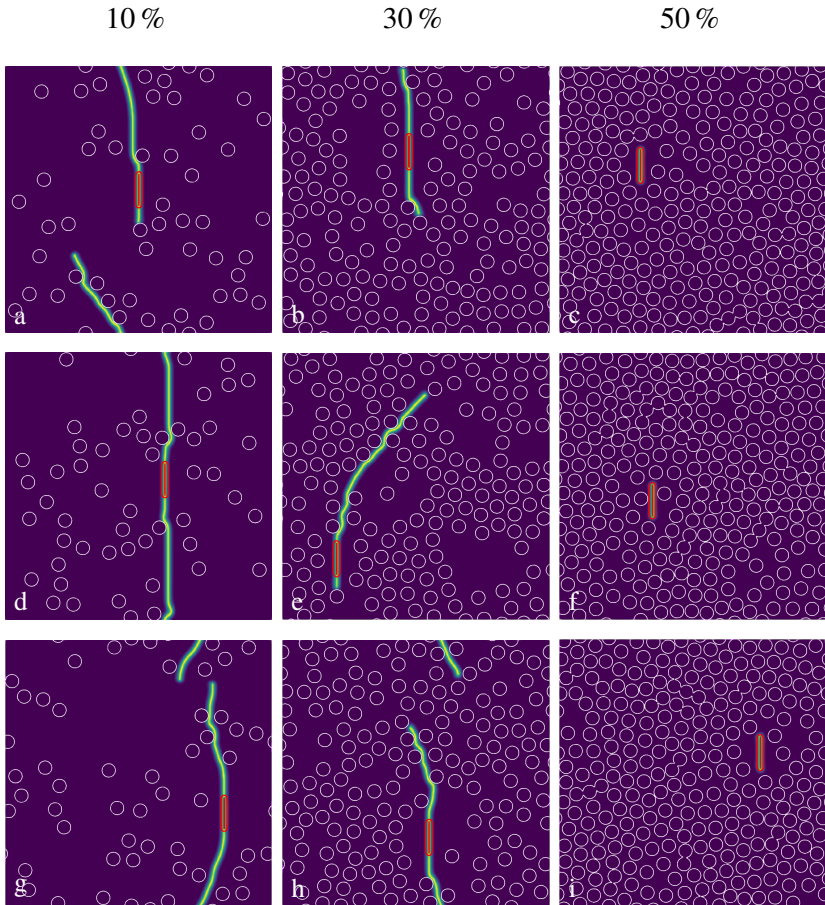


**Figure 7.1:** Final effective crack order parameter field after curing for different fiber volume fractions and ensembles for the unidirectional fiber-reinforced volume elements. In addition, contour lines represent the corresponding sharp fiber-matrix interface and red contour lines represent the initial crack.

For example, Figure 7.1e shows a strong deflection from the initial crack orientation during crack growth due to the fibers. Overall, the final crack path is less spread over the volume elements and no complete failure occurs. For the 50 % ensembles, there is no crack growth other than the initial growth. This is mainly due to the stiffer fibers, which exhibit no chemical shrinkage and lower thermal expansion. In higher amounts, they strongly reinforce the system and transfer the main load so that the initial crack is almost stress free. This is also illustrated by the maximum principal stress shown on the left in Figure 7.2. There exist a circular peak in stress in the fibers surrounding the initial crack, while the crack itself has almost no stress and therefore lacks the necessary driving force to propagate the crack further.

Note that the unidirectional fiber-reinforced sample does not accurately depict the real microstructure of a compound molded glass fiber-reinforced UPPH system. Thus, the fiber cross sections presents a relatively low obstacle to crack growth and the effective crack behavior seems to be mainly dominated by the volume fraction. Therefore, an extension to a more realistic microstructure seems reasonable and is carried out in the following.

**Two-dimensional curved fiber-reinforced thermoset** In the next step, the microstructure is represented by curved long fibers. In order to reduce the computational effort, the simplification to 2D is maintained. As before, Figure 7.3 shows the final crack path for 10 %, 30 % and 50 % fiber volume content for three different samples, along with the initial crack and the corresponding sharp fiber-resin interface illustrated by red and white contour lines, respectively. In contrast to the unidirectional fiber-reinforced elements, none of the 10 % ensemble members exhibits a crack across the entire domain, nor are they straight. Instead, the cracks follow the curved fibers either directly at the interface or a deflections before reaching the interface. The latter is likely due to the complex stress state and different eigenstrains of the materials. As the volume fraction of the fiber increases, the crack path becomes more constrained, resulting in shorter crack paths and more pronounced deflections and kinks in the crack path. As before, the 50 % ensemble shows no crack growth

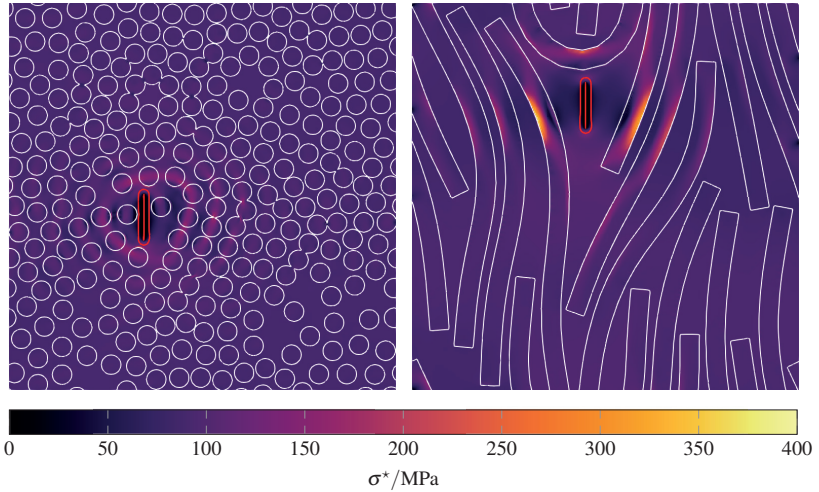


**Figure 7.2:** Distribution of maximum principal stress  $\sigma^*$  for volume elements with a fiber volume fraction of 50% for a unidirectional fiber-reinforced system (left) and a two-dimensional curved fiber-reinforced system (right) after curing simulation with a crack (red).

other than the initial growth as the high amount of stiffer fibers transfers the load. This is again evident from the maximum principal stress displayed on the right side of Figure 7.2, where the peaks are in the fibers surrounding the initial crack, which experience only low stresses.

**Three-dimensional curved fiber-reinforced thermoset** Figure 7.4 shows a volume element with 10% fiber volume content. In addition to the curved fibers, the crack is shown in color, with the different colors representing the crack growth at different time steps, starting from the initial disc-shaped crack. Due to the volumetric nature of the crack and the three-dimensional strain state, a direct comparison with results from 2D simulations is problematic. The final size of the crack appears small compared to the 2D results. This may be due to the smaller domain size, which tends to restrict crack growth

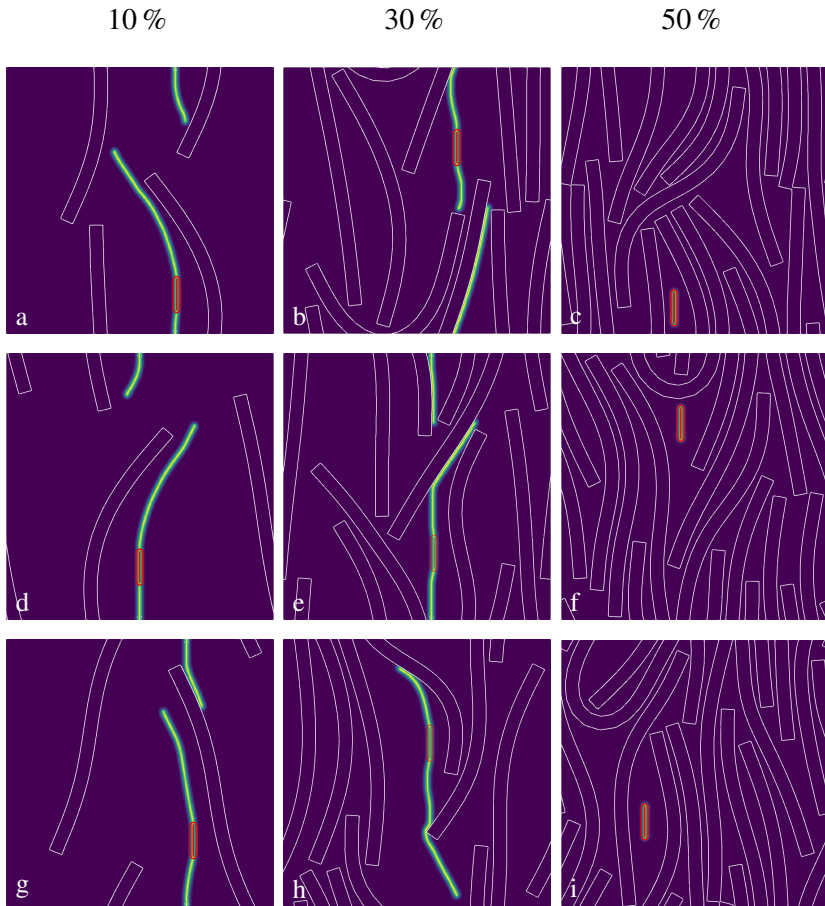


**Figure 7.3:** Final effective crack order parameter field after curing for different fiber volume fractions and ensembles for the curved fiber-reinforced volume elements in 2D. In addition, contour lines represent the corresponding sharp fiber-matrix interface and red contour lines represent the initial crack.

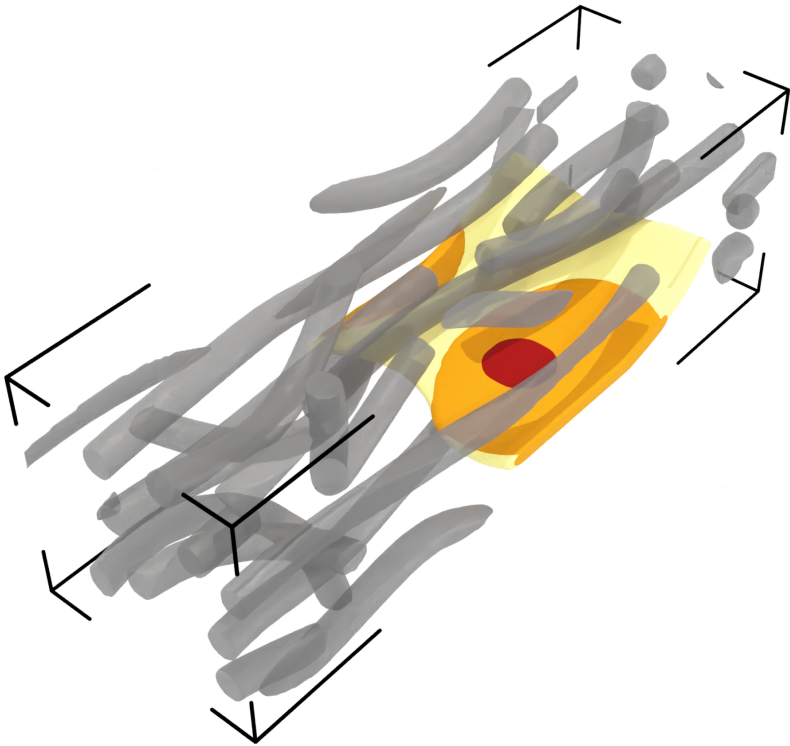


**Figure 7.4:** Volume element with 10% fiber volume content and the final crack in color. The different colors depicts the crack growth from the initial state to the final crack.

due to the boundary conditions. Nevertheless, the volume elements are more representative of a real microstructure of the FRTS. Moreover, a complete failure or severely damaged microstructure is not expected since the composite molding process is capable of producing fully functional components of glass fiber reinforced UPPH resin. Therefore, the three-dimensional result supports the assumption that microcrack formation during the curing process is limited to local areas of high stress concatenation and does not propagate through a larger area of the component.

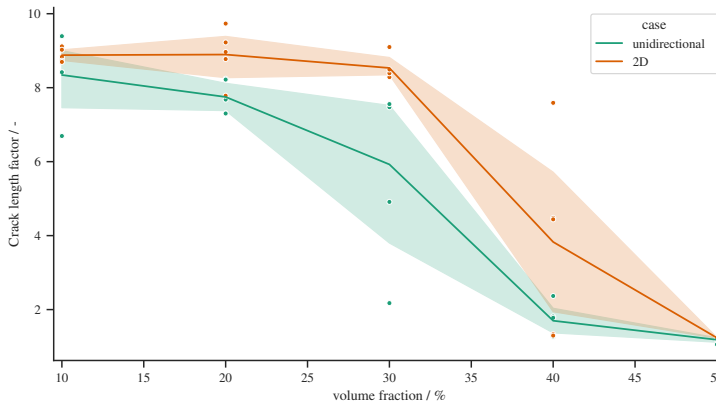


**Figure 7.5:** The crack length factor, the integral of the effective crack order parameter of individual simulations normalized by the initial crack in pure resin, against the fiber volume fraction. Distinguished by the level of abstraction of the microstructure (case), and confidence intervals are provided.

**Comparison** To compare the previous results, the integral of the effective crack order parameter of individual simulations, normalized by the initial crack in pure resin is plotted against the fiber volume fraction in Figure 7.5. In addition, two more volume fractions are considered, and confidence intervals are given. Note that a higher crack length factor indicates a longer crack, but does not specify the path of the crack, i.e., whether the crack is straight or more complex, e.g., deflected by fibers. For the for 10 % unidirectional fibers, the crack length is high, due to the mainly straight cracks. While with higher fiber volume fraction, the crack length decreases as the cracks do not propagate through the whole domain. For the curved fibers, the crack length for 20 % volume fraction is even increased because the curved fiber allows more crack propagation, as the path is deflected along the fibers resulting in longer crack paths. This behavior can be observed up to 40 % volume fraction. While these curved fiber volume elements still exhibit significant cracks, the crack length decreases drastically for the relatively evenly spaced unidirectional fiber volume elements.

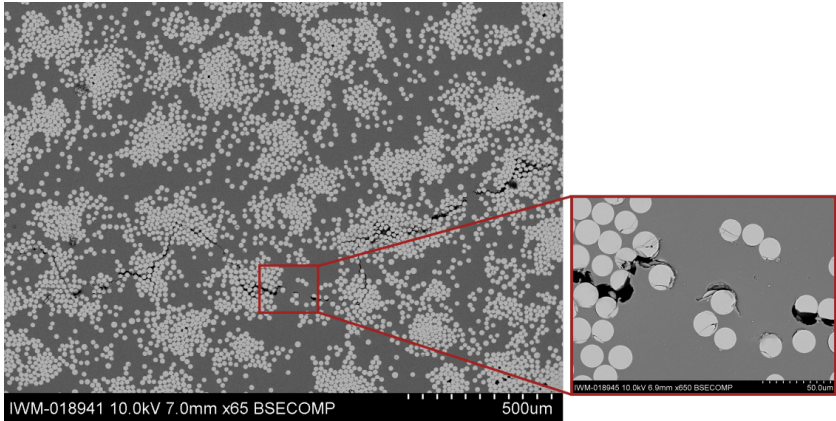


**Figure 7.6:** Cross-sectional SEM image capturing the fracture within unidirectional glass fiber-reinforced thermoplastic. Reprinted from [171].

Note that the reduction to 2D is expected to introduce a systematic error. Together with other sources of error such as material parameters, the quantitative aspect of these results should be treated with caution. However, the qualitative behavior and the underlying crack formation mechanism are still considered to be representative.

In Figure 7.6, an SEM image of a fractured cross section of a unidirectional glass-reinforced thermoplastic is shown. In the absence of directly comparable experimental results in literature, a comparison based on this image is discussed in the following. Note that a different matrix material as well as a different loading, i.e. boundary conditions, are considered. Nevertheless, a qualitative comparison of the crack mechanism is possible. The unidirectional fiber-reinforced simulations shows a matrix dominated failure. In contrast, the SEM image shows a pronounced fiber-matrix interface failure. The crack propagation model used in the present work does not include a special mechanism to account for interfacial crack propagation. Thus, it does not take into account the surface energy in such interfaces, which would be released for crack growth at these interfaces and affect the Griffith fracture criterion [30]. Such a

mechanism could lead to a different crack behavior, as a crack at the interface could be favorable. Also the initial crack is placed in the matrix due to the feasibility of this approach. In real volume elements, a crack is expected to nucleate at the fiber-matrix interface. However, after the initial straight crack in the resin, the crack propagates along the fiber-matrix interfaces of the curved fibers. This indicated that for larger systems with the possible longer cracks, the crack could propagate along the interface similar to the experimental image taken from an already highly damaged specimen. A direct comparison of of this behavior with experimental results is not possible due to the lack of images perpendicular to the fiber cross section. Despite a deficit in the comparability of simulations and experiments, a similar crack propagation could be observed. Nevertheless, an extension of the model used to include crack nucleation and interfacial failure could improve the prediction of crack formation during the curing process.

## 8 Conclusion and outlook

This work deals with the modeling of curing and crack propagation during the compression molding process of FRTS on the nano and micro length scale. In the following, the results of the different aspects of this work are summarized and final conclusions are drawn. In addition possible extension of the models and overall approach is presented.

**Two-stage polymerization using molecular dynamics<sup>1</sup>** Based on molecular dynamics simulations, a simplified but industrially used resin system was extended by adding a fiber surface and sizing layers. The approach of Schwab and Denniston [76] was used to model the two-stage polymerization of the UPPH resin. In addition,  $\gamma$ -MPS was chosen for the coupling agent, and further assumptions were made about the structure of the sizing. A systematic procedure for the development of a final cured system was presented. Based on this approach, evaluations of average quantities during the reactions were performed. Moreover, the system was also evaluated along the normal of the fiber surface, which provides a spatial analysis of the fiber-sizing-resin system.

Based on the established REACTER framework, coupling agent monomers undergo a condensation reaction yielding a distribution of monomers, dimer and higher oligomers. Due to a lack of information in the literature, validation of this distribution did not seem feasible. Nevertheless, this offers an alternative approach to an arbitrarily prescribed distribution. In both the UP as well the

---

<sup>1</sup>The content of this section has been taken directly from Schöller et al. [2] with minor linguistic changes.

radical reaction, a similar distribution of the final conversion degree could be observed: Highest in the pure resin layer and decreasing towards the fiber, with the lowest value directly at the fiber surface. Notwithstanding, it was found that the transition between the different layers was almost smooth. This is most likely due to the diffusion of some molecules, compensating for the change in the composition of sizing and resin layers.

The introduction of the fiber surfaces reduced the diffusivity in the normal direction to the surface. This leads to a reduced overall conversion degree of the radical reaction of the final system, compared to a pure resin system. Moreover, this also results in locally varying conversion degrees and anisotropic radical polymerization at the fiber surface. A comparison of the results of this work to experiments would be highly desirable. Although various investigations of the fiber interface were conducted [68, 172, 173] a comparison of the results is not possible. These experiments are mainly focused on a mechanical characterization of the interphase based on micromechanical tests. This results in effective quantities for the whole fiber-sizing-resin interface. Furthermore, these experiments clearly show that a significant part of the failure of FRP is due to the interface between fiber and resin, including the sizing. Therefore, a better understanding of the detailed processes during polymerization could also improve the design of such experiments. Nevertheless, any experiments investigating, for example, the diffusion of the sizing component during the reaction would allow a direct validation of the presented results. Moreover, this work now makes it feasible to include the mechanical testing of the final system within the MD. This is a non-trivial task, but it allows a direct comparison with the existing literature and could be the focus of a subsequent work.

In other subsequent works, the complexity of the fiber sizing can be increased: Instead of only one coupling agent, several coupling agents or a different film former could be used. In addition, other additives of the sizing could be considered. Also, the basic modeling of the condensation reaction could be extended. For example, a coarse-grained approach could provide detailed insight into the

behavior of the sizing during condensation, which could enhance the full atomistic studies of the proposed approach. The assumption of the rigidity of the fiber surface could also be dropped, requiring the complex atomic structure of the fiber surface to be modeled. This could potentially improve the results, but would significantly increase the complexity. Last but not least, a further investigation of the generated system can be conducted. For example, an evaluation of the material properties of the system, e.g. the thermal or (visco-)elastic parameters, would be of great interest. In particular, an evaluation dependent on the distance to the fiber surface, as proposed in this work, would allow a deeper understanding of the sizing-resin interface. And eventually, complex properties such as a realistic interfacial fracture energy could be derived from such a system.

**Phase-field models for crack propagation in heterogeneous systems<sup>2</sup>** In this work, two different phase-field models for crack propagation in heterogeneous systems were introduced and compared:

- A SCOP model, based on established approaches, which uses a single crack order parameter to account for damage.
- A novel MCOP model, that introduces multiple order parameters in order to distribute the effective damage to the individual regions, modeled by its own set of order parameters. This results in multiple evolution equations, each of which has a constant crack surface energy.

It was shown that the SCOP model is not able to reproduce the surface energy of the sharp interface for an interfacial crack, especially when the same length parameters are chosen for the solid and crack problem. In comparison, the novel MCOP formulation avoids any errors in that case. Furthermore, the model demonstrated the same kinetics and crack profiles during the propagation though an artificial interface, which confirms that multiple crack order

---

<sup>2</sup>The content of this section has been taken directly from Schöller et al. [1] with minor linguistic changes.

parameters can generate a continuously effective crack. An extension to an infinitely tough interface indicated further problems with the SCOP model, as the crack is deflected from the interface before it hits the interface itself, and maintains a certain distance from it. In contrast, the novel MCOP model demonstrates a more pronounced kink of the crack path at the interface and grows directly along the interface, for both sharp and diffuse interfaces. A quantitative comparison between the models for different angles of the interface and an analytical solution also showed a huge improvement in the modeling of crack propagation in heterogeneous materials: In particular, for high angles of the interface the SCOP model cannot replicate the analytical solution, where the MCOP model still shows very good agreement with it.

The application of the novel model to FRP for unidirectional fibers in 2D and the extension to a 3D domain with isotropic fiber orientation distribution shows that the model is able to depict crack evolution in such a complex system, including crack nucleation and merging. Notwithstanding the fact that the crack phase-field model avoids established extensions, such as a tension-compression splitting or the removal of the interface parameter dependence, the many remaining advantages of using multiple crack order parameters could be demonstrated. In future work, a tension-compression split, for example based on the work of Storm et al. [148], could further improve the model. In addition, a combination with a solid-solid phasefield transition model and plasticity could allow the study of other material systems, e.g., crack evolution during martensitic phase transformation [174]. The inclusion of an interfacial crack resistance could also allow for a more sophisticated simulation of FRP failure, by enabling realistic fiber debonding.

**Considering mechanical jump conditions in the MCOP model<sup>3</sup>** In this work a novel MCOP model is proposed for fracture in heterogeneous materials. Despite the improvement in the qualitative and quantitative prediction

---

<sup>3</sup>This section is based on the work of Schöller et al. [3]. Minor linguistic changes and additions have been made.

of crack paths for such systems, the model has some limitations. Therefore, an extension of this model was proposed in this work and investigated: Instead of a basic Voigt-Taylor homogenization scheme, the approach is extended to consider mechanical jump conditions based on Schneider et al. [61]. First, the single inclusion problem was introduced to demonstrate the difference in elastic driving forces of the two schemes. In addition, the final crack paths due to eigenstrains mimicking chemical shrinkage were discussed for the single inclusion problem for both schemes as well as the single-well and single-obstacle schemes. In this context, the jump condition scheme resulted in a better agreement with the expected fracture behaviour.

An exemplary FRP system was introduced to investigate the behavior of both schemes. Therefore, the crack resistance of the glass fiber was varied. The Voigt-Taylor homogenization scheme failed to predict reasonable crack paths for contrary contrasts of elastic modulus and crack resistance. Instead, the fiber failed as well, resulting in different paths. In contrast, when mechanical jump conditions are considered, the model yields the same final crack path for all crack resistances presented, since the mechanical driving force for crack propagation is modeled more independently of the elastic properties of other physical domains. Moreover, this behavior could also observe in the stress-strain curves. While the Voigt-Taylor scheme fails at different loading points, the novel scheme shows a negligible scatter.

Based on this work, more extensive simulation studies on the failure mechanism of FRP materials, as well as other complex systems such as polycrystalline materials, e.g., in hydrothermal environments [175], solid oxide fuel cells among others, can be conducted. Combined with experimentation, this offers the opportunity to improve a broad range of engineering applications.

### **Crack propagation during curing in fiber-reinforced thermosets**

In order to predict the crack formation of FRTS during curing, a method to generate virtual fiber-reinforced volume elements was introduced in Chapter 4. For this purpose, an approach based on MD was used to consider not only

straight fibers, but also long curved fibers. In the following Chapter 5, the curing process, which was previously modeled on the atomic length scale, was simulated on the micro length scale using continuum mechanics. Incorporating thermal and chemical strains, the resulting residual stresses were discussed for different levels of abstraction of the microstructure of FRTS. Finally, in Chapter 7, the various aspects of this work were brought together. Based on the novel crack propagation model for heterogeneous systems and the curing model for FRTS, crack formation during manufacturing was simulated. Despite the lack of possibility to compare the results with experiments and the difficulty to assess the quantitative results, the cracking mechanisms of this material class could be observed. It was demonstrated that the presented approach is able to show crack formation during curing of glass fiber-reinforced UPPH resin. For further work, such a model could benefit from incorporating the viscoelastic material behavior of the resin, despite the increase in computational cost and lack of material properties during the various stages of the curing process. Based on further experimental investigation and incorporation of crack nucleation and interfacial crack propagation, a more quantitative prediction of crack formation during the curing process seems feasible and would be highly desirable for understanding this material class and its failure mechanism.

# A Appendix

## A.1 Intermolecular interaction potentials

The intermolecular interaction potential energy function  $U^{\text{inter}}$ , cf. (2.64), consists of several contributions introduced below and are based on the COMPASS force field [101–103]. Note that the individual parameters in these contributions are usually dependent on the atom types, but for the sake of clarity additional sub or superscripts are omitted.

**Bonds** The bonds contribution consist of a potential with harmonic and anharmonic terms

$$U_{ij}^{\text{B}} = K_2^{\text{b}} (r_{ij} - r_0)^2 + K_3^{\text{b}} (r_{ij} - r_0)^3 + K_4^{\text{b}} (r_{ij} - r_0)^4 \quad (\text{A.1})$$

with the parameters  $K_2^{\text{b}}, K_3^{\text{b}}, K_4^{\text{b}}$  and the equilibrium bond distance  $r_0$ .

**Angles** The angle contribution can further decomposed in

$$U_{ijk}^{\text{A}} = U_{ijk}^{\text{a}} + U_{ijk}^{\text{bb}} + U_{ijk}^{\text{ba}}, \quad (\text{A.2})$$

with a angle potential, again with harmonic and anharmonic terms

$$U_{ijk}^{\text{a}} = K_2^{\text{a}} (\theta_{ijk} - \theta_0)^2 + K_3^{\text{a}} (\theta_{ijk} - \theta_0)^3 + K_4^{\text{a}} (\theta_{ijk} - \theta_0)^4, \quad (\text{A.3})$$

with the parameters  $K_2^a, K_3^a, K_2^a$  and the equilibrium angle  $\theta_0$ . The bond-bond term follows by

$$U_{ijk}^{\text{bb}} = M^{\text{bb}} \left( r_{ij} - r_1^{\text{bb}} \right) \left( r_{jk} - r_2^{\text{bb}} \right), \quad (\text{A.4})$$

with the parameters  $M^{\text{bb}}$  and the distances  $r_1$  and  $r_2^{\text{bb}}$ . In addition, bond-angle term

$$U_{ijk}^{\text{ba}} = N_1^{\text{ba}} \left( r_{ij} - r_1^{\text{ba}} \right) \left( \theta_{ijk} - \theta_0 \right) + N_2 \left( r_{jk} - r_2^{\text{ba}} \right) \left( \theta_{ijk} - \theta_0 \right) \quad (\text{A.5})$$

with the parameters  $N_1^{\text{ba}}, N_2^{\text{ba}}$  and the distances  $r_1^{\text{ba}}$  and  $r_2^{\text{ba}}$ .

**Dihedrals** The dihedrals contribution can further decomposed in

$$U_{ijkl}^{\text{D}} = U_{ijkl}^{\text{d}} + U_{ijkl}^{\text{mbt}} + U_{ijkl}^{\text{ebt}} + U_{ijkl}^{\text{aat}} + U_{ijkl}^{\text{at}} + U_{ijkl}^{\text{bb13}}, \quad (\text{A.6})$$

with a dihedral potential

$$U_{ijkl}^{\text{d}} = \sum_{n=1}^3 K_n^{\text{d}} \left( 1 - \cos \left( n\phi_{ijkl} - \phi_n^{\text{d}} \right) \right) \quad (\text{A.7})$$

with the parameters  $K_1^{\text{d}}, K_2^{\text{d}}, K_3^{\text{d}}$  and angles  $\phi_1^{\text{d}}, \phi_2^{\text{d}}, \phi_3^{\text{d}}$ . The middle-bond-torsion term follows by

$$U_{ijkl}^{\text{mbt}} = \left( r_{jk} - r_2^{\text{mbt}} \right) \left( A_1 \cos \left( \phi_{ijkl} \right) + A_2 \cos \left( 2\phi_{ijkl} \right) + A_3 \cos \left( 3\phi_{ijkl} \right) \right), \quad (\text{A.8})$$

with the parameters  $A_1, A_2, A_3$  and the distance  $r_2^{\text{mbt}}$ . Moreover the end-bond-torsion term

$$U_{ijkl}^{\text{ebt}} = \left( r_{ij} - r_1^{\text{ebt}} \right) \left( B_1 \cos \left( \phi_{ijkl} \right) + B_2 \cos \left( 2\phi_{ijkl} \right) + B_3 \cos \left( 3\phi_{ijkl} \right) \right) + \quad (\text{A.9})$$

$$\left( r_{kl} - r_3^{\text{ebt}} \right) \left( C_1 \cos \left( \phi_{ijkl} \right) + C_2 \cos \left( 2\phi_{ijkl} \right) + C_3 \cos \left( 3\phi_{ijkl} \right) \right), \quad (\text{A.10})$$

with the parameters  $B_1, B_2, B_3, C_1, C_2, C_3$  and the distance  $r_1^{\text{ebt}}, r_3^{\text{ebt}}$  and the angle-angle-torsion term

$$U_{ijkl}^{\text{aat}} = (\theta_{ijk} - \theta_1^{\text{aat}}) (D_1 \cos(\phi_{ijkl}) + D_2 \cos(2\phi_{ijkl}) + D_3 \cos(3\phi_{ijkl})) + \quad (\text{A.11})$$

$$(\theta_{ikl} - \theta_2^{\text{aat}}) (E_1 \cos(\phi_{ijkl}) + E_2 \cos(2\phi_{ijkl}) + E_3 \cos(3\phi_{ijkl})), \quad (\text{A.12})$$

with the parameters  $D_1, D_2, D_3, E_1, E_2, E_3$  and the angles  $\theta_1^{\text{aat}}, \theta_2^{\text{aat}}$ . In addition, the angle-torsion follows by

$$U_{ijkl}^{\text{at}} = M^{\text{at}} (\theta_{ijk} - \theta_1^{\text{at}}) (\theta_{jkl} - \theta_2^{\text{at}}) \cos(\phi_{ijkl}), \quad (\text{A.13})$$

with the parameters  $M^{\text{at}}$  and the angles  $\theta_1^{\text{at}}, \theta_2^{\text{at}}$  and the bond-bond-13 term

$$U_{ijkl}^{\text{bb13}} = N^{\text{bb13}} (r_{ij} - r_1^{\text{bb13}}) (r_{kl} - r_3^{\text{bb13}}), \quad (\text{A.14})$$

with the parameters  $N^{\text{bb13}}$  and the distances  $r_1^{\text{bb13}}, r_3^{\text{bb13}}$

**Improper** The improper contribution can further decomposed in

$$U_{ijkl}^{\text{I}} = U_{ijkl}^{\text{i}} + U_{ijkl}^{\text{aa}}, \quad (\text{A.15})$$

with the improper term

$$U_{ijkl}^{\text{i}} = K^{\text{i}} \left( \frac{1}{3} (\chi_{ijkl} + \chi_{kjli} + \chi_{ljik}) - \chi_0 \right)^2 \quad (\text{A.16})$$

with the parameters  $K^i$  and the equilibrium angle  $\chi_0$ . The angle-angle term follows by

$$U_{ijkl}^{aa} = M_1^{aa} (\theta_{ijk} - \theta_1^{aa}) (\theta_{kjl} - \theta_3^{aa}) + \quad (\text{A.17})$$

$$M_2^{aa} (\theta_{ijk} - \theta_1^{aa}) (\theta_{ijl} - \theta_2^{aa}) + \quad (\text{A.18})$$

$$M_3^{aa} (\theta_{ijl} - \theta_2^{aa}) (\theta_{kjl} - \theta_3^{aa}) \quad (\text{A.19})$$

with the parameters  $M_1^{aa}, M_2^{aa}, M_3^{aa}$  and the angles  $\theta_1^{aa}, \theta_2^{aa}, \theta_3^{aa}$ .

## A.2 Two-stage polymerization<sup>1</sup>

**Benzene distribution** In order to be able to investigate the spatial distribution of the various constituents, a reasonable approach must be chosen. Especially molecules like (P-)MDI or the unsaturated polyester consist of numerous atoms, which can be distributed widely over the system. Reducing them to their center of mass would not result in a useful distribution. Instead, specific functional groups are chosen. For example, all molecules (except the coupling agent) contain benzene rings. In addition, they can be distinguished by their

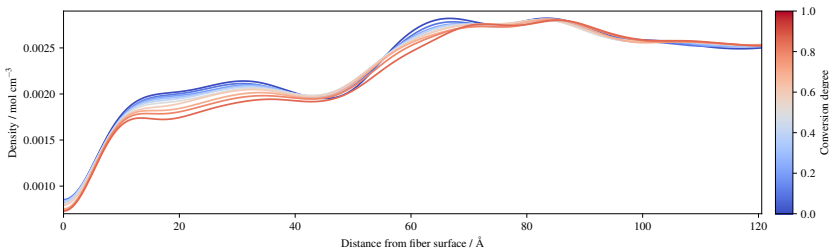


**Figure A.1:** Spatial distribution of the benzene of styrene during radical polymerization.

---

<sup>1</sup>The content of this section has been taken directly from Schöller et al. [2] with minor linguistic changes.

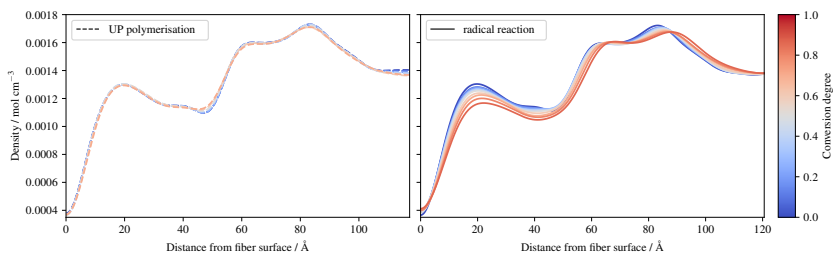


**Figure A.2:** Spatial distribution of benzene of (P)-MDI during polyurethane reaction (left) and radical polymerization (right) for different conversion degrees.

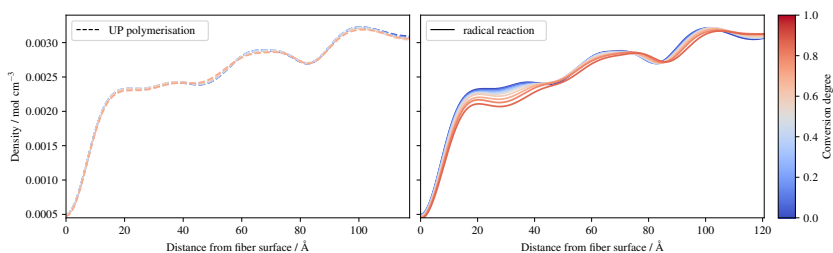


**Figure A.3:** Spatial distribution of benzene of the unsaturated polyester during polyurethane reaction (left) and radical polymerization (right) for different conversion degrees.

uniquely bonded atoms. This allows easy tracking of all benzene rings across the system and during polymerization reactions.

Figure A.1 shows the styrene benzene during radical polymerization. During the reaction, the small styrene molecules level out the initial uneven distribution due to diffusion. The benzene distribution of the larger molecules such as (P)-MDI and the unsaturated polyester is shown in Figure A.2 and Figure A.3, respectively. Despite the fact that they also exhibit some additional artificial charges during the polyurethane reaction, significant diffusion is not observed. In contrast, they show diffusion during the radical polymerization, as they smooth the initial uneven distribution.

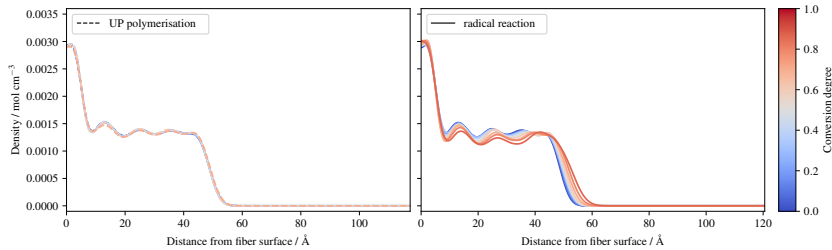


**Figure A.4:** Spatial distribution of silicon atoms of  $\gamma$ -MPS molecules during polyurethane reaction (left) and radical polymerization (right) for different conversion degrees.

**Silicon distribution of coupling agent** For the distribution of the coupling agent, hence  $\gamma$ -MPS, the silicon atom of the molecules is used to represent the position of the free hydrolyzed as well as the coupling agent pre-attached to the fiber surface. Figure A.4 shows this distribution during the polymerization reactions. As before, no significant diffusion can be observed during the polyurethane reaction. Nevertheless, the pre-attached layer with the very high peak at the fiber surface as well as the absence of  $\gamma$ -MPS in the pure resin layer can be observed. During the free radical polymerization, as with the other constituents, diffusion takes place, smoothing out the initial distribution.

### A.3 Phase-field modeling of crack propagation<sup>2</sup>

**Staggered iterations study** For a numerical investigation of the number of staggered iterations during a crack propagation simulation, the setup of an artificial sloped interface, cf. Section 6.4.2, is chosen. For this purpose, the number of iterations is depicted in Figure A.5. The cumulative iterations over

<sup>2</sup>The content of this section has been taken directly from Schöller et al. [1] with minor linguistic changes.

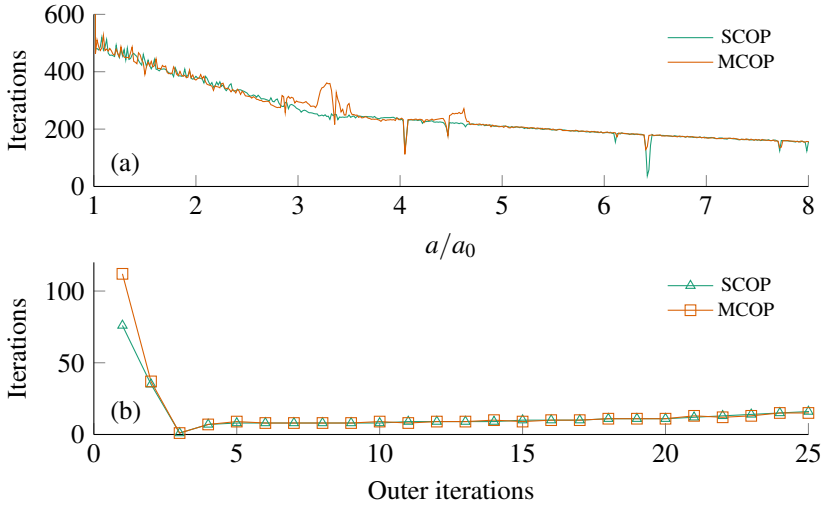


**Figure A.5:** Behavior of the staggered scheme for the artificial sloped interface: (a) Cumulative iterations during the crack growth for the SCOP and MCOP models. (b) Amount of inner iterations for an exemplary discrete crack propagation step.

the crack growth are shown in Figure A.5a. For this purpose, all inner staggered iterations are summed up until a discrete crack propagation occurs. Thereby, the SCOP and MCOP models show similar behavior. The number of iterations is approximately equal. Only near the solid interface the MCOP requires more iterations. This is most likely due to the implicit transition of the crack from one order parameter to the other. The overall trend towards fewer iterations, like the change in slope, is likely due to the way the stress boundary condition is imposed. In addition, Figure A.5b plots the number of staggered iterations against temporal iterations for a discrete crack propagation step. Also here, SCOP and MCOP show the similar behavior: After a discrete crack propagation, the first iterations consist of an increased number of staggered iterations, while subsequently, the iterations are lower, but increase slightly again to the next discrete crack propagation.

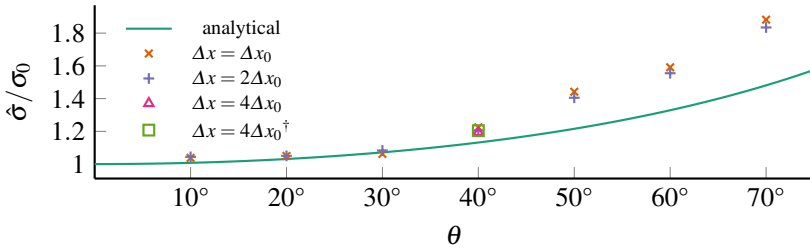


**Figure A.6:** Mesh convergence study of the SCOP model for the artificial sloped interface: The mesh sizes at the crack tip  $\Delta x$  are varied. In addition, the background was also refined and the adaptive mesh refinement parameters were chosen more cautiously ( $\dagger$ ).

**Mesh convergence study** For an investigation of mesh convergence for the artificial sloped interface example (cf. Section 6.4.2), the SCOP model and the infinitely hard upper region are chosen. As in this case the highest gradients occur in the solution fields and can therefore be assumed to be the most challenging problem to discretize. Figure A.6 shows the results of the SCOP model of Section 6.4.2. In addition, the mesh size  $\Delta x$  at the crack tip is varied, where  $\Delta x_0$  is the size in of the previous results. Furthermore, the underlying coarse mesh is significantly refined, and the adaptive mesh refinement parameters are changed to increase the area where  $\Delta x$  applies, denoted by  $\dagger$  in Figure A.6. Thereby, none of the results yields large variance, therefore the discretization chosen in this work can be assumed to be representative.

# Bibliography

- [1] L. Schöller, D. Schneider, C. Herrmann, A. Prahs, and B. Nestler, “Phase-field modeling of crack propagation in heterogeneous materials with multiple crack order parameters,” *Computer Methods in Applied Mechanics and Engineering*, vol. 395, p. 114965, 2022.
- [2] L. Schöller, B. Nestler, and C. Denniston, “Modeling of a two-stage polymerization considering glass fibre sizing using molecular dynamics,” *Nanoscale Advances*, vol. 5, pp. 106–118, 2023.
- [3] L. Schöller, D. Schneider, A. Prahs, and B. Nestler, “Phase-field modeling of crack propagation based on multi-crack orderparameters considering mechanical jump conditions,” *Proceedings in Applied Mathematics and Mechanics*, 2023.
- [4] A. Prahs, L. Schöller, F. K. Schwab, D. Schneider, T. Böhlke, and B. Nestler, “A multiphase-field approach to small strain crystal plasticity accounting for balance equations on singular surfaces,” *Computational Mechanics*, 2023.
- [5] T. Kannenberg, L. Schöller, A. Prahs, D. Schneider, and B. Nestler, “Investigation of microstructure evolution accounting for crystal plasticity in the multiphase-field method,” *Proceedings in Applied Mathematics andMechanics*, vol. 23, no. 3, p. e202300138, 2023.
- [6] A. B. Cherian, B. T. Abraham, and E. T. Thachil, “Modification of unsaturated polyester resin by polyurethane prepolymers,” *Journal of Applied Polymer Science*, vol. 100, no. 1, pp. 449–456, 2006.

- [7] T. Böhlke, F. Henning, A. Hrymak, L. Kärger, K. A. Weidenmann, and J. T. Wood, *Continuous-Discontinuous Fiber-Reinforced Polymers*. Carl Hanser Verlag GmbH & Co. KG, 2019.
- [8] J. Görthofer, N. Meyer, T. D. Pallicity, L. Schöttl, A. Trauth, M. Schemmann, M. Hohberg, P. Pinter, P. Elsner, F. Henning, A. Hrymak, T. Seelig, K. Weidenmann, L. Kärger, and T. Böhlke, “Motivating the development of a virtual process chain for sheet molding compound composites,” *Proceedings in Applied Mathematics and Mechanics*, vol. 19, no. 1, p. e201900124, 2019.
- [9] L. Schöttl, K. A. Weidenmann, Sabiston, K. Inal, and P. Elsner, “Fiber bundle tracking method to analyze sheet molding compound microstructure based on computed tomography images,” *NDT & E International*, vol. 117, p. 102370, 2021.
- [10] L. B. Freund, *Dynamic Fracture Mechanics*. Cambridge University Press, 1990.
- [11] B. Lawn, *Fracture of Brittle Solids*. Cambridge University Press, 1993.
- [12] H. Ming-Yuan and J. W. Hutchinson, “Crack deflection at an interface between dissimilar elastic materials,” *International Journal of Solids and Structures*, vol. 25, no. 9, pp. 1053–1067, 1989.
- [13] M. Amestoy and J. B. Leblond, “Crack paths in plane situations-II. Detailed form of the expansion of the stress intensity factors,” *International Journal of Solids and Structures*, vol. 29, no. 4, pp. 465–501, 1992.
- [14] G. I. Barenblatt, “The formation of equilibrium cracks during brittle fracture. General ideas and hypotheses. Axially-symmetric cracks,” *Journal of Applied Mathematics and Mechanics*, vol. 23, no. 3, pp. 622–636, 1959.

- 
- [15] D. S. Dugdale, “Yielding of steel sheets containing slits,” *Journal of the Mechanics and Physics of Solids*, vol. 8, no. 2, pp. 100–104, 1960.
- [16] M. Elices, G. V. Guinea, J. Gómez, and J. Planas, “The cohesive zone model: Advantages, limitations and challenges,” *Engineering Fracture Mechanics*, vol. 69, no. 2, pp. 137–163, 2001.
- [17] T. P. Fries and T. Belytschko, “The extended/generalized finite element method: An overview of the method and its applications,” *International Journal for Numerical Methods in Engineering*, vol. 84, no. 3, pp. 253–304, 2010.
- [18] A. Prahś and T. Böhlke, “On interface conditions on a material singular surface,” *Continuum Mechanics and Thermodynamics*, vol. 32, no. 5, pp. 1417–1434, 2020.
- [19] L.-Q. Chen, “Phase-Field Models for Microstructure Evolution,” *Annual Review of Materials Research*, vol. 32, no. 1, pp. 113–140, 2002.
- [20] N. Moelans, B. Blanpain, and P. Wollants, “An introduction to phase-field modeling of microstructure evolution,” *Calphad: Computer Coupling of Phase Diagrams and Thermochemistry*, vol. 32, no. 2, pp. 268–294, 2008.
- [21] B. Nestler and A. Choudhury, “Phase-field modeling of multi-component systems,” *Current Opinion in Solid State and Materials Science*, vol. 15, no. 3, pp. 93–105, 2011.
- [22] D. Schneider, O. Tschukin, A. Choudhury, M. Selzer, T. Böhlke, and B. Nestler, “Phase-field elasticity model based on mechanical jump conditions,” *Computational Mechanics*, vol. 55, no. 5, pp. 887–901, 2015.
- [23] C. Herrmann, E. Schoof, D. Schneider, F. Schwab, A. Reiter, M. Selzer, and B. Nestler, “Multiphase-field model of small strain elasto-plasticity

- according to the mechanical jump conditions,” *Computational Mechanics*, vol. 62, no. 6, pp. 1399–1412, 2018.
- [24] A. Karma, D. A. Kessler, and H. Levine, “Phase-field model of mode III dynamic fracture,” *Physical Review Letters*, vol. 87, no. 4, pp. 45 501–1–45 501–4, 2001.
- [25] R. Spatschek, M. Hartmann, E. Brener, H. Müller-Krumbhaar, and K. Kassner, “Phase field modeling of fast crack propagation,” *Physical Review Letters*, vol. 96, no. 1, p. 015502, 2006.
- [26] H. Henry and H. Levine, “Dynamic instabilities of fracture under biaxial strain using a phase field model,” *Physical Review Letters*, vol. 93, no. 10, p. 105504, 2004.
- [27] B. Bourdin, G. A. Francfort, and J. J. Marigo, “Numerical experiments in revisited brittle fracture,” *Journal of the Mechanics and Physics of Solids*, vol. 48, no. 4, pp. 797–826, 2000.
- [28] C. Kuhn and R. Müller, “A continuum phase field model for fracture,” *Engineering Fracture Mechanics*, vol. 77, no. 18, pp. 3625–3634, 2010, computational Mechanics in Fracture and Damage: A Special Issue in Honor of Prof. Gross.
- [29] C. Miehe, M. Hofacker, and F. Welschinger, “A phase field model for rate-independent crack propagation: Robust algorithmic implementation based on operator splits,” *Computer Methods in Applied Mechanics and Engineering*, vol. 199, no. 45–48, pp. 2765–2778, 2010.
- [30] A. A. Griffith, “VI. The phenomena of rupture and flow in solids,” *Philosophical Transactions of the Royal Society of London. Series A, Containing Papers of a Mathematical or Physical Character*, vol. 221, no. 582–593, pp. 163–198, 1921.

- [31] G. A. Francfort and J. J. Marigo, “Revisiting brittle fracture as an energy minimization problem,” *Journal of the Mechanics and Physics of Solids*, vol. 46, no. 8, pp. 1319–1342, 1998.
- [32] G. A. Francfort, B. Bourdin, and J. J. Marigo, “The variational approach to fracture,” *Journal of Elasticity*, vol. 91, no. 1-3, pp. 5–148, 2008.
- [33] C. Herrmann, D. Schneider, E. Schoof, F. Schwab, and B. Nestler, “Phase-field model for the simulation of brittle-anisotropic and ductile crack propagation in composite materials,” *Materials*, vol. 14, no. 17, 2021.
- [34] M. Ambati, T. Gerasimov, and L. De Lorenzis, “Phase-field modeling of ductile fracture,” *Computational Mechanics*, vol. 55, no. 5, pp. 1017–1040, 2015.
- [35] M. Ambati and L. De Lorenzis, “Phase-field modeling of brittle and ductile fracture in shells with isogeometric NURBS-based solid-shell elements,” *Computer Methods in Applied Mechanics and Engineering*, vol. 312, pp. 351–373, 2016.
- [36] C. Kuhn, T. Noll, and R. Müller, “On phase field modeling of ductile fracture,” *GAMM-Mitteilungen*, vol. 39, no. 1, pp. 35–54, 2016.
- [37] D. Schneider, M. Selzer, J. Bette, I. Rementeria, A. Vondrous, M. J. Hoffmann, and B. Nestler, “Phase-Field Modeling of Diffusion Coupled Crack Propagation Processes,” *Advanced Engineering Materials*, vol. 16, no. 2, pp. 142–146, 2014.
- [38] C. Miehe, L. M. Schänzel, and H. Ulmer, “Phase field modeling of fracture in multi-physics problems. Part I. Balance of crack surface and failure criteria for brittle crack propagation in thermo-elastic solids,” *Computer Methods in Applied Mechanics and Engineering*, vol. 294, pp. 449–485, 2015.

- [39] C. Miehe, M. Hofacker, L. M. Schänzel, and F. Aldakheel, “Phase field modeling of fracture in multi-physics problems. Part II. Coupled brittle-to-ductile failure criteria and crack propagation in thermo-elastic-plastic solids,” *Computer Methods in Applied Mechanics and Engineering*, vol. 294, pp. 486–522, 2015.
- [40] T. Wick, *Multiphysics Phase-Field Fracture: Modeling, Adaptive Discretizations, and Solvers*. De Gruyter, 2020.
- [41] B. Li, C. Peco, D. Millán, I. Arias, and M. Arroyo, “Phase-field modeling and simulation of fracture in brittle materials with strongly anisotropic surface energy,” *International Journal for Numerical Methods in Engineering*, vol. 102, no. 3-4, pp. 711–727, 2015.
- [42] T. T. Nguyen, J. Réthoré, J. Yvonnet, and M. C. Baietto, “Multi-phase-field modeling of anisotropic crack propagation for polycrystalline materials,” *Computational Mechanics*, vol. 60, no. 2, pp. 289–314, 2017.
- [43] C. Kuhn and R. Müller, “A discussion of fracture mechanisms in heterogeneous materials by means of configurational forces in a phase field fracture model,” *Computer Methods in Applied Mechanics and Engineering*, vol. 312, pp. 95–116, 2016.
- [44] M. Z. Hossain, C. J. Hsueh, B. Bourdin, and K. Bhattacharya, “Effective toughness of heterogeneous media,” *Journal of the Mechanics and Physics of Solids*, vol. 71, no. 1, pp. 15–32, 2014.
- [45] D. Schneider, E. Schoof, Y. Huang, M. Selzer, and B. Nestler, “Phase-field modeling of crack propagation in multiphase systems,” *Computer Methods in Applied Mechanics and Engineering*, vol. 312, pp. 186–195, 2016.
- [46] B. Nestler, H. Garcke, and B. Stinner, “Multicomponent alloy solidification: Phase-field modeling and simulations,” *Physical Review*

- E - Statistical, Nonlinear, and Soft Matter Physics*, vol. 71, no. 4, p. 041609, 2005.
- [47] N. Prajapati, C. Herrmann, M. Späth, D. Schneider, M. Selzer, and B. Nestler, “Brittle anisotropic fracture propagation in quartz sandstone: insights from phase-field simulations,” *Computational Geosciences*, vol. 24, no. 3, pp. 1361–1376, 2020.
- [48] M. Späth, C. Herrmann, N. Prajapati, D. Schneider, F. Schwab, M. Selzer, and B. Nestler, “Multiphase-field modelling of crack propagation in geological materials and porous media with Drucker-Prager plasticity,” *Computational Geosciences*, vol. 25, pp. 1–19, 2020.
- [49] A. C. Hansen-Dörr, R. de Borst, P. Hennig, and M. Kästner, “Phase-field modelling of interface failure in brittle materials,” *Computer Methods in Applied Mechanics and Engineering*, vol. 346, pp. 25–42, 2019.
- [50] A. C. Hansen-Dörr, F. Dammaß, R. de Borst, and M. Kästner, “Phase-field modeling of crack branching and deflection in heterogeneous media,” *Engineering Fracture Mechanics*, vol. 232, p. 107004, 2020.
- [51] T. T. Nguyen, J. Yvonnet, Q. Z. Zhu, M. Bornert, and C. Chateau, “A phase-field method for computational modeling of interfacial damage interacting with crack propagation in realistic microstructures obtained by microtomography,” *Computer Methods in Applied Mechanics and Engineering*, vol. 312, pp. 567–595, 2016.
- [52] M. Paggi and J. Reinoso, “Revisiting the problem of a crack impinging on an interface: A modeling framework for the interaction between the phase field approach for brittle fracture and the interface cohesive zone model,” *Computer Methods in Applied Mechanics and Engineering*, vol. 321, pp. 145–172, 2017.

- [53] R. Dimitri, P. Cornetti, V. Mantič, M. Trullo, and L. De Lorenzis, “Mode-I debonding of a double cantilever beam: A comparison between cohesive crack modeling and Finite Fracture Mechanics,” *International Journal of Solids and Structures*, vol. 124, pp. 57–72, 2017.
- [54] V. Carollo, T. Guillén-Hernández, J. Reinoso, and M. Paggi, “Recent advancements on the phase field approach to brittle fracture for heterogeneous materials and structures,” p. 8, 2018.
- [55] H. Henry, “Limitations of the modelling of crack propagating through heterogeneous material using a phase field approach,” *Theoretical and Applied Fracture Mechanics*, vol. 104, p. 102384, 2019.
- [56] A. Durga, P. Wollants, and N. Moelans, “Evaluation of interfacial excess contributions in different phase-field models for elastically inhomogeneous systems,” *Modelling and Simulation in Materials Science and Engineering*, vol. 21, no. 5, p. 55018, 2013.
- [57] J. Mosler, O. Shchyglo, and H. Montazer Hojjat, “A novel homogenization method for phase field approaches based on partial rank-one relaxation,” *Journal of the Mechanics and Physics of Solids*, vol. 68, no. 1, pp. 251–266, 2014.
- [58] K. Ammar, B. Appolaire, G. Cailletaud, and S. Forest, “Combining phase field approach and homogenization methods for modelling phase transformation in elastoplastic media,” *European Journal of Computational Mechanics*, vol. 18, no. 5-6, pp. 485–523, 2009.
- [59] B. Svendsen, P. Shanthraj, and D. Raabe, “Finite-deformation phase-field chemomechanics for multiphase, multicomponent solids,” *Journal of the Mechanics and Physics of Solids*, vol. 112, pp. 619–636, 2018.
- [60] D. Schneider, F. Schwab, E. Schoof, A. Reiter, C. Herrmann, M. Selzer, T. Böhlke, and B. Nestler, “On the stress calculation within phase-field

- approaches: a model for finite deformations,” *Computational Mechanics*, vol. 60, no. 2, pp. 203–217, 2017.
- [61] D. Schneider, E. Schoof, O. Tschukin, A. Reiter, C. Herrmann, F. Schwab, M. Selzer, and B. Nestler, “Small strain multiphase-field model accounting for configurational forces and mechanical jump conditions,” *Computational Mechanics*, vol. 61, no. 3, pp. 277–295, 2018.
- [62] J. Thomason, “Glass fibre sizing: A review,” *Composites Part A: Applied Science and Manufacturing*, vol. 127, p. 105619, 2019.
- [63] E. P. Plueddemann, “Adhesion Through Silane Coupling Agents,” *The Journal of Adhesion*, vol. 2, no. 3, pp. 184–201, 1970.
- [64] E. P. Plueddemann, “Silane coupling agents,” *Additives for plastics*, vol. 1, pp. 123–167, 1978.
- [65] J. A. Burgman, “The Manufacturing Technology of Continuous Glass Fibres, K. L. Lowenstein, Elsevier, Amsterdam, 1973. 280 pp.” *Journal of Polymer Science: Polymer Letters Edition*, vol. 12, no. 2, pp. 102–102, 1974.
- [66] J. L. Thomason, “The interface region in glass fibre-reinforced epoxy resin composites: 1. sample preparation, void content and interfacial strength,” *Composites*, vol. 26, no. 7, pp. 467–475, 1995.
- [67] J. L. Thomason, “The interface region in glass fibre-reinforced epoxy resin composites: 2. water absorption, voids and the interface,” *Composites*, vol. 26, no. 7, pp. 477–485, 1995.
- [68] J. L. Thomason, “The interface region in glass fibre-reinforced epoxy resin composites: 3. Characterization of fibre surface coatings and the interphase,” *Composites*, vol. 26, no. 7, pp. 487–498, 1995.
- [69] S. L. Gao and E. Mäder, “Characterisation of interphase nanoscale property variations in glass fibre reinforced polypropylene and epoxy

- resin composites,” *Composites - Part A: Applied Science and Manufacturing*, vol. 33, no. 4, pp. 559–576, 2002.
- [70] X. Liu, J. L. Thomason, and F. R. Jones, “XPS and AFM Study of Interaction of Organosilane and Sizing with E-Glass Fibre Surface,” *The Journal of Adhesion*, vol. 84, no. 4, pp. 322–338, 2008.
- [71] J. Karger-Kocsis, H. Mahmood, and A. Pegoretti, “Recent advances in fiber/matrix interphase engineering for polymer composites,” *Progress in Materials Science*, vol. 73, pp. 1–43, 2015.
- [72] T. Niuchi, J. Koyanagi, R. Inoue, and Y. Kogo, “Molecular dynamics study of the interfacial strength between carbon fiber and phenolic resin,” *Advanced Composite Materials*, vol. 26, no. 6, pp. 569–581, 2017.
- [73] L. ho Tam, A. Zhou, and C. Wu, “Nanomechanical behavior of carbon fiber/epoxy interface in hygrothermal conditioning: A molecular dynamics study,” *Materials Today Communications*, vol. 19, pp. 495–505, 2019.
- [74] S. Nouranian, C. Jang, T. E. Lacy, S. R. Gwaltney, H. Toghiani, and C. U. Pittman, “Molecular dynamics simulations of vinyl ester resin monomer interactions with a pristine vapor-grown carbon nanofiber and their implications for composite interphase formation,” *Carbon*, vol. 49, no. 10, pp. 3219–3232, 2011.
- [75] W. Jiao, C. Hou, X. Zhang, and W. Liu, “Molecular dynamics simulation of the influence of sizing agent on the interfacial properties of sized carbon fiber/vinyl ester resin composite modified by self-migration method,” *Composite Interfaces*, vol. 28, no. 5, pp. 445–459, 2021.
- [76] F. K. Schwab and C. Denniston, “Reaction and characterisation of a two-stage thermoset using molecular dynamics,” *Polymer Chemistry*, vol. 10, no. 32, pp. 4413–4427, 2019.

- 
- [77] S. Advani and E. Sozer, *Process Modeling in Composites Manufacturing, Second Edition*. Taylor & Francis, 2010.
- [78] L. Schöttl, “Development of methods for the characterization of damage in sheet molding compounds by using in-situ computed tomography,” Ph.D. dissertation, Karlsruher Institut für Technologie (KIT), 2021.
- [79] H. Altenbach, *Kontinuumsmechanik*. Springer Vieweg Berlin, Heidelberg, 2018.
- [80] A. Bertram and R. Glüge, *Solid Mechanics*. Springer Cham, 2015.
- [81] A. Bertram, *Elasticity and Plasticity of Large Deformations*. Springer Berlin, Heidelberg, 2011.
- [82] J. N. Reddy, *An Introduction to Continuum Mechanics*, 2nd ed. Cambridge University Press, 2013.
- [83] M. E. Gurtin, E. Fried, and L. Anand, *The Mechanics and Thermodynamics of Continua*. Cambridge University Press, 2010.
- [84] A. Prahś and T. Böhlke, “On invariance properties of an extended energy balance,” *Continuum Mechanics and Thermodynamics*, vol. 32, no. 3, pp. 843–859, 2020.
- [85] B. D. Coleman and W. Noll, “The thermodynamics of elastic materials with heat conduction and viscosity,” *Archive for Rational Mechanics and Analysis*, vol. 13, no. 1, pp. 167–178, 1963.
- [86] I. Steinbach, F. Pezzolla, B. Nestler, M. Seeßelberg, R. Prieler, G. Schmitz, and J. Rezende, “A phase field concept for multiphase systems,” *Physica D: Nonlinear Phenomena*, vol. 94, no. 3, pp. 135–147, 1996.
- [87] I. Steinbach and F. Pezzolla, “A generalized field method for multiphase transformations using interface fields,” *Physica D: Nonlinear Phenomena*, vol. 134, no. 4, pp. 385–393, 1999.

- [88] V. L. Ginzburg, “On the theory of superconductivity,” *Il Nuovo Cimento (1955-1965)*, vol. 2, no. 6, pp. 1234–1250, 1955.
- [89] J. W. Cahn and S. M. Allen, “A Microscopic Theory for Domain Wall Motion and Its Experimental Verification in Fe-Al Alloy Domain Growth Kinetics,” *Le Journal de Physique Colloques*, vol. 38, no. C7, pp. C7–51–C7–54, 1977.
- [90] A. C. Hansen-Dörr, J. Brummund, and M. Kästner, “Phase-field modeling of fracture in heterogeneous materials: jump conditions, convergence and crack propagation,” *Archive of Applied Mechanics*, vol. 91, no. 2, pp. 579–596, 2021.
- [91] D. Gross and T. Seelig, *Fracture Mechanics: With an Introduction to Micromechanics*, ser. Mechanical Engineering Series. Springer Berlin Heidelberg, 2011.
- [92] B. J. Alder and T. E. Wainwright, “Phase transition for a hard sphere system,” *The Journal of Chemical Physics*, vol. 27, no. 5, pp. 1208–1209, 1957.
- [93] B. J. Alder and T. E. Wainwright, “Studies in molecular dynamics. I. General method,” *The Journal of Chemical Physics*, vol. 31, no. 2, pp. 459–466, 1959.
- [94] F. H. Stillinger and A. Rahman, “Improved simulation of liquid water by molecular dynamics,” *The Journal of Chemical Physics*, vol. 60, no. 4, pp. 1528–1532, 1974.
- [95] W. F. van Gunsteren and H. J. C. Berendsen, “Computer Simulation of Molecular Dynamics: Methodology, Applications, and Perspectives in Chemistry,” *Angewandte Chemie International Edition in English*, vol. 29, no. 9, pp. 992–1023, 1990.
- [96] H. Goldstein, *Classical Mechanics*. Addison-Wesley, Reading, MA, 1980.

- [97] L. Verlet, "Computer "experiments" on classical fluids. I. Thermodynamical properties of Lennard-Jones molecules," *Physical Review*, vol. 159, no. 1, pp. 98–103, 1967.
- [98] W. C. Swope, H. C. Andersen, P. H. Berens, and K. R. Wilson, "A computer simulation method for the calculation of equilibrium constants for the formation of physical clusters of molecules: Application to small water clusters," *The Journal of Chemical Physics*, vol. 76, no. 1, pp. 637–649, 1982.
- [99] T. Schneider and E. Stoll, "Molecular-dynamics study of a three-dimensional one-component model for distortive phase transitions," *Physical Review B*, vol. 17, no. 3, pp. 1302–1322, 1978.
- [100] H. J. Berendsen, J. P. Postma, W. F. Van Gunsteren, A. Dinola, and J. R. Haak, "Molecular dynamics with coupling to an external bath," *The Journal of Chemical Physics*, vol. 81, no. 8, pp. 3684–3690, 1984.
- [101] H. Sun and D. Rigby, "Polysiloxanes: Ab initio force field and structural, conformational and thermophysical properties," *Spectrochimica Acta - Part A: Molecular and Biomolecular Spectroscopy*, vol. 53, no. 8, pp. 1301–1323, 1997.
- [102] H. Sun, "The COMPASS force field: Parameterization and validation for phosphazenes," *Computational and Theoretical Polymer Science*, vol. 8, no. 1-2, pp. 229–246, 1998.
- [103] H. Sun, "Compass: An ab initio force-field optimized for condensed-phase applications - Overview with details on alkane and benzene compounds," *Journal of Physical Chemistry B*, vol. 102, no. 38, pp. 7338–7364, 1998.
- [104] J. M. Barton, G. J. Buist, A. S. Deazle, I. Hamerton, B. J. Howlin, and J. R. Jones, "The application of molecular simulation to the rational design of new materials: 1. Structure and modelling studies of linear epoxy systems," *Polymer*, vol. 35, no. 20, pp. 4326–4333, 1994.

- [105] J. M. Barton, A. S. Deazle, I. Hamerton, B. J. Howlin, and J. R. Jones, “The application of molecular simulation to the rational design of new materials: 2. Prediction of the physico-mechanical properties of linear epoxy systems,” *Polymer*, vol. 38, no. 17, pp. 4305–4310, 1997.
- [106] C. Li, E. Coons, and A. Strachan, “Material property prediction of thermoset polymers by molecular dynamics simulations,” in *Acta Mechanica*, vol. 225, no. 4-5. Springer-Verlag Wien, 2014, pp. 1187–1196.
- [107] C. Li and A. Strachan, “Molecular dynamics predictions of thermal and mechanical properties of thermoset polymer EPON862/DETDA,” *Polymer*, vol. 52, no. 13, pp. 2920–2928, 2011.
- [108] L. Gao, Q. Zhang, H. Li, S. Yu, W. Zhong, G. Sui, and X. Yang, “Effect of epoxy monomer structure on the curing process and thermo-mechanical characteristics of tri-functional epoxy/amine systems: A methodology combining atomistic molecular simulation with experimental analyses,” *Polymer Chemistry*, vol. 8, no. 13, pp. 2016–2027, 2017.
- [109] N. Sharp, C. Li, A. Strachan, D. Adams, and R. B. Pipes, “Effects of water on epoxy cure kinetics and glass transition temperature utilizing molecular dynamics simulations,” *Journal of Polymer Science Part B: Polymer Physics*, vol. 55, no. 15, pp. 1150–1159, 2017.
- [110] A. C. Van Duin, S. Dasgupta, F. Lorant, and W. A. Goddard, “ReaxFF: A reactive force field for hydrocarbons,” *Journal of Physical Chemistry A*, vol. 105, no. 41, pp. 9396–9409, 2001.
- [111] K. D. Smith, S. I. Stoliarov, M. R. Nyden, and P. R. Westmoreland, “RMDff: A smoothly transitioning, forcefield-based representation of kinetics for reactive molecular dynamics simulations,” *Molecular Simulation*, vol. 33, no. 4-5, pp. 361–368, 2007.

- [112] M. T. Degiacomi, V. Erastova, and M. R. Wilson, “Easy creation of polymeric systems for molecular dynamics with Assemble!” *Computer Physics Communications*, vol. 202, pp. 304–309, 2016.
- [113] M. E. Fortunato and C. M. Colina, “pysimm: A python package for simulation of molecular systems,” *SoftwareX*, vol. 6, pp. 7–12, 2017.
- [114] V. Varshney, S. S. Patnaik, A. K. Roy, and B. L. Farmer, “A molecular dynamics study of epoxy-based networks: Cross-linking procedure and prediction of molecular and material properties,” *Macromolecules*, vol. 41, no. 18, pp. 6837–6842, 2008.
- [115] J. J. Schichtel and A. Chattopadhyay, “Modeling thermoset polymers using an improved molecular dynamics crosslinking methodology,” *Computational Materials Science*, vol. 174, p. 109469, 2020.
- [116] J. R. Gissinger, B. D. Jensen, and K. E. Wise, “Modeling chemical reactions in classical molecular dynamics simulations,” *Polymer*, vol. 128, pp. 211–217, 2017.
- [117] J. R. Gissinger, B. D. Jensen, and K. E. Wise, “Reacter: A heuristic method for reactive molecular dynamics,” *Macromolecules*, vol. 53, no. 22, pp. 9953–9961, 2020.
- [118] J. J. Karnes, T. H. Weisgraber, J. S. Oakdale, M. Mettry, M. Shusteff, and J. Biener, “On the Network Topology of Cross-Linked Acrylate Photopolymers: A Molecular Dynamics Case Study,” *Journal of Physical Chemistry B*, vol. 124, no. 41, pp. 9204–9215, 2020.
- [119] U. Schubert and T. Wieder, Eds., *Silicon Chemistry: From the Atom to Extended Systems*. Wiley-VCH Verlag GmbH & Co. KGaA, 2003.
- [120] F. T. Wallenberger and P. A. Bingham, *Fiberglass and glass technology: Energy-friendly compositions and applications*. Springer US, 2010.
- [121] M. E. Wieser, N. Holden, T. B. Coplen, J. K. Böhlke, M. Berglund, W. A. Brand, P. De Bièvre, M. Gröning, R. D. Loss, J. Meija, T. Hirata,

- T. Prohaska, R. Schoenberg, G. O'Connor, T. Walczyk, S. Yoneda, and X. K. Zhu, "Atomic weights of the elements 2011 (IUPAC technical report)," *Pure and Applied Chemistry*, vol. 85, no. 5, pp. 1047–1078, 2013.
- [122] R. Verleg and E. Hummer, "Unsaturated polyester urethane hybrid technology - fast track to advanced composites," 2006, pp. 1–16.
- [123] L. Peters, "Influence of Glass Fibre Sizing and Storage Conditions on Composite Properties," in *Solid Mechanics and its Applications*, vol. 245. Springer Verlag, 2018, pp. 19–31.
- [124] E. Mäder, E. Moos, and J. Karger-Kocsis, "Role of film formers in glass fibre reinforced polypropylene - new insights and relation to mechanical properties," *Composites Part A: Applied Science and Manufacturing*, vol. 32, no. 5, pp. 631–639, 2001.
- [125] S. Plimpton, "Fast Parallel Algorithms for Short-Range Molecular Dynamics," *Journal of Computational Physics*, vol. 117, pp. 1–19, 1995.
- [126] A. P. Thompson, H. M. Aktulga, R. Berger, D. S. Bolintineanu, W. M. Brown, P. S. Crozier, P. J. in 't Veld, A. Kohlmeyer, S. G. Moore, T. D. Nguyen, R. Shan, M. J. Stevens, J. Tranchida, C. Trott, and S. J. Plimpton, "LAMMPS - a flexible simulation tool for particle-based materials modeling at the atomic, meso, and continuum scales," *Comp. Phys. Comm.*, vol. 271, p. 108171, 2022.
- [127] L. Martínez, R. Andrade, E. G. Birgin, and J. M. Martínez, "PACKMOL: A package for building initial configurations for molecular dynamics simulations," *Journal of Computational Chemistry*, vol. 30, no. 13, pp. 2157–2164, 2009.
- [128] A. I. Jewett, D. Stelter, J. Lambert, S. M. Saladi, O. M. Roscioni, M. Ricci, L. Autin, M. Maritan, S. M. Bashusqeh, T. Keyes, R. T. Dame, J. E. Shea, G. J. Jensen, and D. S. Goodsell, "Moltemplate: A

- Tool for Coarse-Grained Modeling of Complex Biological Matter and Soft Condensed Matter Physics,” *Journal of Molecular Biology*, vol. 433, no. 11, p. 166841, 2021.
- [129] J. D. Miller and H. Ishida, “Quantitative monomolecular coverage of inorganic particulates by methacryl-functional silanes,” *Surface Science*, vol. 148, no. 2-3, pp. 601–622, 1984.
- [130] F. D. Blum, W. Meesiri, H. J. Kang, and J. E. Gambogi, “Hydrolysis, adsorption, and dynamics of silane coupling agents on silica surfaces,” *Journal of Adhesion Science and Technology*, vol. 5, no. 6, pp. 479–496, 1991.
- [131] Q. Liu, J. Ding, D. E. Chambers, S. Debnath, S. L. Wunder, and G. R. Baran, “Filler-coupling agent-matrix interactions in silica/polymethylmethacrylate composites,” *Journal of Biomedical Materials Research*, vol. 57, no. 3, pp. 384–393, 2001.
- [132] E. Mäder, H. J. Jacobasch, K. Grundke, and T. Gietzelt, “Influence of an optimized interphase on the properties of polypropylene/glass fibre composites,” *Composites Part A: Applied Science and Manufacturing*, vol. 27, no. 9 PART A, pp. 907–912, 1996.
- [133] M. Schneider, “The sequential addition and migration method to generate representative volume elements for the homogenization of short fiber reinforced plastics,” *Computational Mechanics*, vol. 59, no. 2, pp. 247–263, 2017.
- [134] M. Schneider, “An algorithm for generating microstructures of fiber-reinforced composites with long fibers,” *International Journal for Numerical Methods in Engineering*, vol. 123, no. 24, pp. 6197–6219, 2022.
- [135] P. A. Cundall and O. D. L. Strack, “A discrete numerical model for granular assemblies,” *Géotechnique*, vol. 29, no. 1, pp. 47–65, 1979.

- [136] J. Kafashan, J. Wicek, N. Abd Rahman, and J. Gan, “Two-dimensional particle shapes modelling for dem simulations in engineering: a review,” *Granular Matter*, vol. 21, no. 3, p. 80, 2019.
- [137] L. Pournin, M. Weber, M. Tsukahara, J.-A. Ferrez, M. Ramaioli, and T. M. Liebling, “Three-dimensional distinct element simulation of spherocylinder crystallization,” *Granular Matter*, vol. 7, no. 2, pp. 119–126, 2005.
- [138] F. K. Schwab, “Curing simulations of a fibre-reinforced thermoset on a micro- and nano-scale,” Ph.D. dissertation, Karlsruher Institut für Technologie (KIT), 2019.
- [139] A. Prahs, M. Reder, D. Schneider, and B. Nestler, “Thermomechanically coupled theory in the context of the multiphase-field method,” *International Journal of Mechanical Sciences*, vol. 257, p. 108484, 2023.
- [140] M. Kamal, S. Sourour, and M. Ryan, “Integrated thermorheological analysis of the cure of thermosets,” *SPE Tech. Pap.*, vol. 19, pp. 187–191, 1973.
- [141] M. R. Kamal and S. Sourour, “Kinetics and thermal characterization of thermoset cure,” *Polymer Engineering & Science*, vol. 13, no. 1, pp. 59–64, 1973.
- [142] A. Bernath, L. Kärger, and F. Henning, “Accurate cure modeling for isothermal processing of fast curing epoxy resins,” *Polymers*, vol. 8, no. 11, 2016.
- [143] A. T. DiBenedetto, “Prediction of the glass transition temperature of polymers: A model based on the principle of corresponding states,” *Journal of Polymer Science Part B: Polymer Physics*, vol. 25, no. 9, pp. 1949–1969, 1987.

- 
- [144] C. Kuhn, A. Schlüter, and R. Müller, “On degradation functions in phase field fracture models,” *Computational Materials Science*, vol. 108, pp. 374–384, 2015.
- [145] H. Amor, J. J. Marigo, and C. Maurini, “Regularized formulation of the variational brittle fracture with unilateral contact: Numerical experiments,” *Journal of the Mechanics and Physics of Solids*, vol. 57, no. 8, pp. 1209–1229, 2009.
- [146] C. Miehe, F. Welschinger, and M. Hofacker, “Thermodynamically consistent phase-field models of fracture: Variational principles and multi-field FE implementations,” *International Journal for Numerical Methods in Engineering*, vol. 83, no. 10, pp. 1273–1311, 2010.
- [147] M. Strobl and T. Seelig, “On constitutive assumptions in phase field approaches to brittle fracture,” in *Procedia Structural Integrity*, vol. 2. Elsevier B.V., 2016, pp. 3705–3712.
- [148] J. Storm, D. Supriatna, and M. Kaliske, “The concept of representative crack elements for phasefield fracture: Anisotropic elasticity and thermoelasticity,” *International Journal for Numerical Methods in Engineering*, vol. 121, no. 5, pp. 779–805, 2020.
- [149] M. Wheeler, T. Wick, and W. Wollner, “An augmented-lagrangian method for the phase-field approach for pressurized fractures,” *Computer Methods in Applied Mechanics and Engineering*, vol. 271, pp. 69–85, 2014.
- [150] T. Heister, M. F. Wheeler, and T. Wick, “A primal-dual active set method and predictor-corrector mesh adaptivity for computing fracture propagation using a phase-field approach,” *Computer Methods in Applied Mechanics and Engineering*, vol. 290, pp. 466–495, 2015.
- [151] K. Mang, T. Wick, and W. Wollner, “A phase-field model for fractures in nearly incompressible solids,” *Computational Mechanics*, vol. 65, no. 1, pp. 61–78, 2020.

- [152] J. Wambacq, J. Ulloa, G. Lombaert, and S. François, “Interior-point methods for the phase-field approach to brittle and ductile fracture,” *Computer Methods in Applied Mechanics and Engineering*, vol. 375, p. 113612, 2021.
- [153] I. Steinbach, “Phase-field models in materials science,” *Modelling and Simulation in Materials Science and Engineering*, vol. 17, no. 7, p. 31, 2009.
- [154] X. Li, J. Lowengrub, A. Rätz, and Voigt, “Solving pdes in complex geometries: a diffuse domain approach,” *Communications in Mathematical sciences*, vol. 7, no. 1, p. 81, 2009.
- [155] M. Plapp, “Phase-Field Models,” *CISM International Centre for Mechanical Sciences, Courses and Lectures*, vol. 538, pp. 129–175, 2012.
- [156] E. Tanné, T. Li, B. Bourdin, J. J. Marigo, and C. Maurini, “Crack nucleation in variational phase-field models of brittle fracture,” *Journal of the Mechanics and Physics of Solids*, vol. 110, pp. 80–99, 2018.
- [157] A. Kumar, B. Bourdin, G. A. Francfort, and O. Lopez-Pamies, “Revisiting nucleation in the phase-field approach to brittle fracture,” *Journal of the Mechanics and Physics of Solids*, vol. 142, p. 104027, 2020.
- [158] M. Klinsmann, D. Rosato, M. Kamlah, and R. M. McMeeking, “An assessment of the phase field formulation for crack growth,” *Computer Methods in Applied Mechanics and Engineering*, vol. 294, pp. 313–330, 2015.
- [159] K. H. Pham, K. Ravi-Chandar, and C. M. Landis, “Experimental validation of a phase-field model for fracture,” *International Journal of Fracture*, vol. 205, no. 1, pp. 83–101, 2017.

- 
- [160] X. Zhang, C. Vignes, S. W. Sloan, and D. Sheng, “Numerical evaluation of the phase-field model for brittle fracture with emphasis on the length scale,” *Computational Mechanics*, vol. 59, no. 5, pp. 737–752, 2017.
- [161] K. Pham and J.-J. Marigo, “Approche variationnelle de l’endommagement: II. Les modèles à gradient,” *Comptes Rendus Mécanique*, vol. 338, no. 4, pp. 199–206, 2010.
- [162] J.-Y. Wu and V. P. Nguyen, “A length scale insensitive phase-field damage model for brittle fracture,” *Journal of the Mechanics and Physics of Solids*, vol. 119, pp. 20–42, 2018.
- [163] D. Arndt, W. Bangerth, B. Blais, T. C. Clevenger, M. Fehling, A. V. Grayver, T. Heister, L. Heltai, M. Kronbichler, M. Maier, P. Munch, J. P. Pelteret, R. Rastak, I. Tomas, B. Turcksin, Z. Wang, and D. Wells, “The deal.II library, Version 9.2,” *Journal of Numerical Mathematics*, vol. 28, no. 3, pp. 131–146, 2020.
- [164] J. Hötzer, A. Reiter, H. Hierl, P. Steinmetz, M. Selzer, and B. Nestler, “The parallel multi-physics phase-field framework PACE3D,” *Journal of Computational Science*, vol. 26, pp. 1–12, 2018.
- [165] A. Trauth, “Characterisation and modelling of continuous-discontinuous sheet moulding compound composites for structural applications,” Karlsruhe, 2019.
- [166] J. Görthofer, N. Meyer, T. D. Pallicity, L. Schöttl, A. Trauth, M. Schemmann, M. Hohberg, P. Pinter, P. Elsner, F. Henning, A. Hrymak, T. Seelig, K. Weidenmann, L. Kärger, and T. Böhlke, “Virtual process chain of sheet molding compound: Development, validation and perspectives,” *Composites Part B: Engineering*, vol. 169, pp. 133–147, 2019.
- [167] A. Trauth, M. Bondy, K. A. Weidenmann, and W. Altenhof, “Mechanical properties and damage evolution of a structural sheet

- molding compound based on a novel two step curing resin system,” *Materials and Design*, vol. 143, pp. 224–237, 2018.
- [168] C. Miehe and A. Koch, “Computational micro-to-macro transitions of discretized microstructures undergoing small strains,” *Archive of Applied Mechanics*, vol. 72, no. 4-5, pp. 300–317, 2002.
- [169] R. Courant, K. Friedrichs, and H. Lewy, “Über die partiellen differenzgleichungen der mathematischen physik,” *Mathematische Annalen*, vol. 100, no. 1, pp. 32–74, 1928.
- [170] V. Thomée, “Stability theory for partial difference operators,” *SIAM Review*, vol. 11, no. 2, pp. 152–195, 1969.
- [171] M. Schober, “On the characterization and modeling of interfaces in fiber reinforced polymer structures,” Ph.D. dissertation, Karlsruhe Institut für Technologie (KIT), 2019.
- [172] S. Zhandarov and E. Mäder, “Characterization of fiber/matrix interface strength: applicability of different tests, approaches and parameters,” *Composites Science and Technology*, vol. 65, no. 1, pp. 149–160, 2005.
- [173] S. Yan, W. Verestek, H. Zeizinger, and S. Schmauder, “Characterization of Cure Behavior in Epoxy Using Molecular Dynamics Simulation Compared with Dielectric Analysis and DSC,” *Polymers*, vol. 13, no. 18, p. 3085, 2021.
- [174] E. Schoof, C. Herrmann, N. Streichhan, M. Selzer, D. Schneider, and B. Nestler, “On the multiphase-field modeling of martensitic phase transformation in dual-phase steel using J 2-viscoplasticity,” *Modelling and Simulation in Materials Science and Engineering*, vol. 27, no. 2, p. 025010, 2019.
- [175] M. Späth, J. L. Urai, and B. Nestler, “Incomplete crack sealing causes localization of fracturing in hydrothermal quartz veins,” *Geophysical Research Letters*, vol. 49, no. 15, p. e2022GL098643, 2022.

- [176] T. Kannenberg, L. Schöller, A. Prahs, D. Schneider, and B. Nestler, “Microstructure evolution accounting for crystal plasticity in the context of the multiphase-field method,” *Computational Mechanics*, 2023.



## List of the author's publications

- L. Schöller, D. Schneider, C. Herrmann, A. Prahs, and B. Nestler, "Phase-field modeling of crack propagation in heterogeneous materials with multiple crack order parameters," *Computer Methods in Applied Mechanics and Engineering*, vol. 395, p. 114965, 2022
- L. Schöller, B. Nestler, and C. Denniston, "Modeling of a two-stage polymerization considering glass fibre sizing using molecular dynamics," *Nanoscale Advances*, vol. 5, pp. 106–118, 2023
- L. Schöller, D. Schneider, A. Prahs, and B. Nestler, "Phase-field modeling of crack propagation based on multi-crack orderparameters considering mechanical jump conditions," *Proceedings in Applied Mathematics and Mechanics*, 2023
- A. Prahs, L. Schöller, F. K. Schwab, D. Schneider, T. Böhlke, and B. Nestler, "A multiphase-field approach to small strain crystal plasticity accounting for balance equations on singular surfaces," *Computational Mechanics*, 2023
- T. Kannenberg, L. Schöller, A. Prahs, D. Schneider, and B. Nestler, "Investigation of microstructure evolution accounting for crystal plasticity in the multiphase-field method," *Proceedings in Applied Mathematics and Mechanics*, vol. 23, no. 3, p. e202300138, 2023
- T. Kannenberg, L. Schöller, A. Prahs, D. Schneider, and B. Nestler, "Microstructure evolution accounting for crystal plasticity in the context of the multiphase-field method," *Computational Mechanics*, 2023



# List of Figures

Figure 1.1	The different length scales of fiber-reinforced thermosets . . . . .	2
Figure 2.1	Manufacturing process of semi-finished SMC . . . . .	12
Figure 2.2	The Compression molding process . . . . .	13
Figure 2.3	3D visualization of the tracked and clustered SMC fiber bundles . . . . .	14
Figure 2.4	Schematic representation of a diffuse interface when mechanical jump conditions are considered . . . . .	25
Figure 2.5	Different crack modes . . . . .	27
Figure 2.6	Different contributions to the intramolecular potential energy . . . . .	34
Figure 3.1	Schematic interface between glass fiber surface, fiber size and the resin . . . . .	36
Figure 3.2	Skeletal formula of the hydrolyzed $\gamma$ -MPS . . . . .	39
Figure 3.3	Hydrogen bonds of the coupling agent the glass fiber surface and with other coupling agent molecules . . . . .	41
Figure 3.4	The partition of the domain, the system after the polyurethane reaction and after the radical reaction . . . . .	46
Figure 3.5	Distribution of functional groups of the coupling agent after the condensation reaction and the temporal evolution . . . . .	50
Figure 3.6	Evolution of the number average molar mass and mass average molar mass for the two-stage polymerization . . . . .	53
Figure 3.7	Temporal evolution of the conversion degree of the two-stage polymerization over the simulations . . . . .	54

Figure 3.8	Spatial distribution of the crosslinking density and radical chains of the polyurethane reaction . . . . .	55
Figure 3.9	Spatial distribution of the radical chains length between PU crosslinks at different conversion degrees . . . . .	58
Figure 3.10	Spatial distribution of the benzene of styrene during radical polymerization . . . . .	60
Figure 4.1	Interaction of segments in a single curved fiber . . . . .	64
Figure 4.2	Connection and orientation vectors, in a fiber and between segments of different fibers . . . . .	65
Figure 4.3	Implemented force due to overlapping fiber segments . . . . .	67
Figure 4.4	Evolution of the energies during the generation procedure and generated 2D microstructure with unidirectional fibers . . . . .	68
Figure 4.5	Evolution of the different energies and the fiber volume fraction during the iterations of the generation procedure . . . . .	70
Figure 4.6	Generated quadratic 2D microstructures with curved fiber . . . . .	71
Figure 4.7	Generated 3D microstructures with curved fiber . . . . .	72
Figure 5.1	Temporal evolution of curing degree and temperature during the cure process for pure resin . . . . .	81
Figure 5.2	Evolution of curing degree, temperature and principal stress for unidirectional fiber-reinforced domains . . . . .	82
Figure 5.3	Maximum principal stress for a unidirectional and a two-dimensional curved fiber-reinforced system . . . . .	83
Figure 5.4	Evolution of curing degree, temperature and principal stress for two-dimensional curved fiber-reinforced domains . . . . .	84
Figure 5.5	Evolution of curing degree, temperature and principal stress for three-dimensional fiber-reinforced domains . . . . .	85

---

Figure 5.6	Distribution of maximum principal stress of a three-dimensional curved fiber-reinforced system . . . . .	86
Figure 5.7	Maximum principal stress over the fiber volume fraction for the different fiber setups . . . . .	87
Figure 6.1	Schematic homogeneous domain with a sharp crack interface and a diffuse crack interface . . . . .	90
Figure 6.2	Analytical order parameter profile for crack and solid . . . . .	93
Figure 6.3	Schematic heterogeneous domain for the SCOP and MCOP models . . . . .	95
Figure 6.4	Steady state profiles for a diffuse crack interface . . . . .	110
Figure 6.5	Error of the total crack energies and local error of the crack energy density . . . . .	110
Figure 6.6	Exemplary structure of an inclined interface and a initial crack . . . . .	113
Figure 6.7	Simulation domain with an initial crack and a marked and enlarged artificial interface region . . . . .	114
Figure 6.8	Normalized temporal evolution of the crack length, and the stress at the boundary, for the SCOP and MCOP model . . . . .	115
Figure 6.9	Crack propagation along the sloped interface, for sharp and diffuse interfaces . . . . .	116
Figure 6.10	Cross-section with the underlying solid interface, along the binary interface of the SCOP and MCOP model . . . . .	117
Figure 6.11	Exemplary visualization of the evaluation of the crack and comparison with an analytical solution . . . . .	119
Figure 6.12	Schematic of a single inclusion problem . . . . .	121
Figure 6.13	The strain energy densities of a single inclusion problem with displacement boundary conditions . . . . .	122
Figure 6.14	The strain energy densities of a single inclusion problem with eigenstrains in the matrix . . . . .	123
Figure 6.15	Effective maximum principal stress versus the curing shrinkage of the thermoset . . . . .	125
Figure 6.16	Effective crack path for using different schemes at different time steps . . . . .	126

Figure 6.17	Final crack paths for both potentials, and different homogenization schemes . . . . .	127
Figure 6.18	Different realizations of generated 2D volume elements with unidirectional fibers for varying fiber volume fractions . . . . .	130
Figure 6.19	A generated periodic 3D volume element with isotropic fiber distribution and the fractured volume element . . . . .	131
Figure 6.20	Crack path of 2D unidirectional fiber-reinforced volume elements for jump conditions and a Voigt-Taylor scheme . . . . .	132
Figure 6.21	Detail of the crack path for the effective crack order parameter . . . . .	133
Figure 6.22	Macroscopic stress-strain curves of 2D unidirectional fiber-reinforced volume elements . . . . .	135
Figure 7.1	Crack paths after curing for different fiber volume fractions and ensembles for the unidirectional FRTS . . .	141
Figure 7.2	Maximum principal stress for a fiber volume fraction of 50 % after curing simulation and with a crack . . . . .	143
Figure 7.3	Crack paths after curing for different fiber volume fractions and ensembles for the curved FRTS in 2D . . .	144
Figure 7.4	Volume element with 10 % fiber volume content and the final crack in color . . . . .	145
Figure 7.5	The crack length factor against the fiber volume fraction, for different level of abstraction of the microstructure . . . . .	146
Figure 7.6	Cross-sectional SEM image capturing the fracture within unidirectional glass fiber-reinforced thermoplastic . . . . .	147
Figure A.1	Spatial distribution of the benzene of styrene during radical polymerization . . . . .	158
Figure A.2	Spatial distribution of benzene during the polymerization for different conversion degrees . . . . .	159

---

Figure A.3	Spatial distribution of benzene during the polymerization for different conversion degrees . . . . .	159
Figure A.4	Spatial distribution of silicon atoms of $\gamma$ -MPS molecules for different conversion degrees . . . . .	160
Figure A.5	Behavior of the staggered scheme for the artificial sloped interface . . . . .	161
Figure A.6	Mesh convergence study of the SCOP model for the artificial sloped interface . . . . .	162



# List of Tables

Table 3.1	Components of the glass fiber surface . . . . .	37
Table 3.2	Composition of the different layer of the domain . . . . .	43
Table 3.3	Number of steps and time steps for each simulation step and the different systems . . . . .	47
Table 4.1	Parameters for the generation fiber structures . . . . .	68
Table 4.2	Additional parameters for the generation of curved fiber structures . . . . .	70
Table 5.1	Material parameters for the glass fiber . . . . .	78
Table 5.2	References for the material parameters for the UPPH resin	79
Table 6.1	Comparison of the terms in the balance of linear momentum and the evolution equation of the SCOP and MCOP model . . . . .	102
Table 6.2	Material properties and interface width parameters for simulating the fracture of FRP volume elements . . . . .	128



## Schriftenreihe des Instituts für Angewandte Materialien

---

ISSN 2192-9963

---

Eine vollständige Übersicht der Bände finden Sie im Verlagsshop

- Band 50 Michael Selzer  
**Mechanische und Strömungsmechanische Topologie-  
optimierung mit der Phasenfeldmethode.**  
ISBN 978-3-7315-0431-3
- Band 51 Michael Mahler  
**Entwicklung einer Auswertemethode für  
bruchmechanische Versuche an kleinen Proben  
auf der Basis eines Kohäsivzonenmodells.**  
ISBN 978-3-7315-0441-2
- Band 52 Christoph Bohnert  
**Numerische Untersuchung des Verformungs- und  
Bruchverhaltens von einkristallinem Wolfram auf  
mikroskopischer Ebene.**  
ISBN 978-3-7315-0444-3
- Band 53 Stefan Guth  
**Schädigung und Lebensdauer von Nickelbasislegierungen  
unter thermisch-mechanischer Ermüdungsbeanspruchung  
bei verschiedenen Phasenlagen.**  
ISBN 978-3-7315-0445-0
- Band 54 Markus Klinsmann  
**The Effects of Internal Stress and Lithium Transport on  
Fracture in Storage Materials in Lithium-Ion Batteries.**  
ISBN 978-3-7315-0455-9
- Band 55 Thomas Straub  
**Experimental Investigation of Crack Initiation in  
Face-Centered Cubic Materials in the High and  
Very High Cycle Fatigue Regime.**  
ISBN 978-3-7315-0471-9

- Band 56 Maren Lepple  
**Kupfer- und Eisenoxide als Konversions-Elektrodenmaterialien für Lithium-Ionen-Batterien: Thermodynamische und Elektrochemische Untersuchungen.**  
ISBN 978-3-7315-0482-5
- Band 57 Stefan Andreas Slaby  
**Charakterisierung und Bewertung der Zug- und Ermüdungseigenschaften von Mikrobauteilen aus 17-4PH Edelstahl. Ein Vergleich von mikropulverspritzgegossenem und konventionell hergestelltem Material.**  
ISBN 978-3-7315-0484-9
- Band 58 Kumar Ankit  
**Phase-field modeling of microstructural pattern formation in alloys and geological veins.**  
ISBN 978-3-7315-0491-7
- Band 59 Kuo Zhang  
**Characterization and Modeling of the Ratcheting Behavior of the Ferritic-Martensitic Steel P91.**  
ISBN 978-3-7315-0503-7
- Band 60 Nicht erschienen
- Band 61 Fabian Lemke  
**Untersuchung des Sinterverhaltens von SrTiO<sub>3</sub> unter Berücksichtigung der Defektchemie.**  
ISBN 978-3-7315-0510-5
- Band 62 Johannes Kümmel  
**Detaillierte Analyse der Aufbauschneidenbildung bei der Trockenerspannung von Stahl C45E mit Berücksichtigung des Werkzeugverschleißes.**  
ISBN 978-3-7315-0518-1
- Band 63 László Hagymási  
**Modellierung der Stoffübertragung beim Niederdruckcarbonitrieren mit Ammoniak und Acetylen.**  
ISBN 978-3-7315-0568-6
- Band 64 Reza Eslami  
**A novel micro-mechanical model for prediction of multiaxial high cycle fatigue at small scales.**  
ISBN 978-3-7315-0583-9

- Band 65 Sebastian Schulz  
**Phase-field simulations of multi-component solidification and coarsening based on thermodynamic datasets.**  
ISBN 978-3-7315-0618-8
- Band 66 Markus Stricker  
**Die Übertragung von mikrostrukturellen Eigenschaften aus der diskreten Versetzungsdynamik in Kontinuumsbeschreibungen.**  
ISBN 978-3-7315-0658-4
- Band 67 Luis Straßberger  
**Untersuchung und Modellierung des viskoplastischen Verformungsverhaltens oxidpartikelverstärkter Stähle.**  
ISBN 978-3-7315-0674-4
- Band 68 Mark Wobrock  
**Microplasticity of idealized single crystalline Ag cantilevers characterized with methods of high resolution.**  
ISBN 978-3-7315-0682-9
- Band 69 Amritesh Kumar  
**Micromechanical study on the deformation behaviour of directionally solidified NiAl-Cr eutectic composites.**  
ISBN 978-3-7315-0694-2
- Band 70 Johannes Hötzer  
**Massiv-parallele und großskalige Phasenfeldsimulationen zur Untersuchung der Mikrostrukturentwicklung.**  
ISBN 978-3-7315-0693-5
- Band 71 Thomas Hupfer  
**Herstellung von LATP für den Einsatz als Festkörperelektrolyt und dessen Eigenschaften.**  
ISBN 978-3-7315-0702-4
- Band 72 Florentin Pottmeyer  
**Schädigungsverhalten von in CFK-Laminaten eingebetteten Inserts unter bauteilnahen Beanspruchungen.**  
ISBN 978-3-7315-0719-2
- Band 73 Andres Höweling  
**Untersuchung der Hochvoltstabilität und Tiefentladung von dotierten  $\text{LiNi}_{0,5}\text{Mn}_{1,5}\text{O}_4$ -Hochvoltspinellen.**  
ISBN 978-3-7315-0728-4

- Band 74     Tabea Gisela Schwark  
**Deformation and Fracture Properties of the Soft Magnetic Composite Somaloy 700 3P on Different Length Scales.**  
ISBN 978-3-7315-0759-8
- Band 75     Klaudia Lichtenberg  
**Metallmatrixverbunde mit Verstärkungselementen aus metallischem Glas  $\text{Ni}_{60}\text{Nb}_{20}\text{Ta}_{20}$  – Herstellung und Charakterisierung.**  
ISBN 978-3-7315-0782-6
- Band 76     Claudio Findeisen  
**Charakterisierung und Modellierung von instabilen Metamaterialien.**  
ISBN 978-3-7315-0869-4
- Band 77     Nilesha Mishra  
**Influence of strain on the functionality of ink-jet printed thin films and devices on flexible substrates.**  
ISBN 978-3-7315-0853-3
- Band 78     Simon Werner Bonk  
**Plastische Verformungsmechanismen in hochgradig kaltgewalzten, ultrafeinkörnigen Wolframblechen.**  
ISBN 978-3-7315-0878-6
- Band 79     Tim Gräning  
**Herstellung, Charakterisierung und Optimierung von austenitischen ODS Stählen.**  
ISBN 978-3-7315-0732-1
- Band 80     Peter Rupp  
**Herstellung, Prüfung und Modellierung neuartiger hybrider Aluminiumschaum-CFK-Sandwichverbunde.**  
ISBN 978-3-7315-0880-9
- Band 81     Benjamin Sebastian Ehreiser  
**Einfluss mechanischer Lasten auf die Herstellung von Stahl-Glaskeramik-Verbunden.**  
ISBN 978-3-7315-0954-7
- Band 82     Hans Giel  
**Weiterentwicklung experimenteller Methoden zur Ermittlung thermodynamischer Werkstoffdaten von Lithium-Ionen-Batterien.**  
ISBN 978-3-7315-0981-3

- Band 83 Anna Trauth  
**Characterisation and Modelling of Continuous-Discontinuous Sheet Moulding Compound Composites for Structural Applications.**  
ISBN 978-3-7315-0950-9
- Band 84 Jonas Johannes Hüther  
**The Impact of Recycling on the Fibre and the Composite Properties of Carbon Fibre Reinforced Plastics.**  
ISBN 978-3-7315-0983-7
- Band 85 Nicolas A. Mayer  
**Thermodynamik von Kobaltoxid Anodenmaterialien für Lithium-Ionen-Batterien und ihr elektrochemisches Verhalten.**  
ISBN 978-3-7315-0996-7
- Band 86 Ulrich Führer  
**Untersuchung und Modellierung des Haltezeiteinflusses auf die zyklische Entfestigung ferritisch-martensitischer Stähle.**  
ISBN 978-3-7315-0837-3
- Band 87 Ebru Cihan  
**Structure evolution in tribological interfaces studied by multilayer model alloys.**  
ISBN 978-3-7315-0999-8
- Band 88 Markus Sudmanns  
**Entwicklung einer Kontinuumsbeschreibung für die Versetzungsmobilität in Versetzungsnetzwerken.**  
ISBN 978-3-7315-1001-7
- Band 89 Tao Zhang  
**Phase-field Modeling of Phase Changes and Mechanical Stresses in Electrode Particles of Secondary Batteries.**  
ISBN 978-3-7315-1002-4
- Band 90 Markus Ganser  
**On the Electro-Chemo-Mechanical Coupling in Solid State Batteries and its Impact on Morphological Interface Stability.**  
ISBN 978-3-7315-1047-5

- Band 91 Michael Kellner  
**Modellierung mehrkomponentiger Materialsysteme für die Phasenfeldmethode und Analyse der simulierten Mikrostrukturen.**  
ISBN 978-3-7315-1044-4
- Band 92 Felix Schröckert  
**Herstellung dünner Folien aus Lithium-Lanthan-Titanat zur Anwendung als Festkörperelektrolyt.**  
ISBN 978-3-7315-1008-6
- Band 93 Ephraim Schoof  
**Chemomechanische Modellierung der Wärmebehandlung von Stählen mit der Phasenfeldmethode.**  
ISBN 978-3-7315-1050-5
- Band 94 Alexander Valentin Brabänder  
**Registrierende Härtemessung an neutronenbestrahlten Materialien bei hohen Temperaturen.**  
ISBN 978-3-7315-1097-0
- Band 95 Denny Schmidt  
**Einfluss der Kompaktierung auf die Elektrodenmikrostruktur und elektrochemische Performance bei Lithium-Ionen-Zellen.**  
ISBN 978-3-7315-1098-7
- Band 96 Svenja Dittrich  
**Entwicklung von Siebdruckpasten zur Herstellung von Glaslotfugungen für die Festoxidbrennstoffzelle.**  
ISBN 978-3-7315-1085-7
- Band 97 Michael Dippon  
**Bestimmung der Betriebsgrenzen für das Schnellladen von Lithium-Ionen Batterien.**  
ISBN 978-3-7315-1123-6
- Band 98 Patricia Haremski  
**Diffusionseigenschaften von Nickel in einer Festoxid-Brennstoffzelle.**  
ISBN 978-3-7315-1124-3
- Band 99 Florian Wankmüller  
**Mehrskalige Charakterisierung der Hochtemperatur-Brennstoffzelle (SOFC).**  
ISBN 978-3-7315-1142-7

- Band 100 Niklas Russner  
**Modellgestützte Analyse des Stackbetriebs von Festoxidzellen.**  
ISBN 978-3-7315-1144-1
- Band 101 Theo Fett, Karl G. Schell, Ethel C. Bucharsky, Gabriele Rizzi, Pascal Hettich, Susanne Wagner, Michael J. Hoffmann  
**Consequences of hydroxyl generation by the silica/water reaction – Part I: Diffusion and Swelling.**  
ISBN 978-3-7315-1148-9
- Band 102 Theo Fett, Karl G. Schell, Ethel C. Bucharsky, Gabriele Rizzi, Susanne Wagner, Michael J. Hoffmann  
**Consequences of hydroxyl generation by the silica/water reaction – Part II: Global and local Swelling  
Part III: Damage and Young's Modulus.**  
ISBN 978-3-7315-1159-5
- Band 103 Johannes Dornheim  
**Modellfreies Lernen optimaler zeitdiskreter Regelungsstrategien für Fertigungsprozesse mit endlichem Zeithorizont.**  
ISBN 978-3-7315-1158-8
- Band 104 Markus Muth  
**Grundlagenuntersuchungen an intrinsisch gefertigten lasttragenden FVK/Metall-Hybridträgern.**  
ISBN 978-3-7315-1161-8
- Band 105 Oleg Birkholz  
**Modeling transport properties and electrochemical performance of hierarchically structured lithium-ion battery cathodes using resistor networks and mathematical half-cell models.**  
ISBN 978-3-7315-1172-4
- Band 106 Verena Irene Becker  
**Modellierung der Mechanik und der effektiven Transporteigenschaften von partikulären Kathoden sowie deren Einfluss auf die elektrochemische Performance von Lithium-Ionen-Batterien.**  
ISBN 978-3-7315-1174-8
- Band 107 Nikolai Zimmer  
**Nanoskalige Analytik der Mikrostruktur von hochdosig bestrahltem Beryllium.**  
ISBN 978-3-7315-1178-6

- Band 108 Francesco Mazzocchi  
**Development of NbN based Kinetic Inductance Detectors on sapphire and diamond substrates for fusion plasma polarimetric diagnostics.**  
ISBN 978-3-7315-1181-6
- Band 109 Adrian Schmidt  
**Multiskalige Modellierung von Lithium-Ionen-Batterien.**  
ISBN 978-3-7315-1227-1
- Band 110 Maximilian Röhe  
**Dynamic Model-based Analysis of Oxygen Reduction Reaction in Gas Diffusion Electrodes.**  
ISBN 978-3-7315-1234-9
- Band 111 Michael Späth  
**Phasenfeldmodellierung von Bruchbildungs-, Kristallisations- und Auflösungsvorgängen in hydrothermalen Umgebungen.**  
ISBN 978-3-7315-1242-4
- Band 112 Friedemann Streich  
**Numerische Modellierung und Simulation von bleifreien Relaxor-Ferroelektrikum-Kompositen.**  
ISBN 978-3-7315-1259-2
- Band 113 Paul S. Zielonka  
**Entwicklung und Charakterisierung von Siliziumnitrid-/Siliziumkarbidkompositen für den Einsatz in tribologisch hochbeanspruchten Gleitsystemen.**  
ISBN 978-3-7315-1269-1
- Band 114 Carsten Bonnekoh  
**Der Spröd-duktil-Übergang in ultrafeinkörnigem Wolfram.**  
ISBN 978-3-7315-1264-6
- Band 115 Marcel Heinzmann  
**Analyse und Modellbildung von PEM-Brennstoffzellen mittels elektrochemischer Impedanzspektroskopie.**  
ISBN 978-3-7315-1319-3
- Band 116 Felix Sutter  
**Materiell nichtlineare Kontinuumsmodellierung ferroelektrischer Funktionskeramiken mit piezoelektrischen und flexoelektrischen Eigenschaften.**  
ISBN 978-3-7315-1337-7

Band 117    Lukas Schöller  
**Multiscale Modeling of Curing and Crack Propagation  
in Fiber-Reinforced Thermosets.**  
ISBN 978-3-7315-1340-7

KARLSRUHER INSTITUT FÜR TECHNOLOGIE (KIT)  
SCHRIFTENREIHE DES INSTITUTS FÜR ANGEWANDTE MATERIALIEN

Glass-fiber reinforced polymers are becoming increasingly important in industrial applications because of their lightweight potential at relatively low cost. During processing of fiber-reinforced thermosets, the resin material undergoes a chemical reaction that results in chemical shrinkage. Combined with thermal expansion, the microstructure can be damaged during this manufacturing process. A two-step polymerization reaction is modeled using a molecular dynamics approach. Evaluations of the resin system are performed in terms of averaged quantities as well as quantities along the normal direction of the fiber surface, resulting in spatially varying properties along the fiber-resin interface. In addition, a novel phase-field model for crack propagation in heterogeneous systems is derived. The new multi-crack order parameter model is able to quantitatively predict crack growth where established models fail. Finally, the crack propagation model is combined with a curing model to predict micro-crack formation during the curing process of glass fiber reinforced UPPH resin.

ISSN 2192-9963  
ISBN 978-3-7315-1340-7

